Politecnico di Milano

SCHOOL OF INDUSTRIAL AND INFORMATION ENGINEERING

Master of Science – Electrical Engineering

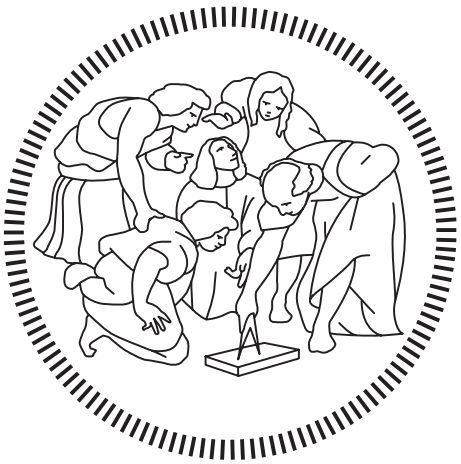

EV Fast Charging with Embedded Battery Energy System in Weak Grid Conditions

Supervisor

Prof. Francesco CASTELLI DEZZA

Co-Supervisor

Title Name SURNAME

Candidate

Marco SAIA

Student Number:

10522725

Academic Year 2020 – 2021

SOMMARIO

L'integrazione dei veicoli elettrici (EV) nella rete elettrica è un argomento caldo nella comunità ingegneristica. La ricarica veloce (Fast Charging) sarà introdotta come una soluzione per avvicinare le funzionalità degli EV ai veicoli ICE (Internal Combustion Engine), e i suoi lati negativi saranno considerati e ovviati attraverso l'uso di un sistema integrato di energia a batteria (BES). La batteria integrata proverrà da batterie dismesse di veicoli elettrici, nelle cosiddette applicazioni "Second-Life". Verranno anche introdotti gli effetti dell'integrazione del BES nella rete.

Sarà proposta una possibile topologia di un caricatore veloce EV con sistema di batterie integrato, per osservare come risolve i problemi sopra menzionati. Un prototipo è in costruzione con la collaborazione di ENGIE EPS, un'azienda italiana leader nel settore della mobilità elettrica. Saranno mostrati i risultati preliminari di questo prototipo.

Una panoramica generale del sistema, completa di modello di simulazione, sarà analizzata per comprendere meglio l'impostazione in cui la ricarica veloce deve essere integrata e riconoscere le aree in cui la topologia fornisce vantaggi e svantaggi rispetto all'integrazione nella rete, la ricarica EV e i costi. In seguito, l'attenzione si sposterà sulla progettazione del filtro per un convertitore AC/DC a bassa potenza che deve mantenere determinati standard. Questo lavoro propone la progettazione del filtro come punto di partenza, attraverso un algoritmo generale che è valido per le impostazioni di bassa potenza, permettendo un'attenta considerazione degli effetti del filtro sulle prestazioni del convertitore, che è spesso trascurato.

Dopo aver introdotto accuratamente un modello matematico per i convertitori commutati PWM, la strategia di base di controllo *dq* sarà impiegata per la progettazione di un controllore lineare stabile, le cui prestazioni saranno valutate contro lo smorzamento delle armoniche e la rigidità della rete. Verranno introdotti alcuni parametri per valutare l'invariabilità delle prestazioni. Saranno poi descritte la strategia di smorzamento attivo ACC (Active Capacitor Current), con particolare attenzione agli effetti che i sistemi digitali hanno sul feedback di stato. Verrà proposto un nuovo algoritmo per garantire in fase di progettazione la completa compatibilità con la velocità del controllore rispetto alla frequenza di switching del convertitore, visualizzando gli effetti discreti nel familiare dominio di Laplace.

Infine, verrà introdotto un controllore adattivo STR (Self Tuning Regulator) come possibile alternativa allo smorzamento attivo e le prestazioni saranno di nuovo valutate rispetto alla induttanza di rete nel punto di connessione. Un confronto finale sarà tracciato per confrontare il classico regolatore di smorzamento attivo PI e quello STR appena trovato.

Parole chiave: Ricarica veloce; Controllo digitale; Batteria Litio; Controllore STR; Rigidità di rete.

ABSTRACT

Grid EV integration has been a discussed topic for several years in the engineering community. Fast charging will be introduced as a solution to the even the playing field with respect to ICE (Internal Combustion Engine) vehicles, and its downsides will be considered and solved via the used of an integrated Battery Energy System (BES). The battery will likely come from decommissioned Electric Vehicle (EV) batteries, in the so called “Second-Life” applications. The effects of BES integration in the network will also be introduced.

A possible topology of an EV Fast Charger with Integrated Battery System will be given, to observe how it solves the aforementioned problems. A prototype is being built with the collaboration of ENGIE EPS, an Italian leading company in the sector of electric Mobility. Preliminary results of this prototype will be shown, however full control on the variables will not be shown due to trade secrets.

A general overview of the system, complete of simulation model, will be analyzed to better understand the setting in which fast charging needs to be integrated and recognize the areas in which the topology provides advantages and disadvantages for grid integration, EV charging and costs. After that, the focus will be shifted on the design of the filter for a low power AC/DC converter which needs to maintain certain standards. This work proposes filter design as the starting point, via a general algorithm that is valid for low power settings, allowing for careful consideration of the filter effects on the performance of the converter, which is oftentimes overlooked.

After thoroughly introducing a mathematical model for PWM switched converters the basic *dq-control* strategy will be employed for the design of a stable linear controller, its performance will be waged against harmonic damping and grid stiffness. Some parameters will be introduced to evaluate performance invariability. Active damping strategies will be then described, with particular focus on the effects that digital systems have on state feedback. A novel algorithm will be proposed to ensure in the design phase complete compatibility with the speed of the controller by viewing discrete effects in the familiar Laplace domain.

Finally and adaptive STR (Self Tuning Regulator) controller will be introduced as a possible solution to active damping and the performances will again be wage again grid stiffness. A final comparison will be drawn to compare the classical PI Active damping controller and the newly found STR one.

Keywords: Fast Charging; Digital Control; Li-ion Battery; STR Controller; Grid Stiffness

Paper Type: Design / Research

ACKNOWLEDGEMENTS

This thesis represents the completion of a double degree program with Xi'an Jiaotong University, which has been the most challenging experience of my life. I could not have completed this path without the assistance of many people which have supported, directed and taught me in the last 3 years.

First, I would like to thank the exchange program staff and Professors Pignari and Grassi at Politecnico di Milano for allowing me to join the program. Then I would like to thank my supervisor Professor Castelli Dezza for giving me to opportunity to spend my internship, which was integral to the completion of the program, in a great company.

I would like to extend my gratitude to all the colleagues at EPS, both in Storage and e-Mobility, that from the start showed nothing but support and patience and were always there to teach me. In particular I would like to thank my e-Mobility and work partner Arcangelo, from which I learnt a great deal both in the technical and in the human ways. I would also like to thank Roberto and later Martino for being responsible and caring for me inside the company.

Furthermore I wish to mention all the friends that I have made in these long years of university and even before! I have met a lot of special people starting from my academic colleagues both in the Bachelor's and Master's which have eased the hardships and highlighted the successes of studying at Polimi, my roommates Marco and Francesco without whom I would not have survived in a distant foreign country, my Chinese friends and Yao in particular also without whom we would have all starved when first landed in China.

To my longtime hometown friends that supported me when times were though, made me feel like I always had a place to come back to and that spent with me many sad and happy nights with me, thank you, there is nobody else like you.

Finally, to all my family whose unyielding help allowed me in every way possible: financially, emotionally and physically.

To my mom Mariella, my dad Claudio and my brother Fabio even though we had to face many problems your thinking about my best interest has never waned and I will be forever grateful.

Last but not least, to my grandma Amneris. You were the best and I so wish you could see me now.

LIST OF CONTENTS

LIST OF FIGURES

LIST OF TABLES

LIST OF REFERENCES

Object	**Reference**
Electric Vehicle	EV
Internal Combustion Engine	ICE
Fuel Cell	FC
Hybrid Electric Vehicle	HEV
Plug-in Hybrid Electric Vehicle	PHEV
Plug-in Electric Vehicle	PEV
Vehicle to Grid	V2G
Total Harmonic Distortion	THD
Human Machine Interface	HMI
State of Charge	SOC
State of Health	SOH
Silicon Carbide	SiC
First Life	FL
Second Life	SL
Battery Energy Storage	BES
Original Equipment Manufacturer	OEM
Dual Active Bridge	DAB
Active Capacitor Current	ACC
Beginning of Life	BOL
End of Life	EOL
Self-Tuning Regulator	STR

1 INTRODUCTION

In recent years, the fact that evolution based on carbon fossil fuel on earth is unsustainable has been well documented. A social spotlight has been directed to the issue by green politic groups and this has raised awareness to the public and world leaders, however the scientific community has been presenting studies for 15-years already that examine the feasibility of reducing human reliance on finite resources such as fossil fuels. There are two main reasons as for why growth using fossil fuels as power source is not feasible:

- Environmental Concerns

  Pollution rise is associated with temperature rise all around the globe. In fact, studies have correlated average particulate to average temperature rise quantitatively, defining benchmarks that should be satisfied were humanity to keep the global climate from changing. To keep average global temperature, increase below 2°C (as has been agreed in the UN Paris Agreement [1]), the cumulative amount of carbon dioxide that can be emitted while maintaining a certain probability of remaining below this target temperature is what is defined as a 'carbon budget'. In the latest Intergovernmental Panel on Climate Change (IPCC) report, the budget was estimated to be approximately 275 billion tons of carbon for a 50% chance. The crucial factor is that if the world expended all its currently known reserves (without the use of carbon capture and storage technology) a total of nearly 750 billion tons of carbon would be emitted. This means that around two-thirds of known reserves will need to be untouched if the WHO global climate targets are to be met.

  Pollution is toxic for all wildlife and human life; the latter are especially affected because pollution concentrations are higher around cities. The World Health Organization (WHO) provided Figure 1 to explain the data to the public [2].

Figure 1 Health risk associated with pollution [56]

- Availability Concerns

The world reservoirs of fossil fuels are not infinite: to give a static indicative estimate of how long human society could feasibly consume fossil fuels, the Reserves-to-Production (R/P) ratio for coal, oil and gas based on 2015 figures are plotted in Figure 2 based on BP's Statistical

Review of World Energy 2016, about 115 years of coal production, and roughly 50 years of both oil and natural gas are left for the world to consume [3].

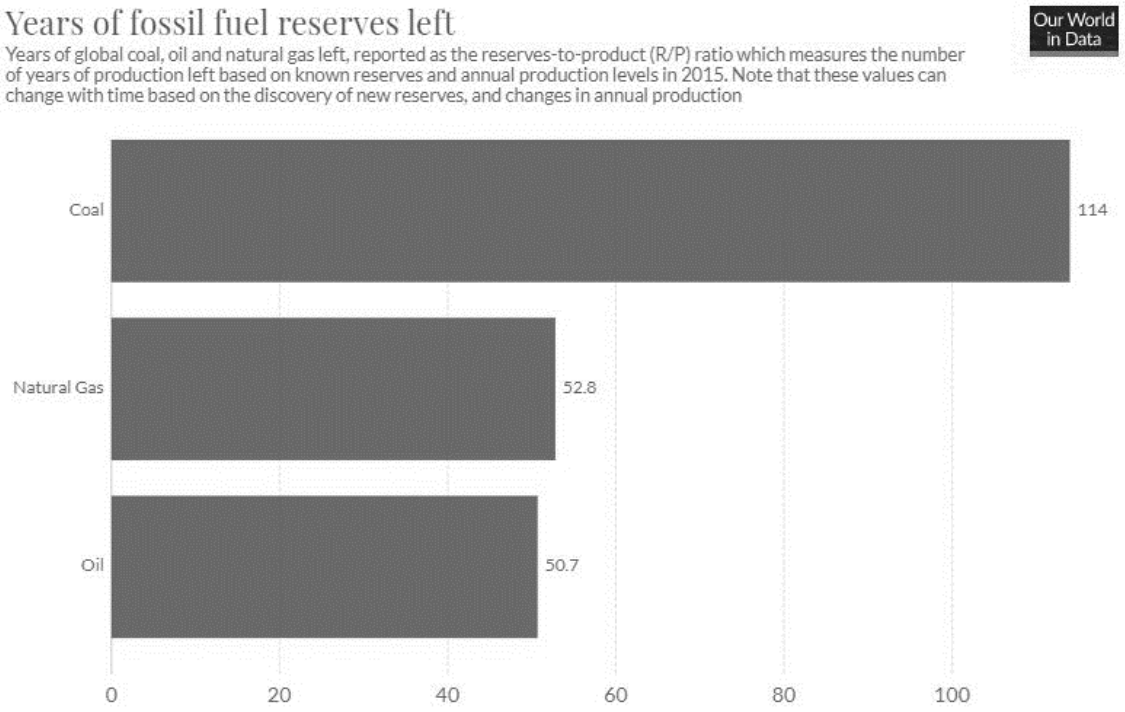

Figure 2 Fossil Fuel Reserves

1.1 ELECTRIC VEHICLES AND THE FIGHT ON POLLUTION

Reports indicate that up to 30% of total human sourced pollution stems from road transportation [4], indicating a very concise step to reduce carbon emissions: the extensive penetration of EVs in the transportation system, which obviously does not only include the private sector but public and private altogether. In study [5] Chinese researches analyze the Beijing situation, taking into consideration three different growth scenarios for research breakthrough and infrastructures funding in China (which is also one of the leading countries in terms of pollution), and conclude, via a statistical model, that up to 600 tons of CO2 can be saved in every year after 2050, achieving a reduction of around 40% in the urban area. Great strides have been made to improve the EVs features, so the comparison with the ICE vehicle would tip in favor of the former, this fueled resources to the research of better performing electrical energy storage (i.e. Batteries) to mount on board of the EV. The industry has come to the point where ranges (especially in premium products) can easily stand up to the carbon fossil-based alternative, reportedly some EVs can have ranges of around 400 km and 200 km when de-rated, for example by the use of air conditioning or the GPS system. Since the efficiency of the EV's powertrain has not improved by much (just a few percentages) lately, the main innovation is coming in terms of how much energy can be stored in the energy accumulation system, which in most cases consists of a battery, but other solutions (such as FCs and supercapacitors) have been explored with less success.

1.2 NECESSITY FOR FAST CHARGING

As of 2020 on-board battery systems in EVs need to have an energy capacity in the tens of kWh, meaning that in private households the time it takes to recharge the battery, with a standard electric supply of a few kW at grid voltage (400 V), spans from 5 to 10 hours, which would be a huge limitation in the readiness of the vehicle; especially when comparing it to the time it takes to re-fuel an ICE (under a minute in a gas station). Recharge modalities are classified by type, power voltage and current in Table 1. While it is true that for everyday use, given the schedule of the individual, it is easy to circumvent this issue, the problem is relevant when more leisurely activities or long trips are considered. All in all, it is a concern that could prevent some potential customers from buying an EV, for issues unrelated to the EV itself, therefore reducing the depth of penetration in the market. This scenario is to avoid since it could reduce the amount of funding in the sector, further setting back the advancements in the field. Higher power dense supply becomes almost inevitable, but this also poses issues, this time in the management of the power grid, which would be magnified anyway by the popular diffusion of electrical energy-based vehicles. The idea is commonly referenced as Fast Charging, meaning having the possibility to charge the EV in matter of around an hour, with higher power, typically upwards of 20 kW which would be challenging to draw from the grid. Some solution involving private usage of the three-phase network or converting in DC have been employed, and successfully resolved the issue of charging time but ultimately the energy still needs to be drawn in bulk from the mains.

Table 1 European EV charging

Charge Time [h]	Power Supply	Power [kW]	Voltage [V]	Current [A]
6-10	Single Phase	3	230	15
3-6	Single Phase	10	230	30
2-3	Three Phase	10	400	15
1-2	Three Phase	20	400	60
≃0.5	Direct Current	50	>500 DC	100

1.3 GRID IMPACT OF BATTERY CHARGING

Many studies have been published on the matter of mass battery integration into the power grid, which poses both challenges and potential benefits. The number of Electric Vehicles of any sort (HEV, PHEV, PEV) sold has increased starting from the early 2010s [6], and is projected to grow at least as much in the next decade. This means the number of vehicles that will require charging could be as many as 4 million in the U.S. alone , in addition some countries like China and Japan are working to integrate EVs in the public transport system, aggravating the demand on the mains. Not all EVs can be connected through the gird, but as technology improves that will be less reasons to choose a hybrid over a fully electric car, so that the share of fully electric vehicles will increase from the current 25% [7]. Considering half of the 4 million projection in

2026 to be Plug-ready, considering half cycle charges per day, the possible increase in daily demand would be around 50 GWh daily from the private sector alone. The 50 GWh increase in generation capacity might not seem relevant compared the current capacity of the U.S. of over a 1000 GW, but if reasonably short time of charge are considered power peaks might become high and erratic. The problems this causes are already consolidated:

1. Grid Infrastructure Overload

   The high current needed to rapidly charge a battery, through and AC/DC converter will most likely result in peaks of current (in the order of tens of amperes for each appliance) which will surely surpass the thermal ratings of MV/LV transformers in residential areas, where a brute upgrade will be needed in terms of size even in best case scenario. Study [8] analyzes two areas; one urban and one industrial, considering different charging strategies and types of cycles (spanning from 0.2 C to 2 C) to determine the needed upgrades and costs, and estimates the infrastructures will need to be improved by around 20%. An interesting feature that is considered in this study is V2G integration, which supposes the bi-directionality of the charger to transfer energy from the "resting" vehicles to an area in demand, however the transformer rating must be observed carefully because moving energy between areas has twice the impact on currents rather than importing it from outside, as shown by study [9]. Furthermore, single phase chargers will need to be avoided in order to ease the tasks of the local distributor of balancing the phases.

2. Area Voltage Control

   While MV analysis focuses on the power flow and energy efficiency regarding the integration of PEVs, the problem of voltage sagging due to erratic vehicle recharge deals with the intrinsic radial nature of the LV system and the integration of distributed renewable energy sources. Both studies [10] [11] analyze the voltage profile in the ever so popular IEEE 34 radial feeder in the unregulated environment and conclude that regulation of some sort will be necessary. Study [11] focuses on heavy-duty vehicles, that introduce a unique set of problem due to the high power necessary: each charging station may require up to 1 MW of power. The grid is studied using a Voltage Level Sensitivity Matrix (VLSM), in conjunction with a Montecarlo Simulation to decide the charge cycle based on location, and highlights that more charging station are detrimental to the stability of voltage, because high energy spikes can be drawn simultaneously and are always available, while less charging stations introduce traffic and waiting time for the heavy duty vehicles. Neither solution is desirable and the authors hint that distributed energy sources might alleviate this condition. Article [10] considers the more traditional problem of light vehicles charging, and via a statistical analysis formulates a minimization problem on power losses constraining the vehicles to full charges. The problem is formulated in Eq1.1 as:

$$\min\left(\sum_{t=1}^{tmax}\sum_{l=1}^{lines} R_l * I_{l,t}^2\right)$$
$$s.t.\begin{cases} \forall t, \forall node : 0 \le P_{n,t} \le P_{max} \\ \forall node : \sum_{t=1}^{t_{max}} P_{n,t}\Delta t * x_n = C_{max} \\ x_n \in \{0;1\} \end{cases} \quad (1.1)$$

Where R_l is the resistance of line l; $I_{l,t}^2$ is the squared current at each time t, under the constraint of max power at each node n, considering full charge C_{max} for a distribution of PHEV x_n and here-in lies the problem: the distribution x_n is hard to know a priori outside of statistical analysis. The QP min problem[1], however, yields good results in this study and could be applied if predictable distribution were to be introduced.

3. Power Quality

   Typically, PEVs chargers draw grid voltage AC power and rectify it to DC and then process the rectified signal using a DC/DC converter. These processes produce harmonic distortion in the distribution system. The nonlinear elements such as inverters and switching cells, lead to a significant increase in voltage distortion and current harmonics on power distribution networks. These harmonics cause problems on the power system, and excessive neutral current and transformer hot spots. Grid regulation usually limit the level of THD up to some order of harmonics to a percentage (e.g. the EN 50160 $THD_{n<40} < 8\%$). The main solutions to this issue are EMI filtering and active filtering, study [12] proposes active filtering based on the current modulation of a PV panel connected to 5 EV chargers and the main inverter and successfully compliant with the normative, exhibiting less than 5% total distortion.

1.4 BATTERY ENERGY SYSTEM (BES) INTEGRATION

As seen in the previous chapter, the main problems from the point of view of grid integration arise from two distinctive features of the PEVs: the high power requirements drawn from the mains and the unpredictability of distribution of vehicles in the charging stations x_n. One solution is to insert an electric "inertia" attached to the charger, to stabilize the intake of energy from the grid, allowing the usage of algorithms of planned charging (e.g. the one presented in [10]) to be more easily implemented. While adding an off-board battery might seem redundant due to losses in the transfer, the advantages are largely surpassed given the very high efficiency of static power converters ($\eta > 97\%$), and considering that the battery could slowly siphon energy from the mains allows for the operation point to be at the very maximum efficiency. Aside from a Li-ion battery, other means of storage are available, but since the charger must be

[1] A quadratic programming (QP) problem has a quadratic cost function and linear constraints. Generally nonlinear programming algorithms require solution of a quadratic programming subproblem at each iteration.

designed to be widespread even in private households, other methods like FCs, supercapacitors and rotating inertias require greater expertise in use and maintenance.

A battery integrated with the EV charger solves the problem of high power requirements for the benefit of both final user and grid operator: the power of the battery can be designed to meet the requirement of fast charging without overloading the MV/LV transformer even when multiple PEVs are connected. The battery is discharged rapidly when the vehicle needs to be operative and slowly gets recharged on planned operations, even allowing for V2G capability that could serve to sustain the network both in voltage (locally), and frequency (globally)[2], if current capacity of the transformer is not met.

Even if every battery charger is not equipped with a battery the uncertainty of distribution x_n would be reduced for every BES integrated charger present, meaning said solutions could be accounted for singularly. The rate of charge and discharge (C-rate)[3] of the battery needs to be determined by human input (reflecting the needs of final user) through an interface (HMI) and network requirement, using locally implemented algorithms. Optimal discharge of the off-board battery may be achieved by a combination of grid and said battery to the EV battery.

Main modes of operation possible are listed in Table 2:

Charging EV from the mains: The EV is plugged in and little charge is present inside the battery, the vehicle recharges at contractual power from the 400 V grid. Notice the battery is not disengaged because it must always have battery to provide the DC-link voltage to ease the control effort, providing a fixed and know voltage on the DC-link.

Charging EV from battery: The battery is fully charged, and high-power transmission is possible from the off-board battery to the EV.

Joint Charge: Both the mains and the off-board battery are utilized to recharge the EV. This mode of operation is characterized by a longer recharge time where grid and off-board battery supply balance to achieve higher efficiency discharge (depending on the C-rate).

V2G: The EV's battery supplies the mains with demanded power, this mode happens only if the off-board battery is low on charge, else it will take precedence.

Off-board battery to Mains: The off-board battery discharges onto the main grid whenever the vehicle is done charging, or the selling operation is convenient. The EV may be plugged or unplugged, the EV's battery is disengaged.

1.5 PROPOSED TOPOLOGY

The technical specifics taken into consideration in this instance are reported in Table 3, Table 4, and Table 5. Most EV chargers consist of a front-end AC/DC converter with a DC/DC converter in the EV Battery side, which also provides the opportunity to connect the BES in

[2] Energy can be transferred into the same radial feeder where voltage sagging is occurring due to current imported from the MV grid (e.g. on the far end of a small sized line), while it can also be transferred upstream into the MV grid to aid total generating effort.

[3] C-rate is a term used to indicate the rate of discharge of a battery in terms of total capacity, for example a C-rate of 1 implies a current that would discharge the battery in one hour.

between converters effectively forming a DC-link. AC-link chargers have been studied [13] but the high number of components and the absence of a common DC part prevent the usage of this solution.

Table 2 Modes of Operations

Mode of Operation	**Grid Status**	**Off-board Battery**	**EV Battery**
Charging EV from mains	Engaged (Supply)	Engaged (Voltage Stabilization)	Engaged (Receiver)
Charging EV from battery	Disengaged	Engaged (Supply)	Engaged (Receiver)
Joint Charge	Engaged (Supply)	Engaged (Supply)	Engaged (Receiver)
V2G	Engaged (Receiver)	Engaged (Voltage Stabilization)	Engaged (Supply)
Off-board battery to Mains	Engaged (Receiver)	Engaged (Supply)	Disengaged

In general, less Power Electronics Components are present in a design the better reliability it will possess, on this note it might be useful to observe that a dedicated DC/DC converter for the Integrated BES is not strictly necessary because the setpoints of the AC/DC can be adjusted to the slowly varying battery voltage (the maximum charging power is 11 kW). The battery must never be discharged fully to provide voltage uncoupling between the converters, and in accordance with Table 2Table 2, the usage of a dedicated DC/DC converter for the off-board battery, might reduce reliability (given the always engaged nature of the BES).

As shown by Table 4 and Table 5 the allowed voltage of the BES is always higher than the EV's battery, meaning a "buck-like" DC/DC converter will suffice for the BES-EV connection.

The proposed architecture is shown Figure 3 where in addition to the power components, the main control and interface elements are highlighted. The control elements all converge to the controller that takes into consideration the inputs, decides the protocols to be used and controls the physical dynamics of the power transfer.

In the upcoming chapters of this work the different elements represented in Figure 3 will be analyzed. A general overview complete of simulation will be given, to better understand the setting in which fast charging needs to be integrated and recognize the areas in which the topology provides advantages for the integration and where there are problems instead. After that, the focus will be shifted on the design of the filter for a low power AC/DC converter which needs to maintain certain standards. This work proposes filter design as the starting point, via a general algorithm that is valid for low power settings, this allows for careful consideration of the filter effects on the performance of the converter, which is oftentimes overlooked.

Table 3 AC Side Specs

AC Side	
Max Power [kW]	11
Voltage [V]	400
Frequency [Hz]	50

Table 4 EV Specs

EV Side	
Max EV Charging Power [kW]	50
Voltage range [V]	< 500
Max current [A]	125

Table 5 BES Specs

Battery System	
Rated Capacity [kWh]	42
Voltage range [V]	590 – 810
Max current [A]	125
Max C-rate	1.2

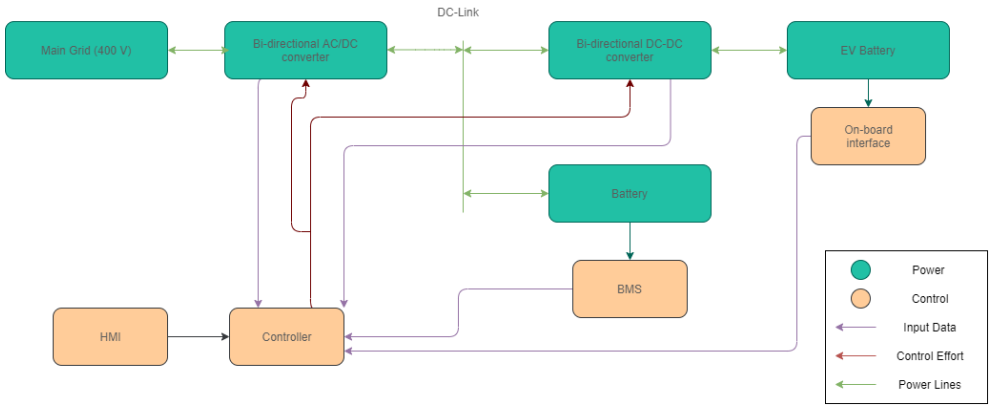

Figure 3 Main Architecture

After thoroughly introducing a mathematical model for PWM switched converters the basic *dq-control* strategy will be employed for the design of a stable linear controller, its performance will be waged against harmonic damping and grid stiffness. Some parameters will be introduced to evaluate performance invariability. Active damping strategies will be then described, with particular focus on the effects that digital systems have on state feedback. A novel algorithm will be proposed to ensure in the design phase complete compatibility with the speed of the controller by viewing discrete effects in the familiar Laplace domain.

Finally, a non-linear state feedback discrete control will be proposed to tackle the same problems that active damping previously solved and performances will be compared via simulation.

Chapter 2: Every component (see Figure 4) will be implemented in simulation software to provide a general overview of the principles on which the system will be operating. Used control strategies and will be validated and tested on a prototype, which fits the industrial state of the art. Emphasis will be given on power flux and the role of the battery in the stabilization of the system all well as the problems that it poses. The battery and battery management system will be reviewed. Some of the more common battery chemistries will be described and employed for simulation.

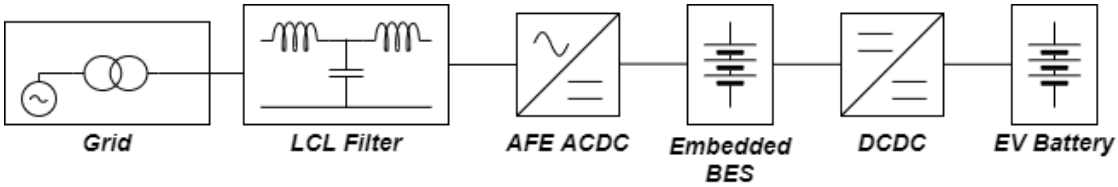

Figure 4 Main components introduced in Chapter 2.

Chapter 3: Various topologies of the AC/DC converter will be presented. An emphasis will be placed on the modality in which new technologies ease the task of the designer, and the design of the LCL filter.

Chapter 4: The linear inner control strategy of the AC/DC converter will be explained and discussed and, once it has been established, the problem of grid compatibility and digital active damping will be analyzed. A novel determination algorithm will be proposed for the choice of the active damping feedback gain.

Chapter 5: A nonlinear state feedback discrete control strategy will be introduced along with the mathematical instruments for its use. The choice is based on the inherent similarity with the active damping strategy previously described and so the aptitude of both strategies to be compared. This control strategy will be based on an adaptive state estimation algorithm to patch the open problems form other chapters.

Chapter 6: A summary of the whole work will be provided, along with final considerations and next steps. A conclusive comparison on control schemes will be drawn that highlight pros and cons of each one.

2 SYSTEM OVERVIEW

The importance of having an overview of the whole system when designing a component is well established in the engineering world, so a description of each component in the fast-charging environment for EVs is detailed in this section. The previous chapter nominated these such parts, but it was limited in the sense that it did not provide any space where to draw the final choices; a deeper understating upon these options pinpoints the direction in which the industry is moving, what problems have already been solved and which yet remain.

From service provider standpoint two configuration are common: either the AC conversion is centralized via a bigger power converter or distributed where the AC conversion is left to a stand-alone lesser capable converter in terms of power transfer. The main characteristics of the converter as well as a rudimental description is given in Chapter 2.1, however the more technical details are left for Chapter 3 and 4.

2.1 ACDC POWER FLOW CONTROL

The most important characteristic of an ACDC converter for EV charging is to be able to handle power transfers in both directions, devices possessing this characteristic are called AFEs (Active Front End). The need for this has already been established, however the modality of achieving such feat is still left to the designer. When vehicle charging is interested a more stable approach is needed to ensure flexibility of connection to the DC bus of the converter, so regulating the output of the converter to the voltage level of the battery and saturating the current through the AFE is enough to determine power transfer, however when the battery is integrated and fixed the DC is bound to its SoC so only the current can be regulated to determine power transfer. The latter is inherently better in the considered scenario, because of the ability to regulate both direct and quadrature portions of the current (more on this in Chapter 3). Both schemas are electrically equivalent and reported in Figure 5. In the first case the current is determined by Eq.2.1 while the second case refers to Eq.2.2.

$$I_{dc} = \frac{V_{dc} - V_{bat}}{Z_{bat}} \rightarrow V_{dc} = Z_{bat} I_{dc} + V_{bat} \tag{2.1}$$

Where I_{dc} is the desired current transfer (associated to power $V_{bat} I_{dc}$) and Z_{bat} is the equivalent impedance of the batter, a priori not known, so the regulation algorithm needs to feedback the actual current to regulate voltage accordingly.

$$P = V_{dc} I_{dc} = k * V_{ac} I_{ac} \cos(\phi) \tag{2.2}$$

Where k is a coefficient depending on the grid connection (i.e., one or three phase), V_{ac}, I_{ac} are intended as phasors and $\cos(\phi)$ is the is the power factor. In this way both dc current and power factor can be controlled, granting more possibilities for grid regulation and all the advanced functionalities expected from the electrification of mobility.

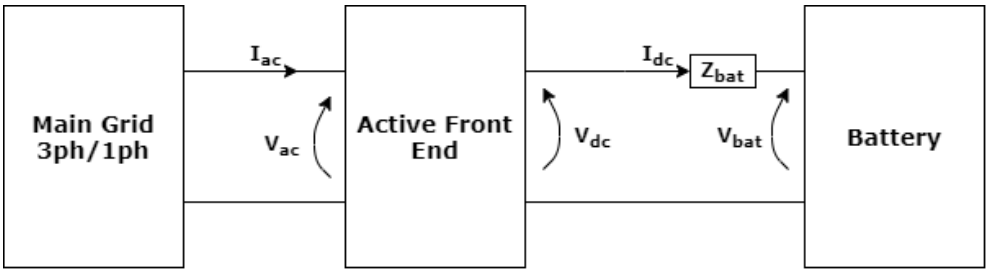

Figure 5 AFE electrical interaction with Battery

The battery representation in Figure 5 is an aggregation of the possible EV battery and the accumulation system in the system. A more complete model is needed to assess the power flow of the system, so the battery is split in two and individual flows are characterized by their effects system wide. As shown in Figure 6:

$$\begin{cases} 11\ kW > P_{GRID} \cong P_{AFE} \\ P_{AFE} = P_{EV} - P_{BES} \end{cases} \rightarrow P_{BES} \cong P_{EV} - P_{GRID} \tag{2.3}$$

Where P_{GRID} is the power exchanged with the grid, P_{AFE} is the power through the Active Front End, P_{BES} is the power transferred by the Battery Energy System and P_{EV} is the power requested by the EV. From Eq.2.3 it can be noticed that by knowing P_{EV} and P_{GRID}, P_{BES} can be calculated but only imposed when P_{GRID} can be controlled, and since the difference in voltage between the EV Battery and the BES is slight, and to decide power transfer in the DC-link an equation similar to Eq.2.1 applies, some configurations are more reachable by employing the control method with setpoint calculation of Eq.2.2.

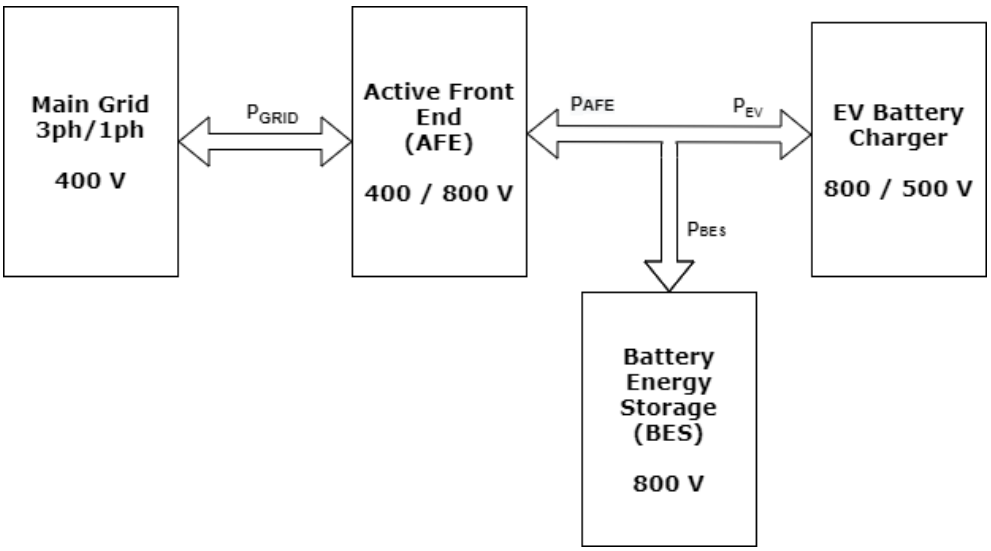

Figure 6 Power Flow of a Battery Energy System Integrated Fast Charger

To better understand this claim, battery behavior needs to be analyzed and understood, indeed two of the fundamental tasks of the BMS system are battery voltage measurement and SoC estimation, and to understand the intricacies of the process some common estimation algorithms will be introduced and studied as applied in the context.

2.2 BATTERY TECHNOLOGY OVERVIEW

Battery technology has evolved like never before in the past decades. As already mentioned, the battery mounted on EVs can reach up to 100 kWh, which is a testament not only to the energy they can stock, but the high performances in terms of weight and space as well.

In common BES usage for static storage of power however, battery structure used to be somewhat different that for mobile means of transportations, since the constraints for space and weight are laxer, seen as they do not decrease the mechanical characteristics (top speed, acceleration) as they would on an EV. Nowadays even static automotive solution, like the one presented in this thesis, use EV batteries for primary source of storage in what are called Second Life (SL) applications, so it is necessary to achieve greater understanding about which characteristics dominate the automotive industry.

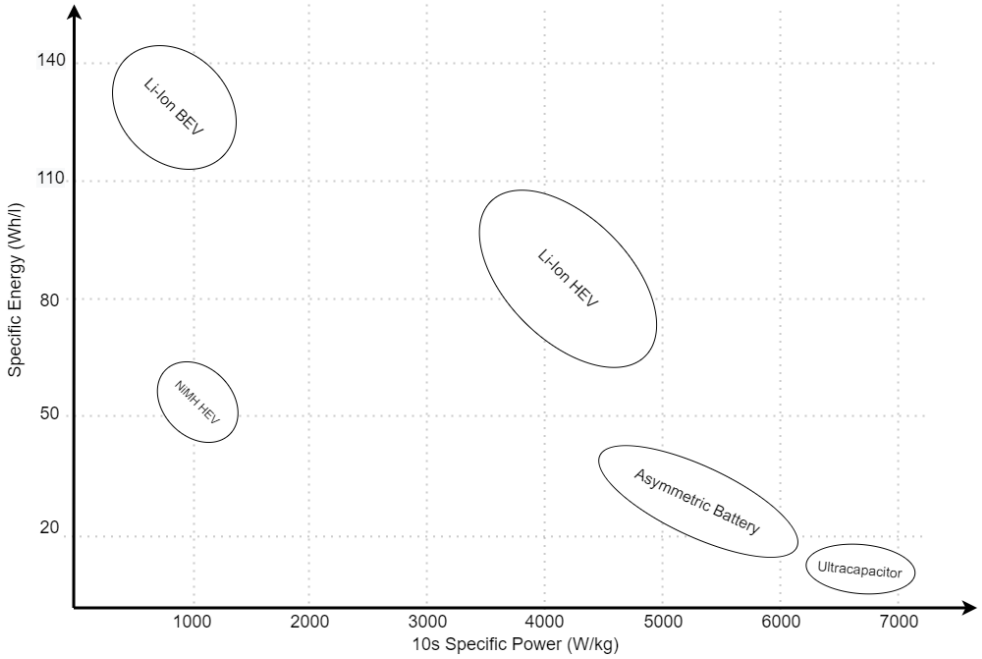

Figure 7 Energy density vs 10s Specific Power burst for different storage technologies

Specific power (W/kg) is highly significant in an EV because it directly plays a role in acceleration and performance of the vehicle. Energy density (Wh/l) is just as significant because there is a finite amount space to fit the battery pack in the shaft of the vehicle. Specific power focused battery pack are used in HEVs because they do not have to supply all the energy, as the greater part of the energy is handled by ICE. In the BEVs the battery is the only supplier of energy and so an excellent specific energy is desirable, but also a good specific power to aid in accelerations [14] as shown in Figure 7. Comparing batteries developed for HEVs to the one developed for BEVs might be misrepresentative because they have very different energy (kWh) requirements. In simpler terms HEVs battery are not asked to supply cruise energy and so can be way more performant in terms of power, however the industry is striving to close the gap between the two technologies as the transition continues to fully electric.

The life cycle of the batteries is also an important factor when comparing technologies. NiMH and Li-ion batteries are what is currently used in EVs and are more focused on energy density,

but other options like supercapacitors are available. The durability is mainly determined by the chemistry employed:

Nickel Metal Hydrate batteries are a mature technology and were the first batteries used in modern era. They offered greater specific power (70 Wh/kg) with respect to lead-batteries (30 Wh/kg) and weighted significantly less, so they had become the most obvious choice. The complete reaction in a NiMH battery is from left to right in Eq.2.3:

$$H_2O + M + e^- \leftrightarrow OH^- + MH \tag{2.3}$$

where M is an intermetallic compound which most commonly includes a rare-earth mixture of lanthanum, cerium, neodymium, praseodymium and nickel, cobalt, manganese, or aluminum as stated by various battery makers [15] [16]. Nowadays NiMH does not compare well with other kind of chemistries but still have upsides: it is cheap technology that has been very well developed. Unfortunately, cell voltage is low at 1.5 V per cell and that makes scalability a problem. Other issues include higher self-discharge rate and poor handling of heat development, also when overcharged H surplus accumulates [17] posing safety problems not only for the battery but for the driver, greatly diminish the life cycle this chemistry is able to achieve at higher powers.

Lithium-ion batteries are the most used source of power for HEVs and BEVs because of their advantages over other chemistries:

1. Higher operating voltages (3.7V). This means less cells can be used to reach a good operating voltage of the pack, which aids in cell equalization issues and reliability profiling.
2. Lithium-ion cells have a lower self-discharge rate than other rechargeable cells, which is especially useful in vehicles that might need to stay parked for long periods without losing charge.
3. Higher energy density.

Lithium batteries main problems are high manufacturing costs, expected to go down as EV penetration increases and sensitivity to overcharge, making the employment of a BMS with a good SOC estimate necessary.

Lithium batteries work differently from traditional cells: lithium does not react with the electrolyte, instead its either absorbed in the electrode, this process is called intercalation, or expelled by the electrode in the electrolyte in a process called deintercalation [18]. These reactions demand the electrodes to have two key properties:

1. Open-crystal structures
2. Conductive poles

Lithium is stored as an independent charge, and it is not bonded in the crystalline structure which makes it free to move, allowing it to diffuse and equalize concentration. During discharge lithium gives up an electron, which is supplied to the electrical load, and the ion Li+ exits the

crystalline structure of the cathode dissolving in the electrolyte. Conversely, lithium ions nearing the anode are absorbed by the crystalline structure and are given and electron. The process is reversible, and the intercalation process does not modify the chemical specie, so the battery as a longer life than traditional batteries. The rupture of the separator can happen in a few ways which affect the performance of the battery and will be addressed later in this thesis.

The double layer capacitor or Ultracapacitor (UC) is gaining momentum both in public awareness and research. New technologies have been sprouting all over the world, like hybrid busses, new start stop systems and innovative regenerative breaking that all use UCs. While hopes are high for a breakthrough as of today UCs are used as a secondary energy supply to the batteries, especially in EVs where high specific power is not achievable yet. When peak power demand must be met, the UCs comes into play, granting very high power in short burst thanks to their small series impedance, in the order of 0.1mΩ as found by [19]. Worth noting is their long-life cycle that would solve the maintenance problem the chemical batteries have. As disadvantages UCs have very little energy density (5Wh/kg), and the electrolyte decompose with great caloricity: upper bond temperature can even reach 100°C becoming of difficult employment in extreme environments. Another disadvantage is average functioning voltage (2.5 V).

Table 6 presents an overview of the different energy storage technologies: while ultracapacitor look really appealing and will see great development in the next few years, for now the Li-ion batteries are what is most used in EVs and what we will be focusing on form now. Values have been gathered by [19] [20] [21].

Table 6 Energy Storage Technologies Comparison

Battery Technology	Nominal voltage per cell [V]	Specific energy [Wh/kg]	Energy density [Wh/l]	Life cycles	Major Issues
NiMH	1.2-1.8	70	170	1500	Heat management, byproducts, Low energy, Impedance fluctuations
Li-ion	3.7	120	200	10000	Cost, separator management
Ultracapacitors	2.5	5	low	500000	Low energy density, low operating temperature

2.3 BATTERY MODEL

Every BMS needs a reference mathematical model to determine the state of charge (SOC) of the battery pack, meaning a good characterization of the behavior of the battery becomes important for accurate tracking. By tracking the evolution of not only the charge but of the parameters that constitute the model, that are intrinsically tied with internal phenomena of the cell, a good estimation of the SOH can be achieved. A list of all the indicators and parameters, and how they are affected by aging and other external factors is presented in order to craft an electrical equivalent model that suits the needs of the application.

2.3.1 State of Charge (SOC)

SOC is a factor ranging from 0 (discharged) to 1 (charged), that describes how charged the cell is and is defined by Eq.2.4:

$$SOC(t) = \frac{Q_r(t)}{Q_t(t)} \qquad (2.4)$$

Which is the ratio of the remaining charge $Q_r(t)$ over the total capacity of the cell $Q_t(t)$. Total capacity is a charge measure and is usually expressed in Ah and is a time-varying parameter of the cell model. It decreases as the cell ages due to unwanted chemical side reactions over many cycles, the effects can be estimated by degradation models, especially in the context of SL applications. Variation in the SOC of the cell can be described on a cycle-to-cycle basis with the first order differential equation in Eq.2.5 considering Q_t constant as Q.

$$\frac{dSOC(t)}{dt} = -\eta(t) * \frac{i(t)}{Q} \qquad (2.5)$$

Where η is the coulombic efficiency of the cell and changes with the sign of the current: its value is one when discharging and less than one when charging because some of the current does not contribute at the charging of the cell, instead it is spent on chemical side reaction that often cause battery degradation and $i(t)$ is the current flowing thorough the battery. Integrating the above equation yields Eq.2.6:

$$SOC(t) = SOC(0) - \int_0^t \eta(\tau)\frac{i(\tau)}{Q} \qquad (2.6)$$

Tracking $SOC(t)$ however is much more complicated because of the uncertainty on the initial condition, self-discharge, and measurement error. In general, the behavioral measuring model, if the complexity is kept at this one equation should also account for different temperatures, working conditions etc..., however the simplest models may only integrate the current as a source of estimation, accepting great variability in the result.

2.3.2 Open Circuit Voltage (OCV)

The open circuit voltage is the voltage measure at the terminals of the cells when the load current is zero, so the OCV does not depend on the current flow. Chemical cells usually deliver

a somewhat constant voltage regardless of the charge (that is what makes them better than supercapacitors) but also generally the OCV of a completely charged battery is higher than a completely discharged one, in this thesis the relationship between OCV and SOC is extrapolated from the characteristics of the components present in the laboratory, which have been tested by an external factory. The relationship can the written as a non-linear functional h with SOC, temperature T, time of cycle t_c and current sign as parameters as per Eq.2.7:

$$OCV = h(SOC, T, t_c, |i|) \tag{2.7}$$

h is not explicitly know, a lookup table instead determined by functional measurements. In common simulation scenarios only one plane of the solid created by the functional h is typically considered, however more complex simulations are possible. When considering the steady state function $t_c = t_{ss}$ and Eq.2.7 can be rewritten:

$$OCV = h(SOC, T, t_{ss}, |i|) = \begin{cases} h^{+}_{Tss}(SOC, T); & i > 0 \\ h^{-}_{Tss}(SOC, T); & i \leq 0 \end{cases} \tag{2.8}$$

Where $i > 0$ means charging and $i \leq 0$ discharging, Figure 8 and Figure 9 show OCV characteristics respectively, where it can be noticed that at lower temperatures the battery is not well behaved, so the battery pack is equipped with an internal heater to work usually over 10°C .

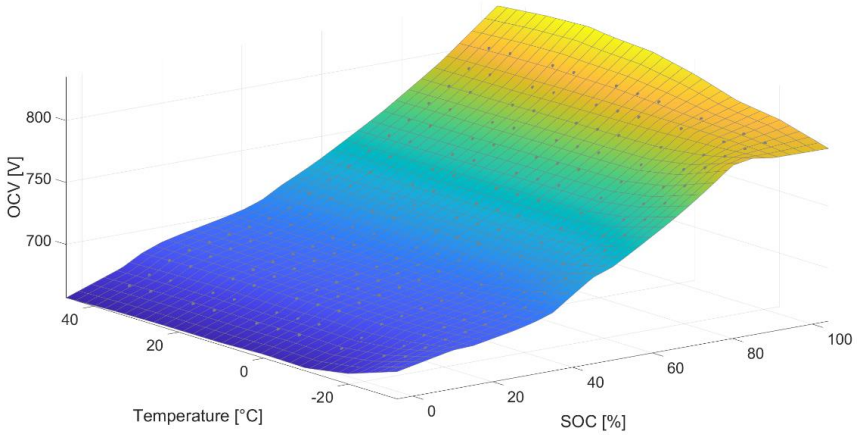

Figure 8 Charging OCV profile with dependence on SOC and Temperature

More realistically a specific ambient temperature (and so a thermal steady state) can be considered as shown in Figure 10 where it can be noticed that over 50% of SOC excursion is contained withing 70 V, justifying some hypothesis made later in this thesis about considering the voltage constant.

2.3.3 Equivalent Series Resistance (ESR)

When the battery pack is subjected to an external current, the voltage at the terminals of the cell drops below the OCV at that given time, due to resistance of the connectors and chemical side

reactions, this event can be modeled by placing a resistance (R_0) in series with the OCV generator, so the voltage at the terminals can be written as Eq.2.9:

$$v(t) = OCV(SOC, T, t_{ss}, |i|) - i(t) * R_0 \tag{2.9}$$

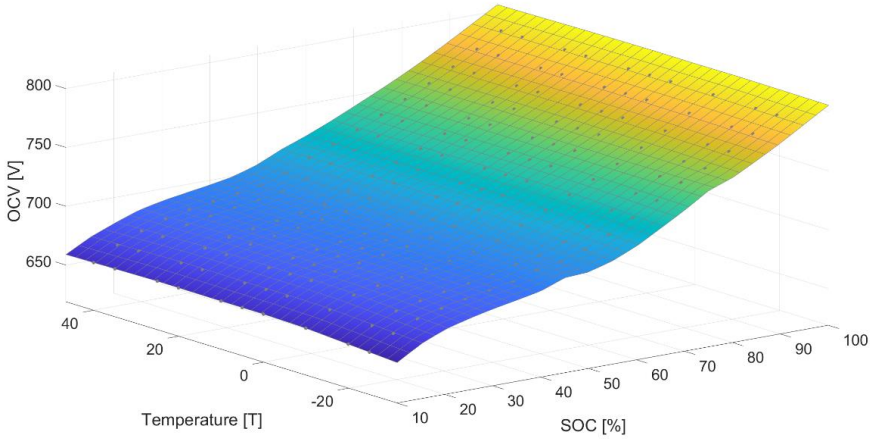

Figure 9 Discharging OCV profile with dependence on SOC and Temperature

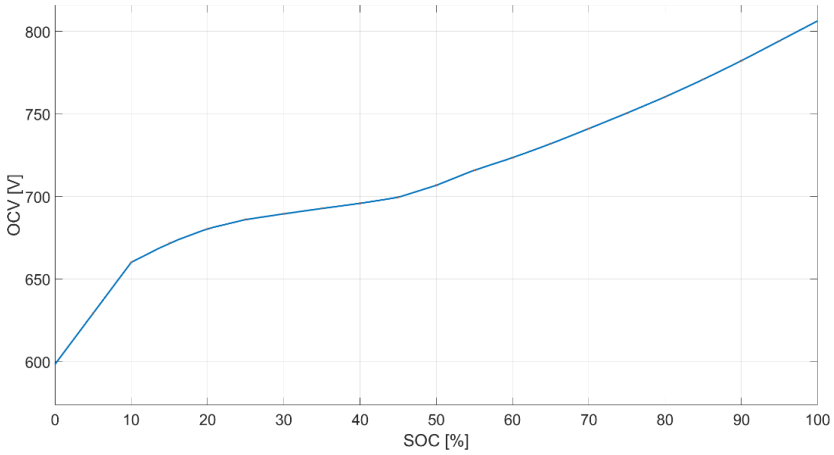

Figure 10 Charging OCV profile with dependence on SOC and Fixed Temperature 25°C

The ESR can also be considered variant with the same parameters of the OCV, so following the same procedure as before lookup table can be used to recreate the relationship as in Eq.2.10.

$$R_0 = h_R(SOC, T, t_{ss}, |i|) = \begin{cases} h^+_{R,Tss}(SOC, T); & i > 0 \\ h^-_{R,Tss}(SOC, T); & i \leq 0 \end{cases} \tag{2.10}$$

The discharging behavior of the ESR is represented in Figure 11 where the SOC and temperature working zone becomes obvious since the resistance increases tenfold at very low temperature and charge. At 25°C the battery behaves as in Figure 12, which is the optimal profile.

The presence of the resistance also plays a role in the energetic balance since it dissipates power, which basically describe the thermal behavior of the battery. A first order thermal model of the form in Eq.2.11 can be employed to dynamically change the temperature, however simpler techniques to determine the chilling power of the cooling circuit can be used, so that simulation time remains short.

$$P_D - P_C = \frac{\Delta T}{R_{b-a}} + C_b \frac{d\Delta T}{dt} \tag{2.11}$$

Where P_D is the dissipated power of the cell, P_C is the chilling power, ΔT is the gradient temperature between the battery and the ambient, R_{b-a} is the thermal resistance between the battery and the ambient and C_b is the thermal capacity of battery shaft. Since $P_D = i(t)^2 * R_0$ which is in general dependent on temperature considering the full model can become complicated, so as Figure 12 shows, the value can be considered constant for all values above 20% of SOC. This simplification allows for the determination of P_C as:

$$P_C = P_{D,max} - \frac{\Delta T_{max}}{R_{b-a}} \tag{2.12}$$

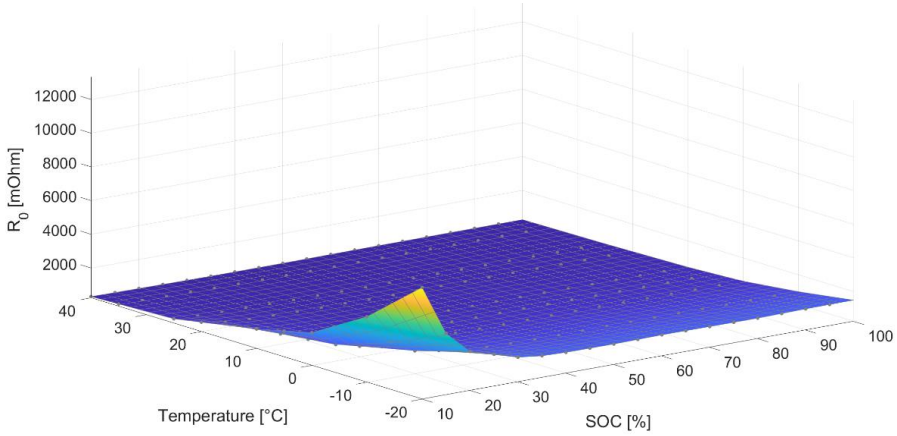

Figure 11 Discharge Resistance profile with dependence on SOC and Temperature

$P_{D,max}$ is related to the maximum scheduled current transfer and ΔT_{max} is the maximum allowable over temperature with respect to the ambient.

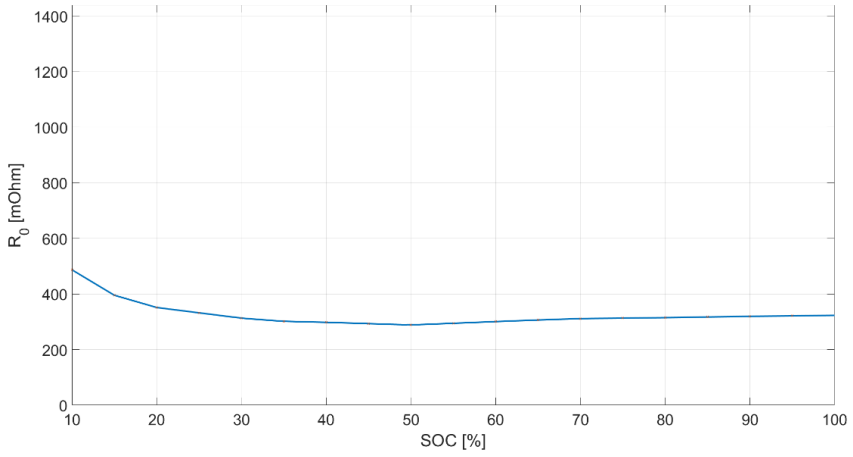

Figure 12 Discharge Resistance profile with dependence on SOC and Fixed Temperature 25°C

2.3.4 Diffusion Voltage

When the battery is turned off after an active cycle, the voltage $v(t)$ at the electrical terminals of the battery should rise from $v(t)$ to $OCV(SOC, T, t_{ss}, |i|)$ since $i(t) = 0$ as per Eq.2.9 , however the process is not instantaneous: the phenomena is caused by diffusion in the cells which partially restores ion imbalance and it is called diffusion voltage. An equivalent electrical model, in Figure 13, can be mimicked by imagining a parallel of a capacitor (C_1) and a resistance (R_1) in series with the ESR. When the load is connected the capacitor charges up to the value $R_1 * i(t)$, when the load is disconnected the factor $R_0 * i(t)$ drops to 0 and the voltage on the capacitor slowly goes to 0 over the duration of 4 $R_1 * C_1 = 4\tau$, as a result the voltage slowly rises.

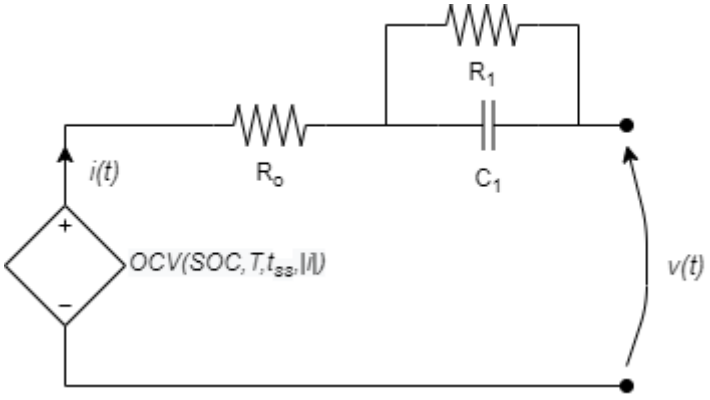

Figure 13 2nd Electrical Model of a battery

The battery voltage at the terminal under nominal conditions (when T and SOC are in the appropriate ranges) is modeled as in Eq.2.13:

$$\begin{cases} \dfrac{dSOC}{dt} = \eta(t) * \dfrac{i(t)}{Q} \\ \dfrac{dv_c}{dt} = -\dfrac{1}{C_1 R_1} v_c + \dfrac{i(t)}{C_1} \\ v(t) = OCV - R_0 i(t) - v_c(t) \end{cases} \tag{2.13}$$

Estimation of parameters can be performed in a few ways however the "current pulse characterization method" is the most used [22] [23]. The test consists in charging or discharging the EUT with a pulse of current for a set time and monitor the evolution of the voltage. After the end of the current pulse, when the voltage is stable within a percentage of the final excursion (usually 5%,) model fitting is applied to the data, in the case of a 2nd order model, as represented Figure 14, however the parameters can easily be calculated as per Eq.2.14-16.

$$R_0 = \frac{v(t_2) - v(t_1)}{I} \tag{2.14}$$

$$R_1 = \frac{v(t_3) - v(t_2)}{I} \tag{2.15}$$

$$4\tau = t_3 - t_2 \rightarrow C_1 R_1 = \tau \rightarrow C_1 = \tau * \frac{I}{v(t_3) - v(t_2)} \tag{2.16}$$

The test is then repeated for different temperatures and at different SOC levels until a surface like the one in Figure 11 is determined. Unfortunately, in this case numeric characterization of the series polarization impedance was not available, however since long time cycle is been considered the measurable effects should not impact performance, only SOH estimation.

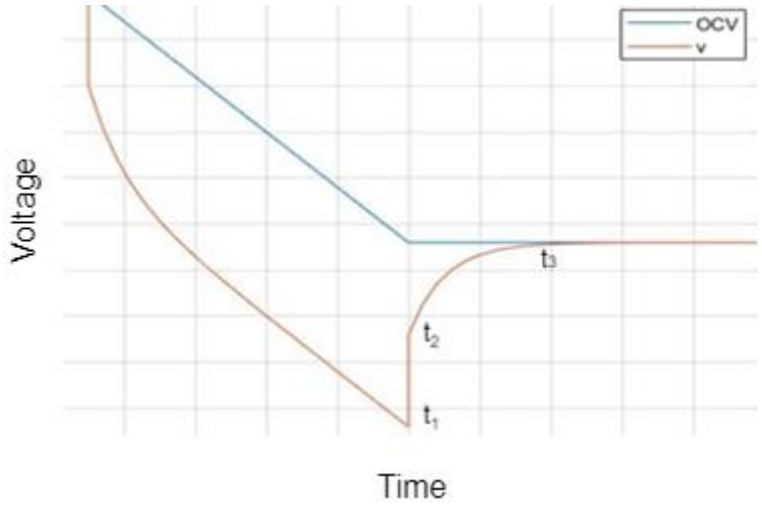

Figure 14 Typical voltage evolution under pulsed current

2.3.5 Higher Order Models

Higher order models have been studied [24] [25] to better characterize battery behavior, in these models further, more complex, impedance branches are added in series with the basic model previously described, to account for lesser order chemical phenomena. The parameters introduced until now R_1, C_1 explain the diffusion voltage process, which is heavily impacted by the SOH of the battery, due to the creation of Solid Electrolytic Interface (SEI) over time, likewise further parameters can be used as an indicator for the estimation of the battery life cycle. Faradic impedance consists of double layer capacitance (C_2) and charge transfer resistance (R_2). These depend on the porosity and tortuosity of the electrodes, meaning different chemistries offer different performances, however the main behavior of the battery is conserved, hence they are considered less important to the fidelity of the model. The Faradic impedance is frequency dependent, has a role on transients and is expressed along with Warburg impedance in Eq.2.16 which better describes diffusion processes.

$$Z_w(j\omega) = (1 - j) * \frac{\sigma}{\sqrt{\omega}}$$
$$\sigma = \frac{RT}{n^2 F^2 A\sqrt{2}} \left(\frac{1}{C_O \sqrt{D_O}} + \frac{1}{C_R \sqrt{D_R}} \right) \tag{2.16}$$

Where, σ is the Warburg Coefficient, F is the Faraday constant, A is the surface area of the electrode, R is the gas constant, T is the absolute temperature, C_o and D_o are the concentration and diffusion coefficient of the oxidant, while C_R and D_R refer to the reductant. Parametrization

of the model in Figure 15 is more complex, and it relies on model fitting from pulsed current tests as well as inductance spectroscopy.

Higher order models add new layer of complexity in BMS algorithms for parameters and state estimation, especially in real time applications and so they are scarcely used. In most prototypal studies ([26] [27] [28] [29]) a less refined mathematical model is preferred, a tradeoff between effectiveness and simplicity is always necessary to ensure good tracking of the experiments.

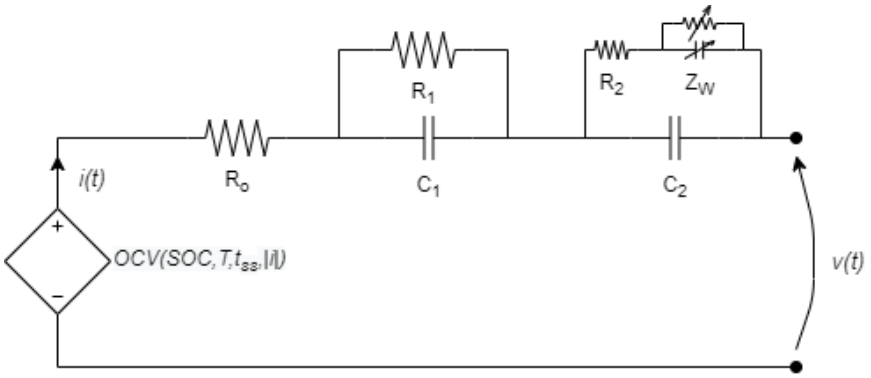

Figure 15 Higher order model of a battery

2.3.6 Battery Degradation Model, Second Life and Battery Energy System Sizing

Mass adoption of EV will be the epicenter of the carbon fossil energy transition policies in transportation. Millions of batteries will need to be made readily available in the market during the next decade, if there is any chance to complete the transition successfully. Incidentally as EVs evolve and older battery get dismissed the market will be flooded with used batteries; reusing EV batteries would provide an alternative revenue stream for a sub-product that otherwise would be at disposal stage, and this fact is increasingly getting the attention of important Original Equipment Manufacturers (OEMs). Moreover, this represents an alternative to other ESS, which could defer the manufacturing of new systems, leading to considerable environmental footprint mitigations. Since only a small portion of total battery life can safely be used in EVs, in what is called First Life (FL), less demanding and more controlled applications are a possible destination for older batteries, during what is called Second Life (SL).

The parameters and performances of the battery cells decrease over time and use, due to side reactions or other environmental factors, especially when considering the employment of SL BES. Aging is relentless and leads ultimately to system failure. Corrosion is the main agent of cell aging and happens differently based on battery chemistry: in a li-ion cell the most common sign of corrosion is called aspassivation. This effect creates a layer on the surface of the graphite cathode, known as solid-electrolyte-interphase or SEI film, that stops further reactions from happening locally. The SEI film slowly builds up over time and hinders the possibility of reaction, lowering the capacity of the cell, but fortunately the process is slow. Another side reaction of the lithium cell is the production of dendrites in the electrodes, as these crystals grow, they reduce the effective area of the electrodes, increasing the equivalent resistance from the electrical point of view, and so reducing the power the cell can output. These treelike metallic structures can lead to self-discharge increase, and self-short circuit because they can

cause structural damage to the cell, such as breaking through the separator. Intercalation based cell also suffer from volume changes that can damage the case and binder materials leading to increased internal impedance. Further studies can be found at [18] and [30].

The percentage increase in equivalent resistance is commonly used as the chief parameter to determine the advancement in life of the battery, along with total capacity. The state of health (SOH) can be defined as:

$$SOH(t) = \frac{Q_t(t)}{Q_t(0)} = \frac{Q_r(t)}{SOC(t)Q_t(0)} \tag{2.17}$$

Where $Q_t(t)$ is the total charge at the instant t. Clearly the SOH affects the SOC behavior and vice versa, so aging models are indispensable to ensure the battery retains economic sense for repeated use.

The root cause of aging has been described but, in a general sense, two modalities of accounting for it can be discerned, which serve different purposes: one of economic nature and the other related to electrical performances. They are strictly tied with the normal life cycle of a battery, which is often decided by static threshold, however a great many studies suggest that a differentiation might be needed based on the SL application of the specific unit. Considering the SOH, the battery life can be divided in 5 phases as in Figure 16. During the FL the EV battery is characterized by factory specifications and is considered at 100% capacity, after wear and tear of normal EV charge and discharge cycles sets in the battery slowly loses capacity and enters that near 80% SOH range that typically denotes the end of EV usage. After dismounting the unit, it should undergo more in depth testing to certify the SL initial status, also because the value of SOH was a rough estimate tracked by the EV's BMS and a more precise one is needed. After second parametrization is done the battery can be used for less intensive cycles, such as peak shaving or, in this case, embedded fast charging. The more intensive tasks, such as PV field peak shaving, where MW can be interested, should be assigned to the best batteries, avoiding frequent swaps and the annexed costs. Study [31] shows, for given load profiles, at different PV penetration factors how much a kWh is economically worth per battery and concludes that the optimal position for battery longevity highly depends on installed capacity, meaning better initial SOH.

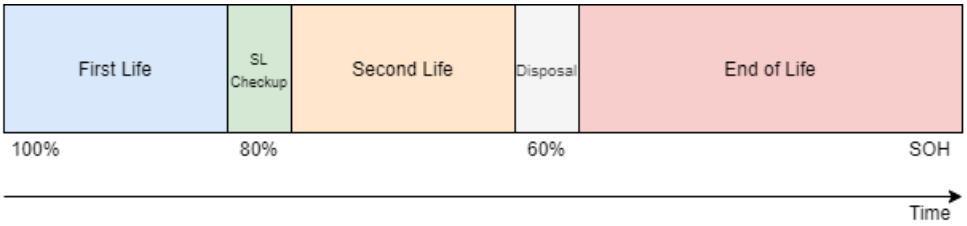

Figure 16 Battery Life Cycle

A first method of tracking the SOH of a battery consists in tracking the evolution of the passive parameters that define the cell, in models like the one defined in Eq.2.12. This is usually done by running an estimation algorithm on the BMS. When the parameters reach threshold measures the battery is considered End of Life (EOL) [32] [33]. While this is convenient as it can be real time based and directly connects the model with performance (e.g. the ESR is directly related

to heat generation) the actual estimate of the SOH can be hard to predict without scheduled testing of full charge and discharge cycles. The topic will be expanded later where the BMS is considered.

A priori thermo-chemical aging models, also known as calendar models, can be used to propagate the effects of using a certain battery in SL applications if load cycles are available. These models are suitable to complete constraint conditions when min/max problems are considered since they output a direct estimate of the SOH. Most studies find that loss of capacity depends on $t^{\frac{1}{2}}$, temperature and current, however the latter can be accounted in a cycle-to-cycle model loss [34] . The calendar loss of capacity can be estimated via an Arrhenius function as:

$$\Delta Q_{cal}(t, T_B) = Q_t(t_{BOL}) A_{cal} e^{-\frac{E_A}{RT_B}} \sqrt{t} \tag{2.18}$$

Where t_{BOL} is the time of Beginning of Life (BOL), A_{cal} is a scaling constant in $months^{-\frac{1}{2}}$, E_A is the activation energy of the cell, R is the Boltzmann Constant and T_B is battery temperature in K. Accounting for cycle loss of capacity is inherently harder since cycle dynamics are heavily dependent on many factors such as: electrode chemistry, age of the cell, current and temperature. many studies evoke a counting method where cycles provoke a fixed loss in capacity, this method however fails to account for the high variability of power in different applications [35]. To determine a method that accounts for SOC levels and current during the cycles a modified counting method can be imagined: the SOC dependency is considered by taking the nameplate cycle reduction in maximum charge of $Q_{t,BOL} \frac{1-\Delta SOH_{EOL}}{N_t}$, where $Q_{t,BOL}$ is the total charge in Ah at the battery at BOL, ΔSOH_{EOL} is the total SOH loss allowed and N_t is the nameplate number of cycle at 1C and multiplying it by $\left(\frac{i}{1C}\right)^z$ which is the ratio of cycle current and 1C elevated to an exponent z to account for the non-linearity of the degradation process. The cycle loss of total charge is written in Eq.2.19.

$$\Delta Q_{cycle,N} = Q_{t,BOL} \frac{1 - \Delta SOH_{EOL}}{N_t} \left(\frac{i}{1C}\right)^z \tag{2.19}$$

In order to correctly size the battery a criterion must be chosen to serve as optimization parameter. Logically a reduction in total cost of investment in installed energy can be taken, however this would lead to under sizing the system so instead an investment-per-projected year approach minimization criterion is used instead. Eq.2.20 describes the total cost of the battery C_{BES}, where $c_{Wh}$is the cost per Wh, E_{BES} is the nominal energy storage in Wh, $c_{Wh,BOL}$ is the cost at BOL, k is a factor that accounts for the de-pricing of the battery during lifetime and V_{AVG} is the average functioning voltage of the battery, which considering constant current can be evicted from the OVC-SOH curve. The cost function F of Eq.2.21 describes the investment-per-year, where t_{EOL} is the number of months before the BES reaches EOL and SOH_{SL} is the SOH where SL starts.

$$C_{BES} = c_{Wh} E_{BES} = c_{Wh,BOL} e^{k(1-SOH_{SL})} V_{AVG} Q_{t,BOL} \tag{2.20}$$

$$F\left(Q_{t,BOL}, t_{EOL}\right) = 12 * \frac{C_{BES}}{t_{EOL}} \tag{2.21}$$

The t_{EOL} estimate can be achieved by sizing a constraint function that determines it in function of $Q_{t,BOL}$:

$$t_{EOL} \;\; s.t. \;\; \frac{Q_t(t_{EOL})}{Q_{t,BOL}} = 1 - \Delta SOH_{EOL} \rightarrow \frac{SOH_{SL} Q_{t,BOL} - \Delta Q_{t,SL}(t_{EOL})}{Q_{t,BOL}} = 1 - \Delta SOH_{EOL} \tag{2.22}$$

Where $\Delta Q_{t,SL}(t)$ is the gradual loss of total capacity and is given by Eq.2.23 and $N(t)$ is that number of completed cycle at time t.

$$\Delta Q_{t,SL}(t) = \Delta Q_{cal}(t) + \Delta Q_{cycle.N} * N(t) \tag{2.23}$$

Finally the constraint function $H(SOH_{SL}, Q_{t,BOL}, t_{EOL})$ can be written:

$$H\left(Q_{t,BOL}, t_{EOL}\right) = \\ = \frac{SOH_{SL} Q_{t,BOL} - \left(SOH_{SL} Q_{t,BOL} A_{cal} e^{-\frac{E_A}{RT_B}} \sqrt{t_{EOL}} + Q_{t,BOL} \frac{1 - \Delta SOH_{EOL}}{N_t} \left(\frac{i}{Q_{t,BOL}} \right)^z N_t(t_{EOL}) \right)}{Q_{t,BOL}} - (1 - \Delta SOH_{EOL}) \tag{2.24}$$

The minimization problem can therefore be summarized as in Eq.2.25 where the optimized variables have been given numerical constraint to suit given application:

$$\min_{Q_{t,BOL}, t_{EOL}} F\left(Q_{t,BOL}, t_{EOL}\right) \;\; s.t. \;\; \begin{cases} H\left(Q_{t,BOL}, t_{EOL}\right) = 0 \\ Q_{t,BOL,min} < Q_{t,BOL} < Q_{t,BOL,max} \\ t_{EOL,min} < t_{EOL} < t_{EOL,max} \end{cases} \tag{2.25}$$

To obtain the values of $Q_{t,BOL}, t_{EOL}$ optimized by the cost function the models need to be parametrized in accordance with experimental data. Eq.2.18-20 are subject to some variability depending on the data used to model fit them. Calendar aging parameters A_{cal} and E_A by surveying the number of months the battery is expected to live in quasi static condition. It is well known that temperature has a grave effect on life expectancy of the battery and so it will greatly diminish the number of months before EOL [36]. Effectively choosing two pair of coordinates $(t_{EOL}|_{i=0}, T_B)_{1,2}$ the parameters of Eq.2.18 can be determined as per system in Eq.2.26:

$$\begin{cases} \Delta Q_{cal}((t_{EOL}|_{i=0}, T_B)_1) = Q_{t,BOL} A_{cal} e^{-\frac{E_A}{RT_{B_1}}} \sqrt{t_{EOL,1}} = \Delta SOH_{EOL} Q_{t_{BOL}} \\ \Delta Q_{cal}((t_{EOL}|_{i=0}, T_B)_1) = Q_{t,BOL} A_{cal} e^{-\frac{E_A}{RT_{B_2}}} \sqrt{t_{EOL,2}} = \Delta SOH_{EOL} Q_{t_{BOL}} \end{cases} \tag{2.26}$$

Similarly for $\Delta Q_{cycle,N}$, accounting for current dependency, surveying battery testing studies for automotive purposed battery, in the range 0.5C to 2C, the parameter z can be guessed by recognizing that at 1.5C battery are expected to last up to 2 times less and instead a 0.8 C the duration of life can be increased of up to 20% [37] [38] [39]. The expected loss in terms of SOH for each cycle is around the 0.02% at the rate of 1C. Finally the specific energy cost of the battery in Eq.2.20 is taken as exponentially decreasing in the range of SOH for SL considered,

meaning that fixing the price point at the extremes of that range would finally yield an estimate of the decrease.

The problem of Eq.2.25 is solved using MATLAB for the following parameters:

$$(t_{EOL}|_{i=0}, T_B)_1; (t_{EOL}|_{i=0}, T_B)_2 = (200\ months, 25°C);\ (70\ months, 55°C);$$

$$C_{Wh} = 150 \frac{\$}{kWh}$$

$$\Delta SOH_{EOL} = 0.4; N_t = 5000;\ N(t) = 25t; V_{AVG} = 750\ V; i = \frac{50\ kW}{750\ V}, k = 1.35; z = -4.7$$

$$Q_{t,BOL,min} = 53.33\ Ah;\ Q_{t,BOL,max} = 133.33\ Ah;\ t_{EOL,min} = 5\ yr;\ t_{EOL,max} = 10\ yr.$$

The nonlinear constraint that models battery duration in function of initial SOH of SL and embedded battery capacity is shown in Figure 17, higher capacity last longer due to the effective diminished C-rate.

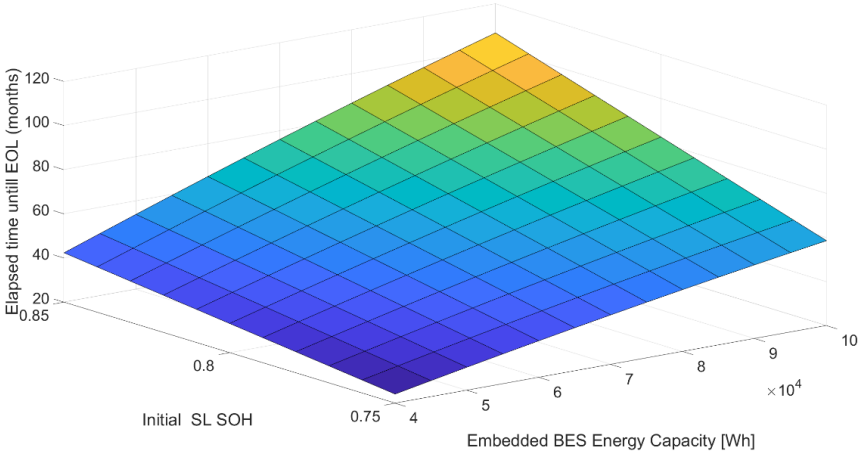

Figure 17 Battery SL length as a function of capacity and initial SL SOH

The region constraints $Q_{t,BOL,min} = 53.33\ Ah;\ Q_{t,BOL,max} = 133.33\ Ah;\ t_{EOL,min}$ have been chosen so that the model would remain valid first and foremost, however these are possible estimates of a real application where space in the storage cabinet for the BES is finite, also a minimum $Q_{t,BOL,min}$ needs to ensure the feasibility of the battery voltage V_{AVG} so that the sum of the singles cells in a series minimum configuration reaches that value. The cost function is characterized by the parameter z which has been calculated by supposing a de-pricing for 50% to 30% in the considered SOH range.

The outputs of the minimization problem hare shown in Figure 18, Figure 19 and Figure 20 against a range of initial SOH of SL spanning for 0.75 to 0.85. Figure 18 shows that for optimized cost a bigger battery is needed for higher levels of SL SOH, this is due to the increased investment cost that introduces the need for a more durable product. In this case the C-rate spans from 0.9 to 0.73 decreasing the cycle losses from 90% to 70% circa which shows the optimal point for battery life duration. These figures might be overestimated thus making a possible real estimate flatter with the C-rate.

The estimated optimal battery duration is shown in Figure 19, if a battery that lost upward of 5 years is needed SL SOH of 0.8 and above need to be considered, however a more expensive

initial investment will obviously be required. It is imaginable that SL batteries will be divided by batch when re-characterized, so price point may change based on availability, making lower SOH rated batteries more viable.

Finally, in Figure 20, which shows the optimal investment per year, the best SOH SL factor can be recognized at around 0.835, which for the considered problem modeling could set the standard for beginning of SL for maximum battery value, however the investment per year for lower rate SOH SL batteries only increases of around 12% at the lower span.

2.4 BMS

The battery management system is surely one of the fundamental components when dealing with BES. The BMS is generally tasked with overwatching a great many variables inside the BES, and on its measurements and estimates is based most of the control logic regarding safety, functioning range, and efficiency [40]. The main tasks of a BMS are:

- Monitoring voltage, current, power flow, internal temperature, SOC and SOH, capability estimation. Electrical parameters are easier to estimate, while SOC and SOH can become troublesome especially in real-time.
- Balancing of battery cells voltage, due to uncertainty in the manufacturing cells usually have different capacity or nominal voltage.
- Safety of operation, such as preventing short circuits and high temperatures in the battery, ensuring that the separator is integer.

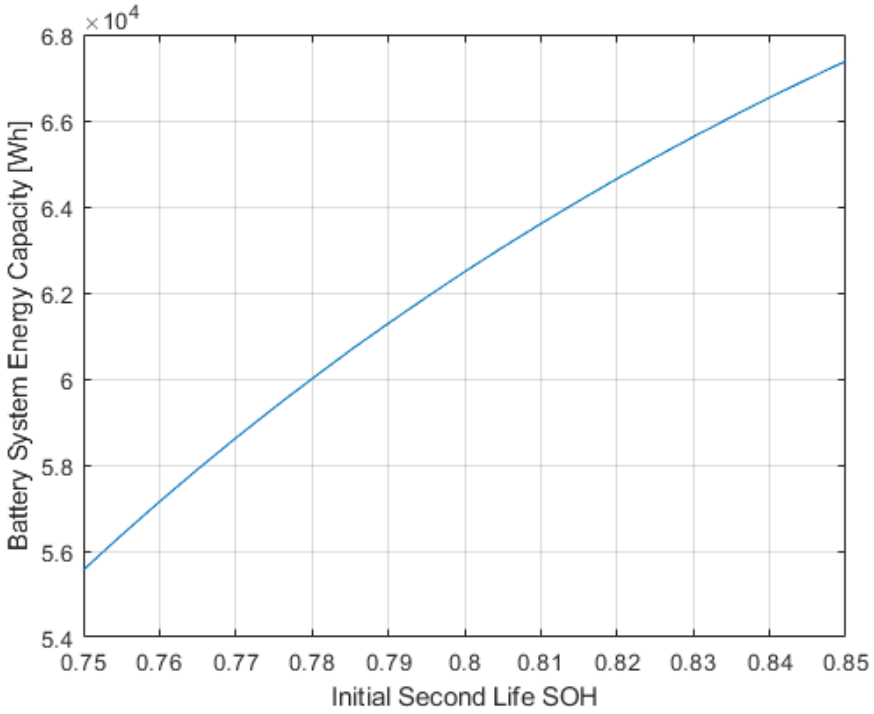

Figure 18 Optimized Embedded BES Energy Capacity in function of SL initial SOH

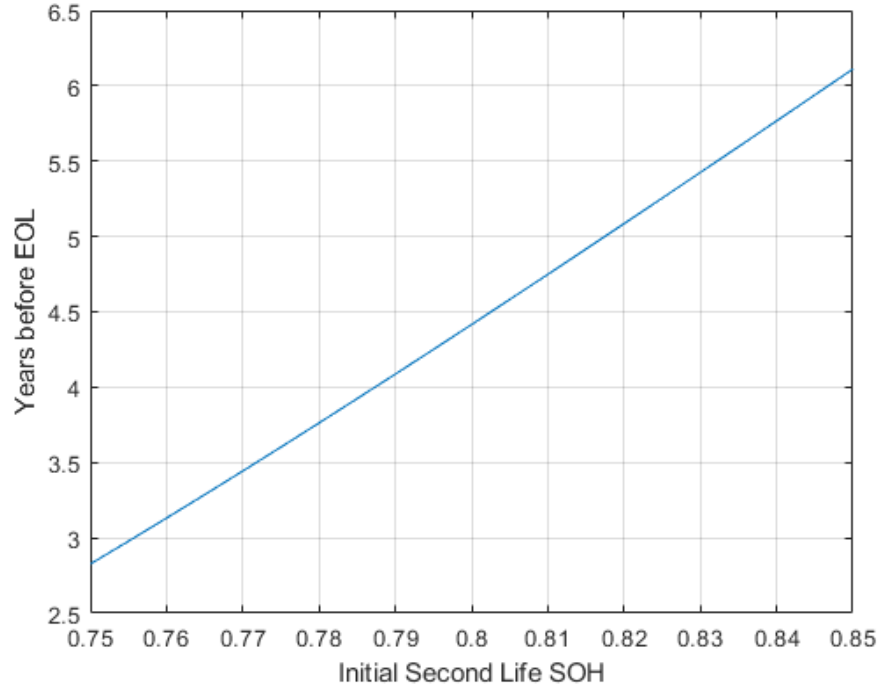

Figure 19 Optimized SL duration in function of SL initial SOH

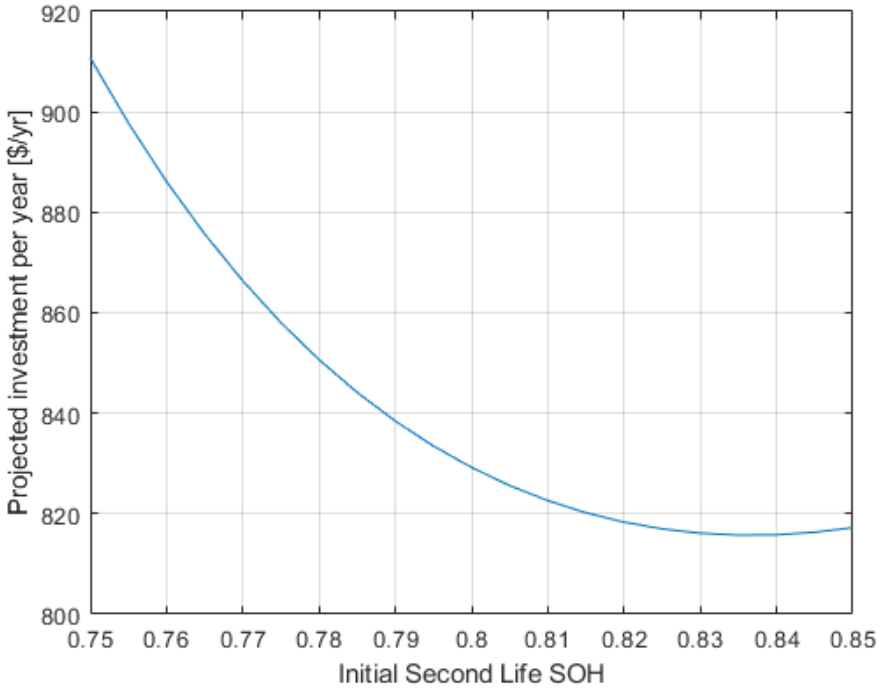

Figure 20 Optimal investment per year in function of SL initial SOH

Using cells voltage measurements, the BMS is also tasked to equalize SOC of each cell. Cell-to-cell balancing has two approaches:

- Passive balancing

  Drains the surplus of charge from the overcharged cells using a shunt resistor with a switch controlled by the BMS. This dissipates the energy as heat lowering efficiency

and increasing caloricity, but this kind of balancing circuit is very cheap and may be suited for low-end applications.

- Active balancing

  Moves the surplus of charge from the overcharged cells to the undercharged cells, conserving energy and increasing efficiency, the circuitry required can be however expensive.

In order to achieve all these tasks the BMS must record the measurements made by the connected peripheral and implement estimations algorithms to account for uncertainties of measurement, parametrization errors and nonlinearities in the system.

2.4.1 SOC Estimation Algorithms

SOC estimation is crucial for most operations in almost any application, SOH also plays a role in SOC estimate because the OCV-SOC curve changes as the maximum capacity decreases. The OCV-SOC curve is considered to remain largely the same if reported to the operating maximum capacity:

$$Q_t(t) = SOH(t)Q_t(0) \tag{2.27}$$

As said measuring SOH is difficult, however low C-rate charge and discharge cycle can be run periodically to estimate battery capacity, effectively rerunning a brief characterization test like the one described previously. Next some SOC estimations methods will be introduced to employ in simulations model, effectively deciding the complexity of the simulation model of the battery itself.

2.4.1.1 Coulomb Counting (CC)

The CC method is based on the low-level knowledge of total charge storable in the battery, previous charge level and charging/discharging efficiency of Eq.2.5 ($\frac{dSOC(t)}{dt} = -\eta(t) * \frac{i(t)}{Q}$). By integrating the SOC can be calculated as:

$$SOC(t_{N+1}) = SOC(t_N) - \int_{t_N}^{t_{N+1}} \eta(t) * \frac{i(t)}{Q} dt \tag{2.28}$$

Where t_N is the finishing time of the n-th cycle of charge of discharge. The method is based on correctly measuring the whole current flowing through the BES; however it is theoretically impossible due to measurements errors and self-discharge current, which can never be captured by instruments. The error can be accounted for by saying that for a long set of cycles $(N, \dots, N+n)$ the remaining part of the error is:

$$SOC(t_{N+n}) = SOC(t_N) - \sum_{i=0}^{n} \int_{t_{N+i}}^{t_{N+i+1}} \eta(t) * \frac{i_M(t) - e_i(t)}{Q} dt = SOC_M(t_{N+n}) \underbrace{- \sum_{i=0}^{n} \int_{t_{N+i}}^{t_{N+i+1}} \eta(t) * \frac{e_i(t)}{Q} dt}_{E_n} \tag{2.29}$$

Where i_M is the measured current, e_i is the measurement error, $SOC_M(t_{N+n})$ is the measured SOC as per Eq.2.28 in the measurement and E_n is the average of the error reported on the SOC. If n is big enough then the non-polarized part of the error will average out, so as long as the SOC remains far from the operating limits no risk in the error occurs. The self-discharge rate correction can be accounted for by a fixed loss of SOC every period of time when the battery is unused. The CC method is never used "pure" however because it does not refer to the SOC to OCV curve, so voltage measurement never corrects the charge measurement losing a great deal of information.

2.4.1.2 Extended Kalman Filter (EKF)

The EKF is an iterative process that compares measurements and model estimates, enhancing the precision of both by calculating a reliability gain called Kalman Index. It does so by making a prediction through a mathematical model and comparing it with new measurement data via an estimate covariance matrix, finally the new state is obtained by mixing the prediction and measurement [41]. It is intrinsically more precise than CC because it relies on experimental curves and an electrical model of the battery to predict errors, which are typically nonlinear [42].

Define the following, where $u_{n|m}$ denotes a variable predicted for step n with data up to step $m < n$ and u_k denotes a static indicator or a measurement for step k:

- x the model state variables
- F the model transition matrix
- B the control input matrix
- w the process noise with zero mean and covariance Q s.t. $W \sim N(0, Q)$
- I the battery current measurement
- V the battery voltage
- v the measurement noise s.t. $v \sim N(0, R)$

The 2nd order model of Eq.2.13 can be discretized and used for the digital implementation of an EKF as in Eq.2.30. The measurements can only be recorded at the electric terminals so only $v(t), i(t)$ are available in addition to the temperature of the battery.

$$\underbrace{\begin{bmatrix} SOC_{k+1|k} \\ v_{c,k+1|k} \end{bmatrix}}_{x_{k+1|k}} = \underbrace{\begin{bmatrix} 1 & 0 \\ 0 & 1 - \dfrac{Ts}{C_1 R_1} \end{bmatrix}}_{F} \underbrace{\begin{bmatrix} SOC_{k|k} \\ v_{c,k|k} \end{bmatrix}}_{x_{k|k}} + \underbrace{\begin{bmatrix} \eta * \frac{\mathrm{Ts}}{\mathrm{Q}} \\ \dfrac{Ts}{C_1} \end{bmatrix}}_{B} [I_{k+1}] + w \tag{2.30}$$

$$V_{k+1|k} = h'(x_{k+1|k}, T_B, I_{k+1})$$

Where T_s is the sampling time.

$V_{x_{k+1|k}}$ is calculated via the OCV-SOC curve (as defined in Eq.2.7) and the last equation of Eq2.13. Namely it can be written as Eq.2.31 and is a function of the state variables and model inputs:

$$V_{x_{k+1|k}} = h(SOC_{k+1|k}, T_B, t_{ss}, |I_{k+1}|) - h_R(SOC_{k+1|k}, T_B, t_{ss}, |I_{k+1}|)I_{k+1} + v_{c,k+1|k} \quad (2.31)$$

Eq.2.31 can be linearized:

$$V_{x_{k+1|k}} \cong V_{x_{k|k}} + H_k(x_{k+1|k} - x_{k|k}) \quad (2.32)$$

Where H is the Jacobian linearization matrix calculated at the previous step composed by:

$$H_{k+1} = \left[\left(\frac{dh}{dSOC}|_{x_{k|k}} - \frac{dh_r}{dSOC}|_{x_{k|k}} I(k)\right) \quad -1\right] \quad (2.33)$$

So that $V_{k+1|k}$ can be modeled as a linear system and compared with the measurement V_{k+1}. The filter operates in 2 steps: prediction and update. During the prediction, only data up to time step k is available so $x_{k+1|k}$ denotes the predicted state variables value as per Eq.2.30. At the same time, the estimate covariance matrix $P_{k+1|k}$ is predicted:

$$\begin{aligned} x_{k+1|k} &= Fx_{k|k} + BI_{k+1} \\ P_{k+1|k} &= FP_{k|k}F^T + Q \end{aligned} \quad (2.34)$$

During update the next step $x_{k+1|k+1}$ and $P_{k+1|k+1}$ are calculated via the innovation Y_{k+1} and the Kalman Gain K_{k+1}:

$$\begin{aligned} Y_{k+1} &= V_{k+1} - H_{k+1}x_{k+1|k} \\ K_{k+1} &= P_{k+1|k}H_{k+1}^T(H_{k+1}P_{k+1|k}H_{k+1}^T + R)^{-1} \end{aligned} \quad (2.35)$$

Finally:

$$\begin{aligned} x_{k+1|k+1} &= x_{k+1|k} + K_{k+1}Y_{k+1} \\ P_{k+1|k+1} &= (I - K_{k+1}H_{k+1})P_{k+1|k} \end{aligned} \quad (2.36)$$

The updated estimates of Eq.2.36 will be used in the next step of the iteration as of Eq.2.34. The Kalman Gain K is, in the mono-dimensional sense, a value between 0 and 1 indicating what is more reliable, either the measurement or the prediction. Since normally the matrix R remains constant within the functioning range, it should approach zero as the system approaches a steady state, since $|K| < 1$.

The EKF in general is not an optimal estimator (it is optimal if the measurement and the state transition model are both linear). It heavily relies on correct modeling and initial conditions of the system: if these are wrong the filter may quickly diverge when the linearization point is too erratic. Another issue with the EKF is that the estimated covariance matrix tends to underestimate the true covariance matrix and needs external additive stabilizing noise to maintain meaning. De facto for battery the initial states of the model are known with good precision from prolonged tests, so it represents a good method of estimation.

2.5 DCDC CONVERTER AND CONTROL

The DCDC stage of conversion is the most energy dense component of the presented topology. It must allow unrestricted bidirectional charge of up to 50 kW, complete galvanic insulation between charging station and EV and low DC current ripple to be compliant with battery requirements. The high operating power of the application poses problems in the feasibility of the project, often the converter is composed by several smaller sized modules, allowing the usage of smaller magnetics and ripple reduction via interleaving techniques. The total load is then shared between modules either passively via independent voltage regulations on the same DC output node, or actively via control load sharing. The latter is more uncommon because it requires a specific feedback control structure to manage the current gradient between modules.

The chosen configuration is the Active Dual Isolated Bridge DCDC and is one of the most common in the EV charger industry and is shown in Figure 21. The transformer between primary and secondary bridge ensure isolation and if broad gap semiconductors are used, low magnetic losses can be achieved due to the high operating frequency, which of course requires careful sizing of the conductors [43]. The control scheme of the switches is the following: Bridge 1 operates as a Buck converter which inverts the voltage in a symmetrical modulated wave. S1.1 and S1.2 share the same duty cycle, while S1.3 and S1.4 operate with a time shift of $\frac{T_s}{2}$. The theoretical maximum duty cycle D' is 0.5 however, to prevent short circuit of the leg it is limited at a safety value below 0.5. Bridge 2 operates as Boost converter, S2.1 and S2.2 are switched on when S1.3 and S1.4 are switched off, same for S2.3 and S2.4 with S1.1 and S1.2. This sets the duty cycle of Bridge 2 (D'') to $1 - D'$. The characteristic waves for duty cycles, inductor current and output voltage are reported in Figure 22. Since the output waves are symmetrical at $\frac{T_s}{2}$, the average output voltage can be calculated on the half switching period considering $D = 2D'$, by considering steady state current ripple equal in the two parts of the semi switching period [44]:

$$\Delta I_L^+ = \frac{\frac{V_i}{n} - V_o}{L_1}\frac{DT_s}{2}; \Delta I_L^- = -\frac{V_0}{L_1}\frac{(1-D)T_s}{2}$$
$$\Delta I_L^+ = -\Delta I_L^- \rightarrow V_0 = 2\frac{V_i}{n}D' \tag{2.37}$$

Where ΔI_L^+ and ΔI_L^- are the current ripples during $\frac{T_s}{2}$, n is the winding ratio of the transformer and L_1 is the output inductance of the converter. The converter inductor current and corresponding duty cycles are shown in Figure 22 where the switching frequency of the PWM is $f_s = 20\ kHz$.

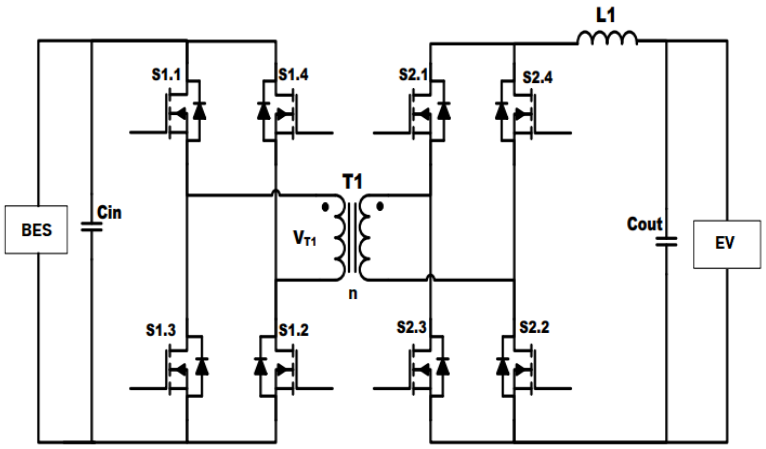

Figure 21 Dual Active Bridge Isolated DCDC converter topology

The transformer winding ratio n is chosen as *500/700* to level the input and output voltages to make sure that steady state duty cycles are near $D' = 0.2$, which is far from the operating limit of $D'_{max} = 0.5$. The inductance L_1 is chosen to have a value of $10\ mH$ to contain current ripple to 2%.

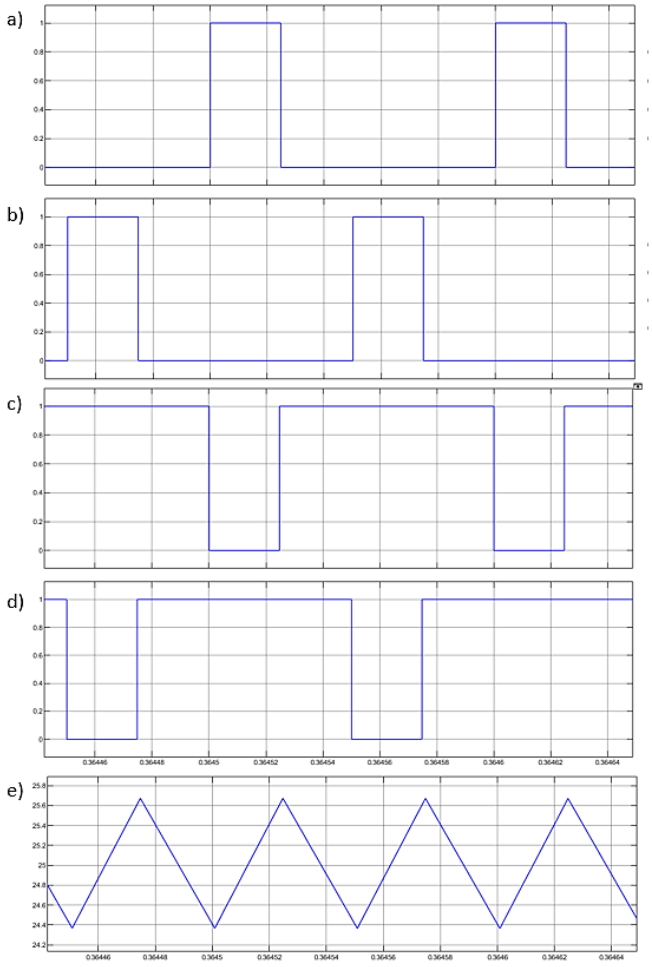

Figure 22 Duty cycle and Output Current Ripple [scales s and A]:
a) S1.1, S1.2 b) S1.3, S1.4 c) S2.1, S2.2 d) S2.3, S2.4 e) Inductor current ripple

Since the control scheme only relies on one duty cycle to generate the control waveforms of the switches a single control loop can be adopted. In this case, after the consideration made in 2.1, the control loop needs to impose the powering through the DCDC converter, which is identical to the current scaled by the EV's own battery. The control effort is calculated via the PI controller in Figure 23 which feeds the output to the dual PWM of Figure 24. The performances of the control scheme are shown in Figure 25, where the blue line is the current reference, and the red line is the inductor current.

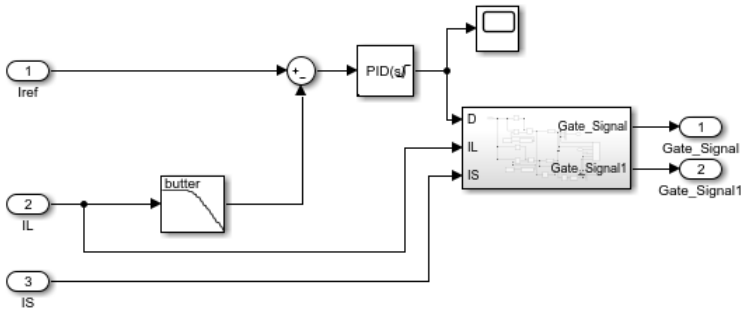

Figure 23 Inductor Current Control Loop; $K_p = 0.0005; K_i = 0.1$

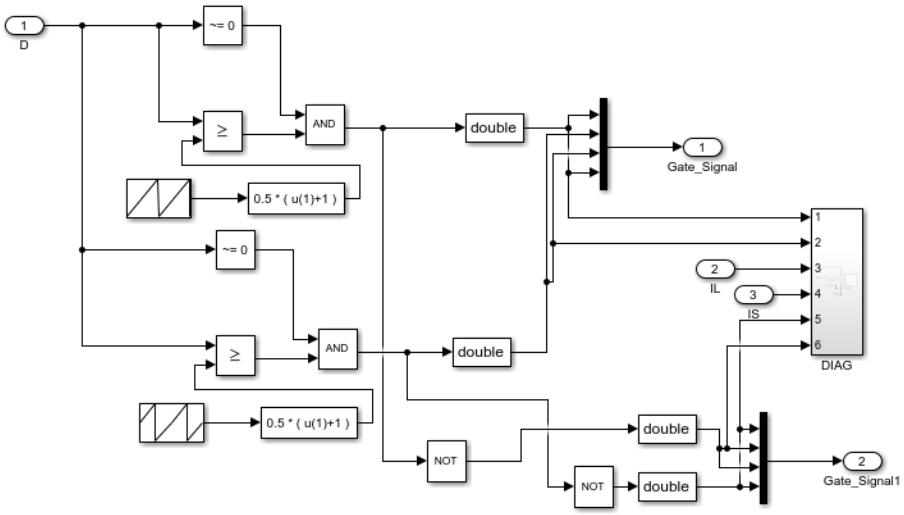

Figure 24 Dual PWM converter for Iso-DAB

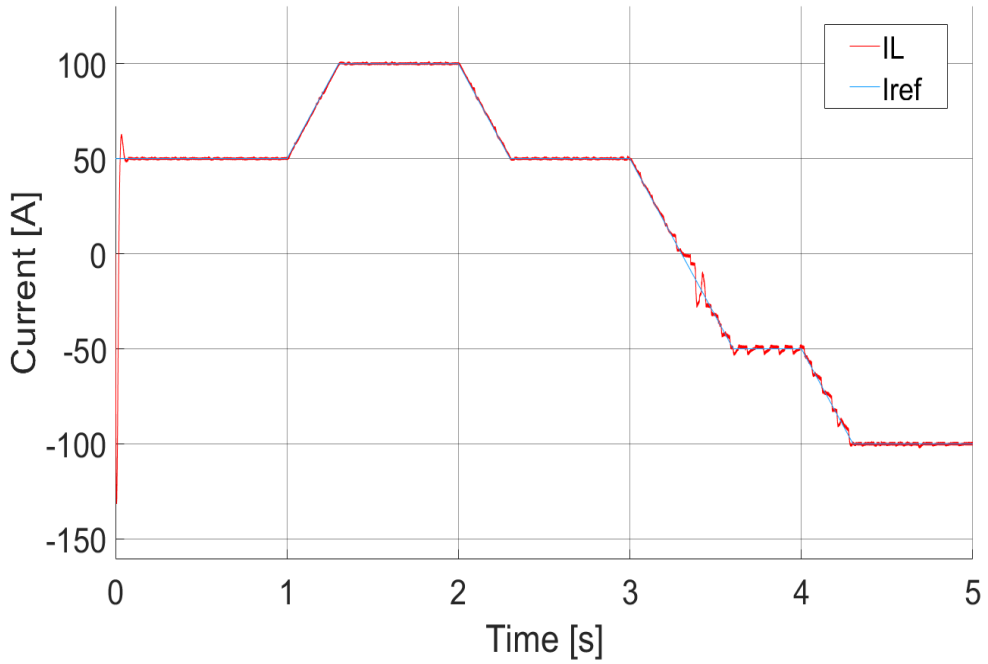

Figure 25 Inductor current on reference control performance with maximum slew rate 166 A/s

It can be noticed that the control scheme has problems crossing the 0 A axis due to the filter on the feedback loop. In this case a fixed lookup table for the duty cycle may be employed in the vicinities of the crossing to jump the system to a stable steady state, since the bandwidth of the chosen controller allows for faster dynamics. This effect will be shown on the prototype waveforms in the next chapter. The maximum slew rate is set to 166 A/s as set by the IEC 61851. The input current of the DAB is inverter by the first bridge, this causes a discontinuous current to be drawn from the embedded BES which is not ideal as shown in Figure 26.

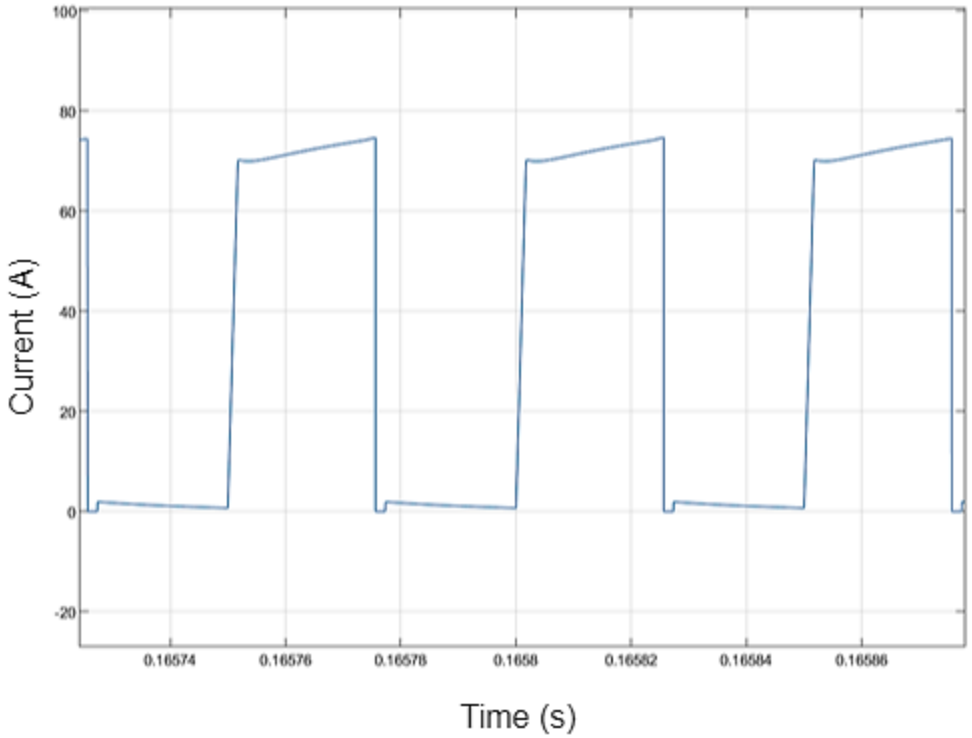

Figure 26 BES Input current with positive reference setpoint

In practice this is corrected by adding an additional boost stage at the input of the converter, which also extends the range of possible input voltages since there is another degree of freedom in the control.

2.6 SYSTEM SIMULATION AND EXPERIMENTAL FINDINGS

The system simulation is based on the ideal final product, however since the work is in prototypal stage some compromises will have to be accepted to provide proof of concept quickly. For example some of the firmware and software is offloaded to third parties to provide ease of integration and will therefore not be available for critical analysis. Some other implementations would simply require too much time and will be included in a later release of the application. The design of the AC components of the simulation is described in the later chapters 3 and 4. The employed AC control is current reference based dq control with digital PI regulators and active capacitor current damping. The switching frequency f_{sw} is set to $15\ kHz$ and synchronous sampling is used such that the sampling frequency $f_s = f_{sw}$.

The startup sequence of the ACDC AFE is shown in Figure 27 representing the 3-phase grid currents and in Figure 28 the voltage of the DC-Link, the first current peak corresponds to the DC Link pre-charge to grid rectified voltage of circa $564\ V$, the next current peak is imposed by the voltage regulator which regulates the DC-Link voltage to match the battery voltage as read by the BMS to prevent sudden in-rush of DC Current. After the two voltages are sufficiently close a DC contactor is closed. Just after second 0.35 in Figure 27 the ACDC AFE starts to draw 10 kW to recharge the embedded BES, Figure 29 shows the working THD achieved by the final simulation complete of switching dynamics. The low frequency harmonics are undamped due to the absence of low frequency active filters, however the THD is at an acceptable level. The maximum current peaks achieved in this way are of just above $40\ A$, which should be supported by commercially available breakers, the DC resistance used is rated $10\ \Omega$, $50\ A$. The startup process is completely regulated by MATLAB Stateflow software represented in Figure 30 which allows for fast deployment on the plant controller.

The main battery models have been descripted in 1, however not all parameters are available for simulation since a model too complex would not increase simulation precision, rate of convergence and experimental identification of the modules was not a viable route for fast prototyping of the charging station. Figure 31 shows the battery model employed and the SOC estimation algorithm which corresponds to CC previously described. The lookup table have been taken form the test parametrization shown in Figure 8 to Figure 12. Since the model is discretized via table, and the parameters have sharp changes the battery voltage during simulation might contain false discontinuities, these are to intend as averaged as per the real behavior of the battery.

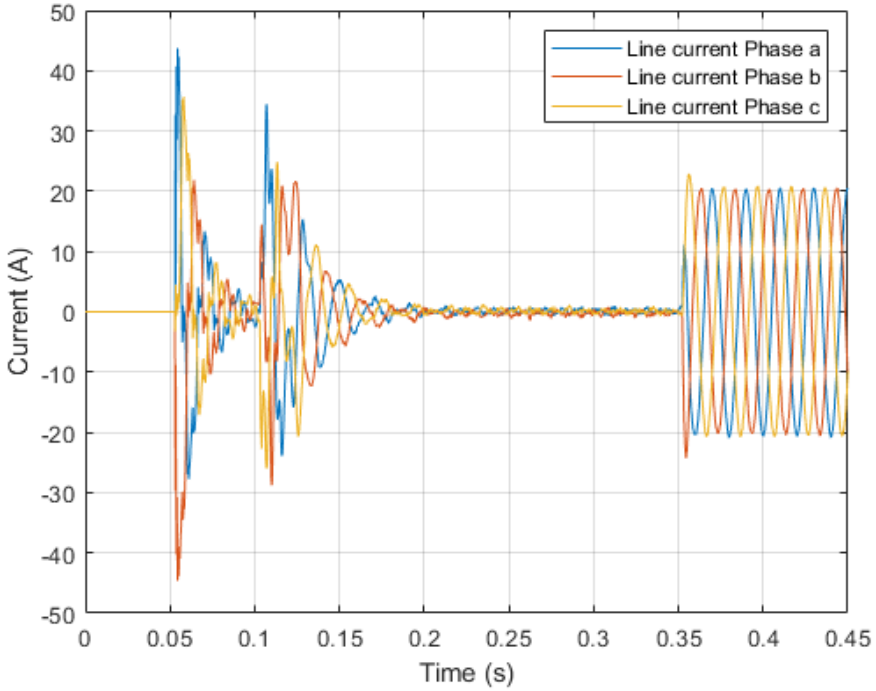

Figure 27 Grid currents profile during startup sequence

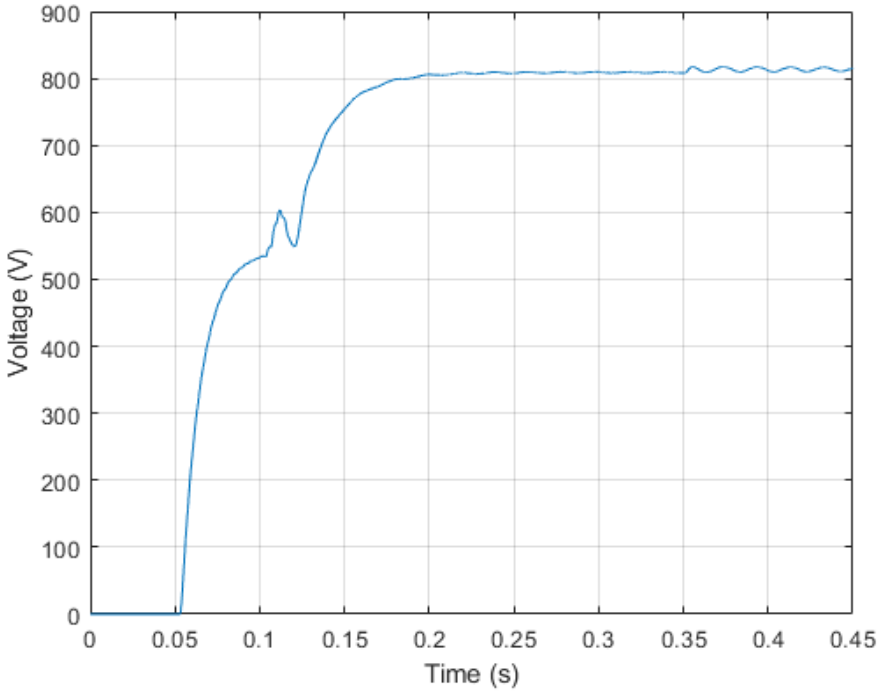

Figure 28 DC-Link voltage profile during startup sequence

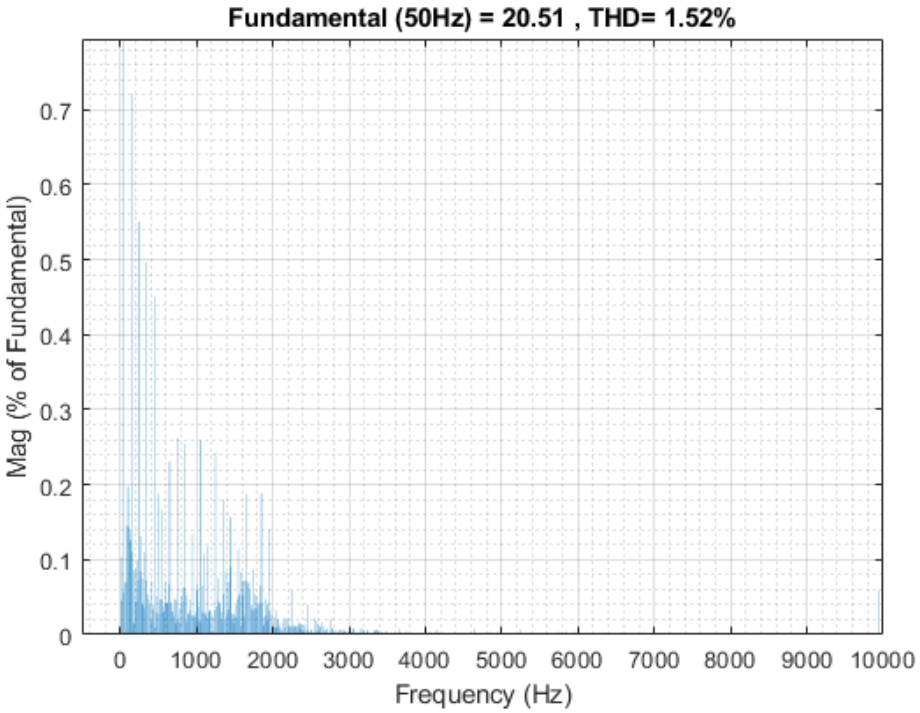

Figure 29 Total Harmonic Distortion (THD) of line currents after startup sequence

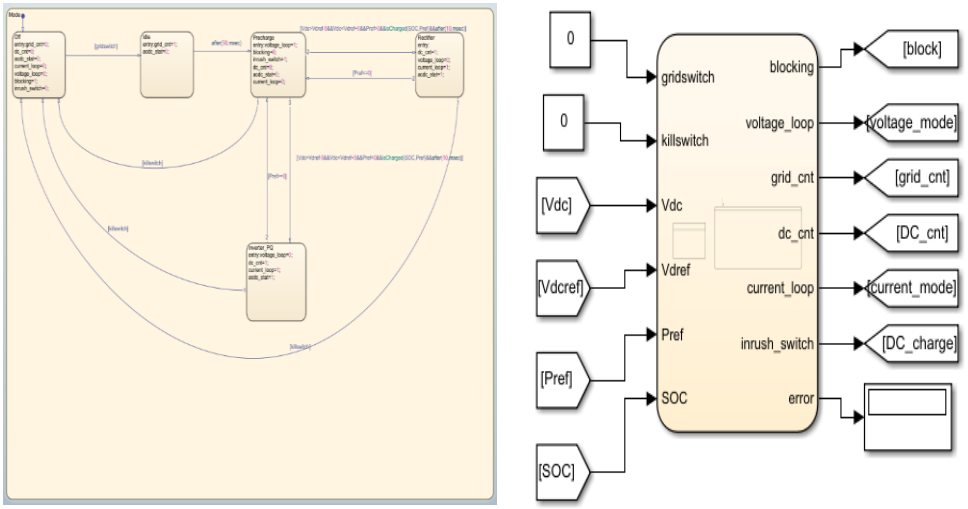

Figure 30 MATLAB Stateflow controller for model management

A simulation of recharge cycle was set to demonstrate the working rationale of the charging station. The initial SOC parameters of the EV battery and BES were set to 30% and 95% and capacities 42.2 kWh and 80 kWh of respectively, the increased size of the BES reflects cabinet optimization considerations in the prototype. The charging cycle was divided in 4 parts :

1. From minute 0 to minute 20 the EV is recharged at 50 kW from the BES, here no power is drawn form the grid. The smaller EV battery is recharged quickly to 70% with no gird impact.

2. From minute 20 to minute 30 the recharge power of $50\,kW$ is split between the BES ($40\,kW$) and the ACDC converter ($10\,kW$) in order to reduce power consumption from the BES, thus granting higher capacity for the next cycle.
3. From minute 30 to minute 45 the BES is set to draw $0\,kW$ as the EV approaches 90%, since a 40 mins recharge time was set and there was available power for the grid.
4. After 45 minutes the EV departs, and the BES slowly siphons energy from the grid to get ready for the next recharge cycle.

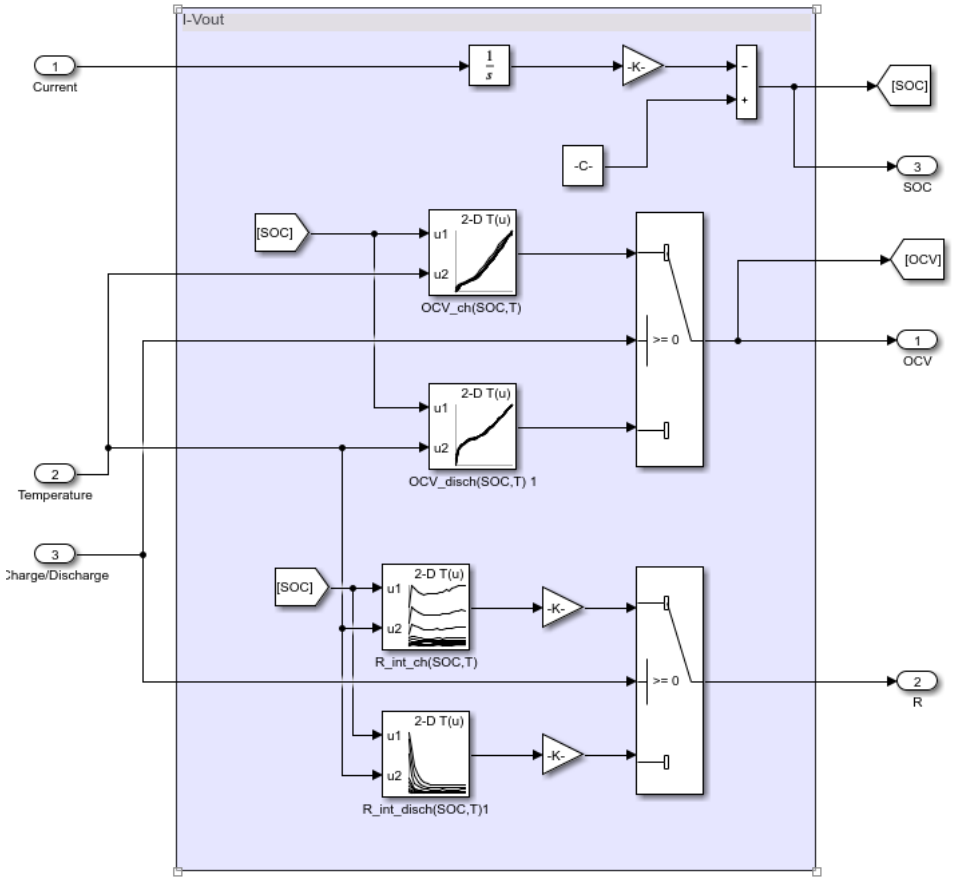

Figure 31 Simulation BES model with CC

Figure 32 and Figure 33 show the charging cycle described above as well as the SOC evolution during said cycle. Power is considered positive when absorbed from the grid and injected into the EV, while power absorbed from the BES by either the grid or the EV is considered negative. The calculated current references to feed into the converter controllers are shown in Figure 34, and can accurately be followed by the system. The DCDC converter does not present ripple because an average model was used to prevent simulation errors caused by long simulation times (above 70 minutes). It can be noticed that the current reference is updated on the basis of the EV voltage of Figure 35, since the power must be kept constant.

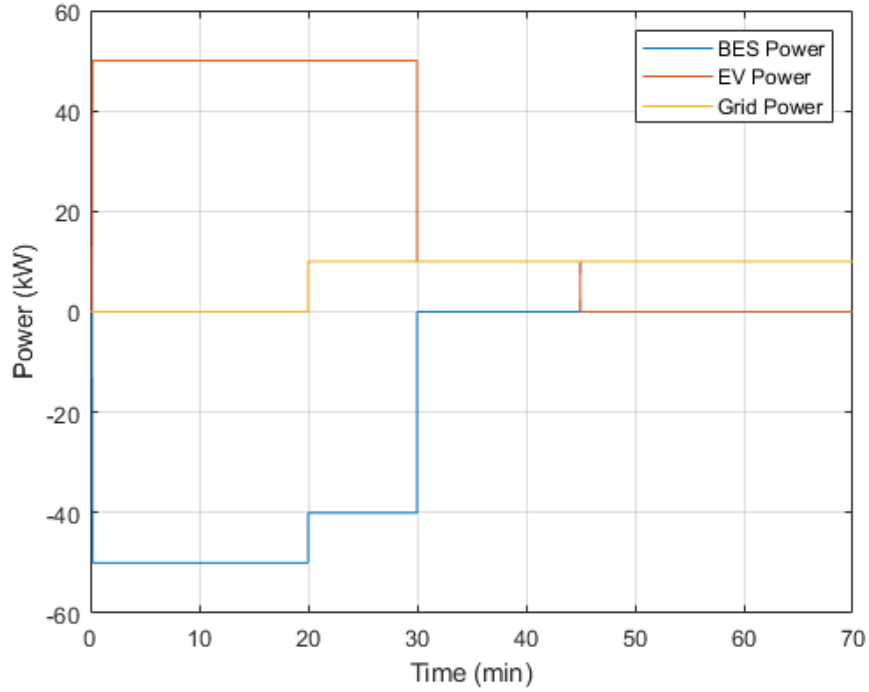

Figure 32 Typical charging cycle of an EV with fast charging from the embedded BES, Power Profile of the converters and BES

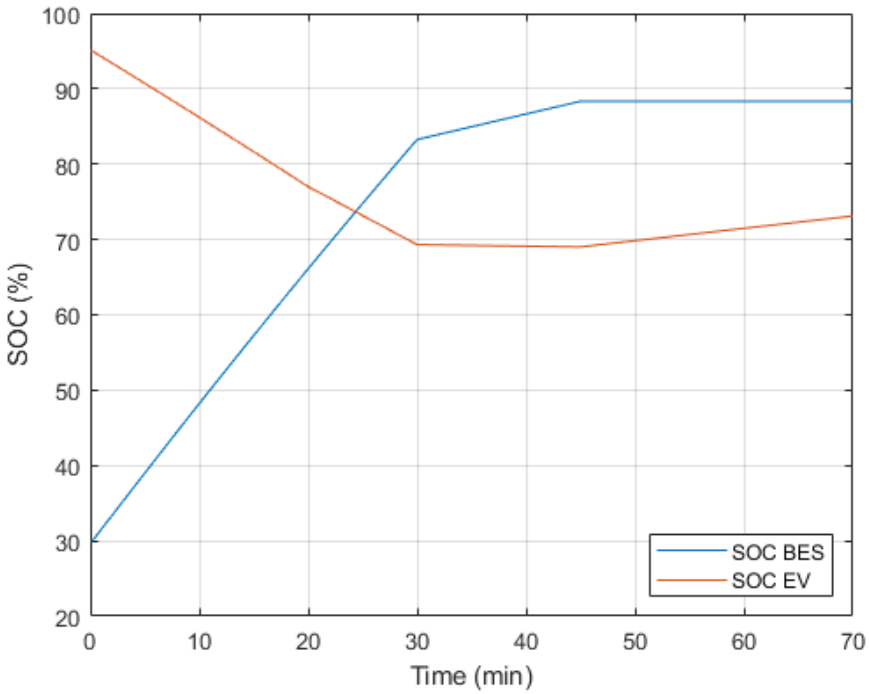

Figure 33 Typical charging cycle of an EV with fast charging from the embedded BES, SOC Profile of the batteries

The batteries voltage profile is shown in Figure 35, the curves are unusually sharp in some instants, this is caused by two superimposing effects: the sharp change in requested current changes the voltage drop on the batteries' ESR, which in turn changes based on the SOC level. The test cycle proves the point of fast charging via electric inertia, where one key consideration is the preservation of that inertia since the charging station must be able to operate continuously. In other words if there is available power to be drawn from the grid (based on grid frequency and voltage profile), the primary route is still moderate power absorption, however the

regulation effort can be employed when needed and even when no EV is available. The dynamic behavior ,with respect to the grid, of the system can then be assimilated to that of the ACDC converter, considering the DC link charged by the battery, in this instance the total design of the filter and converter must be considered. Final systemic results of are shown next.

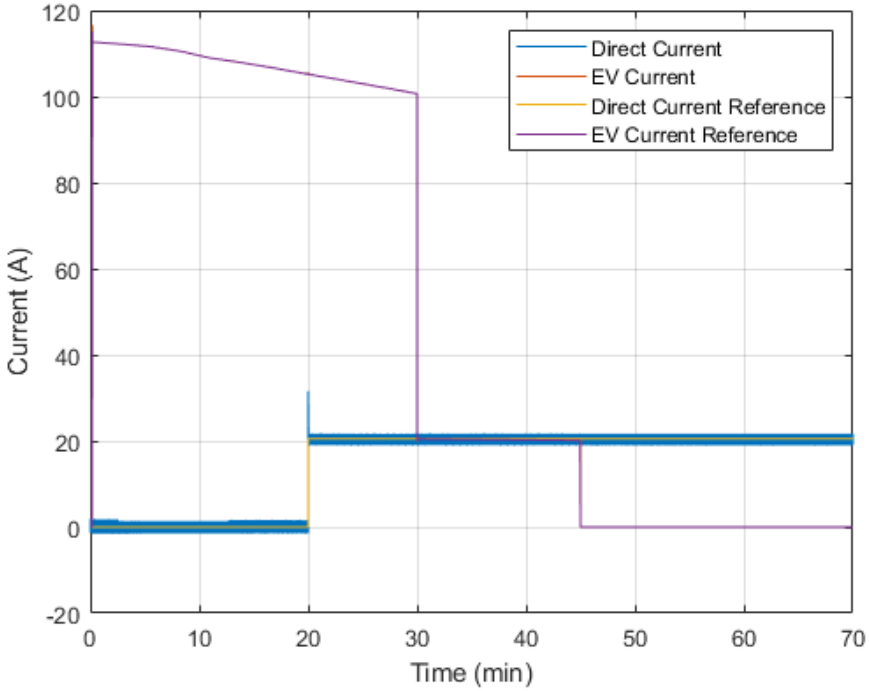

Figure 34 Calculated current references for the control of the charging cycle

The dynamic performance of the system can be evaluated by imagining a fast primary regulation request from the TSO, regarding V2G and stabilization operations. Here a setpoint of primary current were requested to the system every $0.1\ s$ and are shown in Figure 36 in the form of direct current where a maximum slew rate of $500\,\frac{A}{s}$ was applied. The converter is able to follow accurately the setpoint and is not limited by poor bandwidth, which is fundamental to ensure responsiveness in applications where grid services are required. The exact control strategy is explained in 4 and relies on the design of a low frequency LCL filter and active damping of the interaction between the low cutoff frequency of the filter and the high bandwidth of the controller. The converter side current are shown in Figure 37, and predictably are afflicted by high harmonic components, however Figure 38 shows the currents effectively flowing through the grid transformer which exhibit low THD, even if low frequency harmonics are still present, as they are too low frequency to be attenuated by the LCL filter without compromising the control. Finally, Figure 39 shows the typical current contribution of the filter capacitor to the currents. These are high in harmonic content; however they also contain a first order harmonic due to the $50\ Hz$ impedance of the capacitor. It should be noted that aside for some non-idealities in the capacitor only reactive power is drawn.

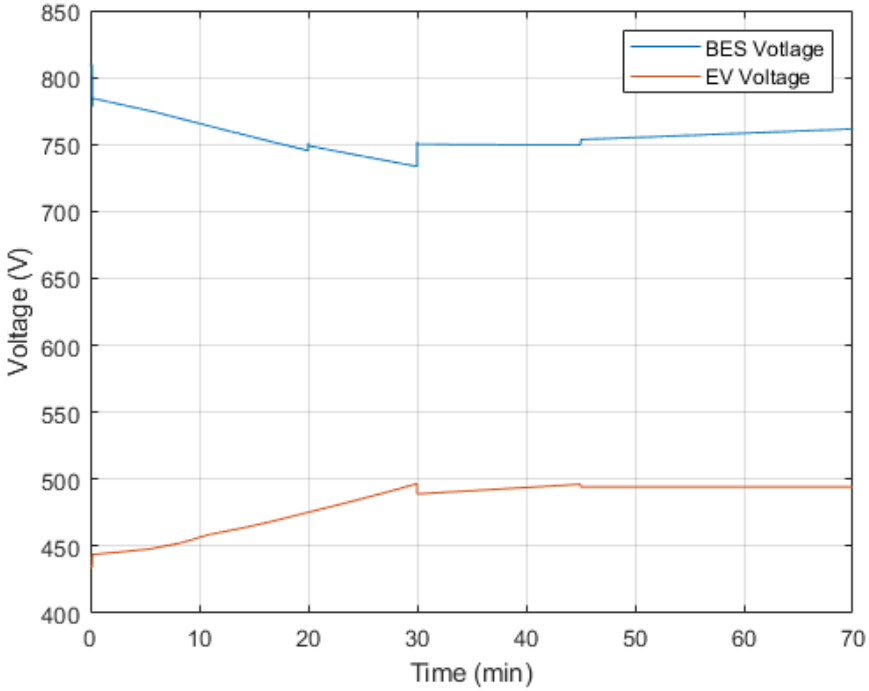

Figure 35 BES and EV battery voltage profile during the cycle

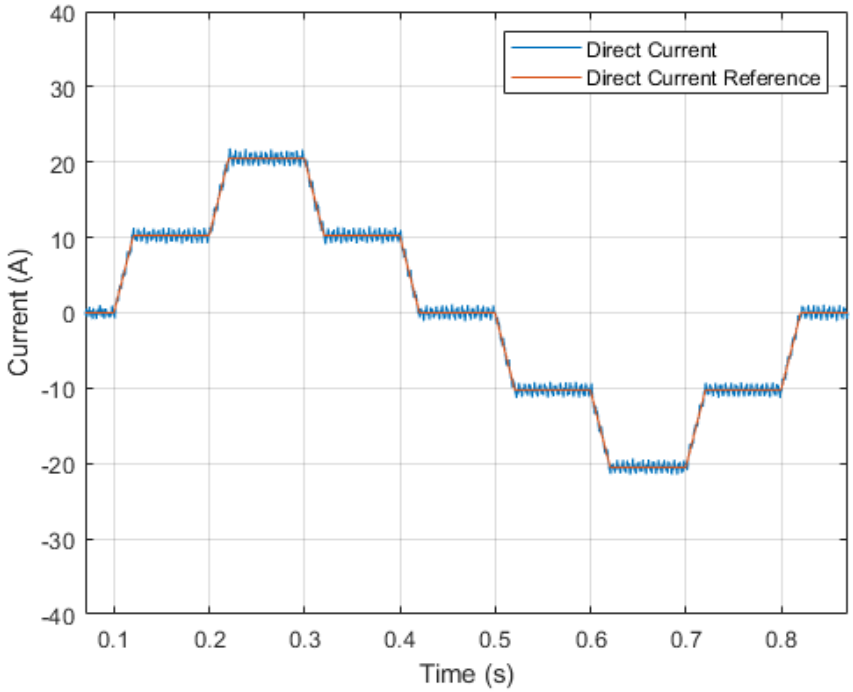

Figure 36 Current references for simulated primary control, with maximum slew rate of 500 A/s

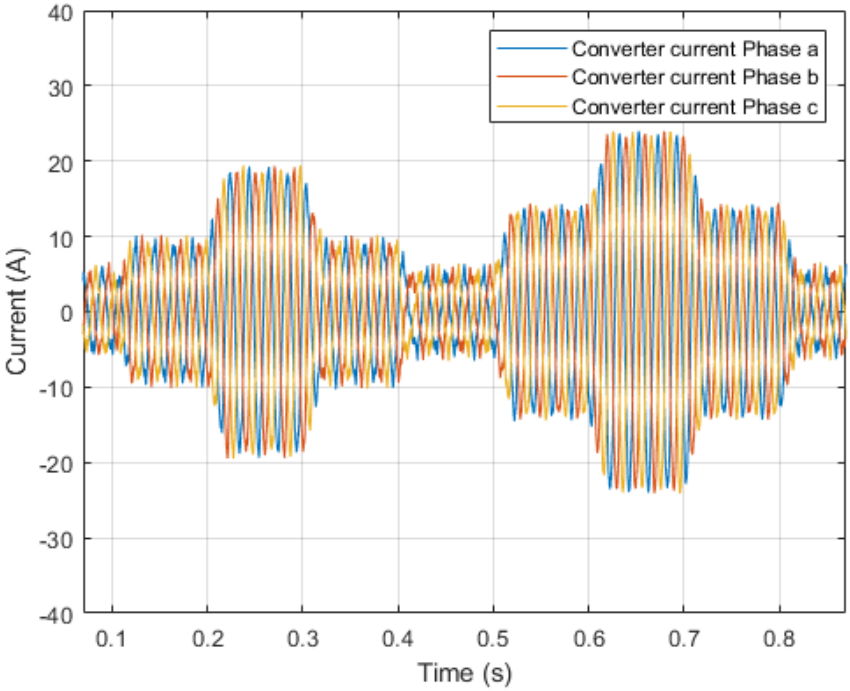

Figure 37 Converter line current during fast primary regulation

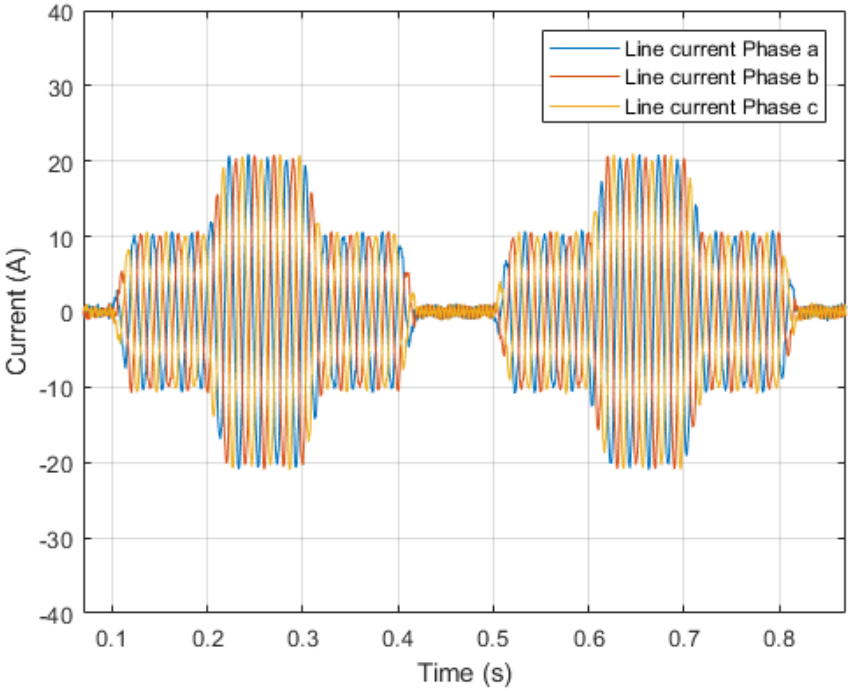

Figure 38 Grid line current during fast primary regulation

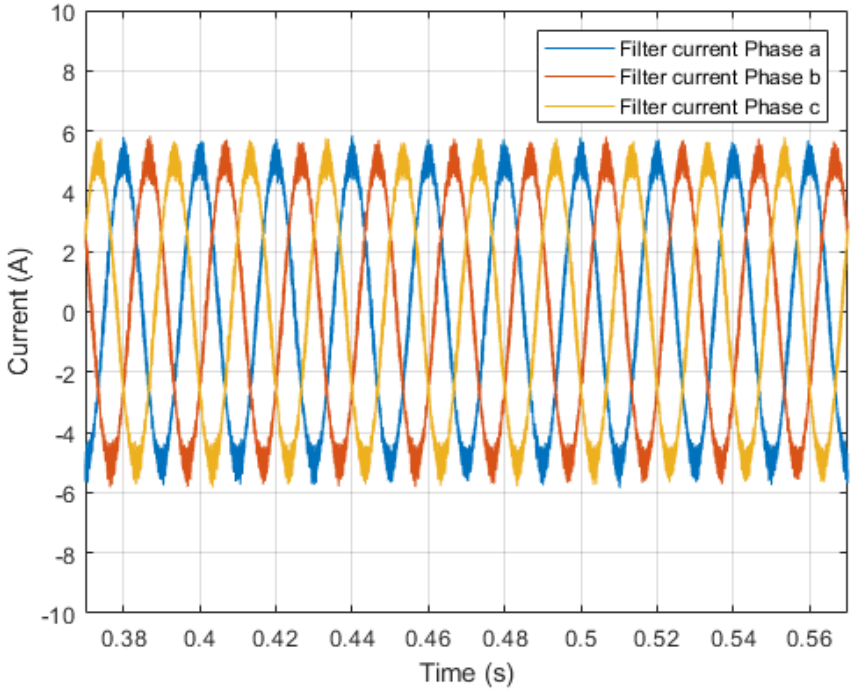

Figure 39 Filter capacitor line current during operation

2.6.1 Experimental Setup and Findings

In this section the experimental measurements based on the physical prototype will be reported, however in this stage of the project the prototype was not yet completed so the differences in architecture must be noticed. As shown in Figure 40 the Embedded BES was not connected in the prototypal due to delays with the external BMS supplier, however the power converter could be validated using the AFE ACDC as an equivalent voltage source (e.g. using a voltage reference-based control loop) as per 4.1.2, as a consequences the step of the ACDC q-d current cannot be measured directly, however the HV DC current is still controllable by the DCDC converter.

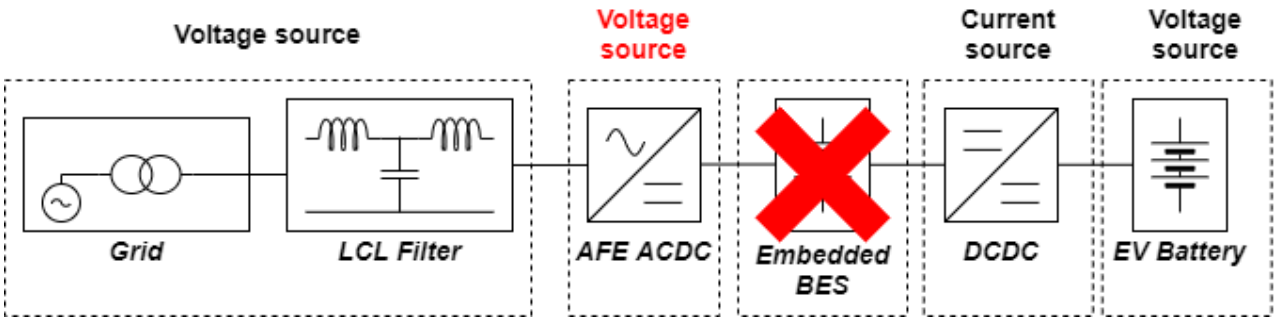

Figure 40 Difference between finished scheme and current state of the prototype with equivalent controlled behavior

The experimental setup is shown in Figure 41, the list of instruments that have been used are:

- Isolated ACDC Power Supply 15kW 1500V-30A (Test Benchmark)
- AFE 10kW with filter
- 100kVA Transformer
- Cabinet 50kW DCDC

- ACDC 10kW (Grid circulation)
- EV Battery
- Oscilloscope 4 channels (RS-485)
- Multimeter (Fluke MT13)
- CAN-USB converter
- PC

The test was divided in 2 phases, the first validation of the DCDC cabinet via a benchmark run with grid circulation of power and the second one with the actual EV battery.

Figure 41 Experimental setup

The steady state operations can be observed in Figure 42, the output EV Battery voltage is variable due to the ripple in current creating voltage drops in the ESR of the battery cells. A magnified view of the ripples is offered in Figure 43, the input DCDC current ripples at a

frequency of 45 kHz because a boost stage has been inserted to prevent the behavior presented in Figure 26, the output DCDC current (to the EV) instead has a ripple of 100 kHz since that is the chosen operating frequency of the Dual Active Bridge. The step in current reference performances are shown in Figure 44, where can be noticed that a 25 A step takes 114 ms to actuate which roughly corresponds to 220 A/s which is more than satisfactory.

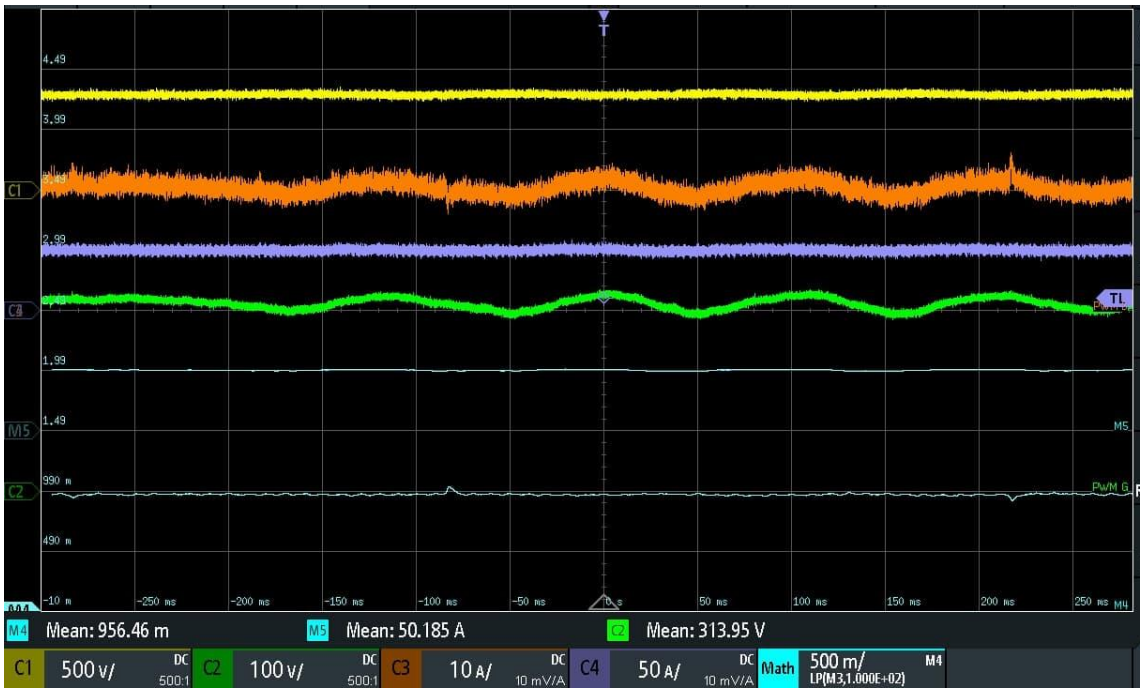

Figure 42 Steady state operation of the system at 800 V DC Link voltage (Yellow), 400 V EV Battery (Green), Input DCDC current (Orange) and output (Purple) at mean running efficiency of 96%.

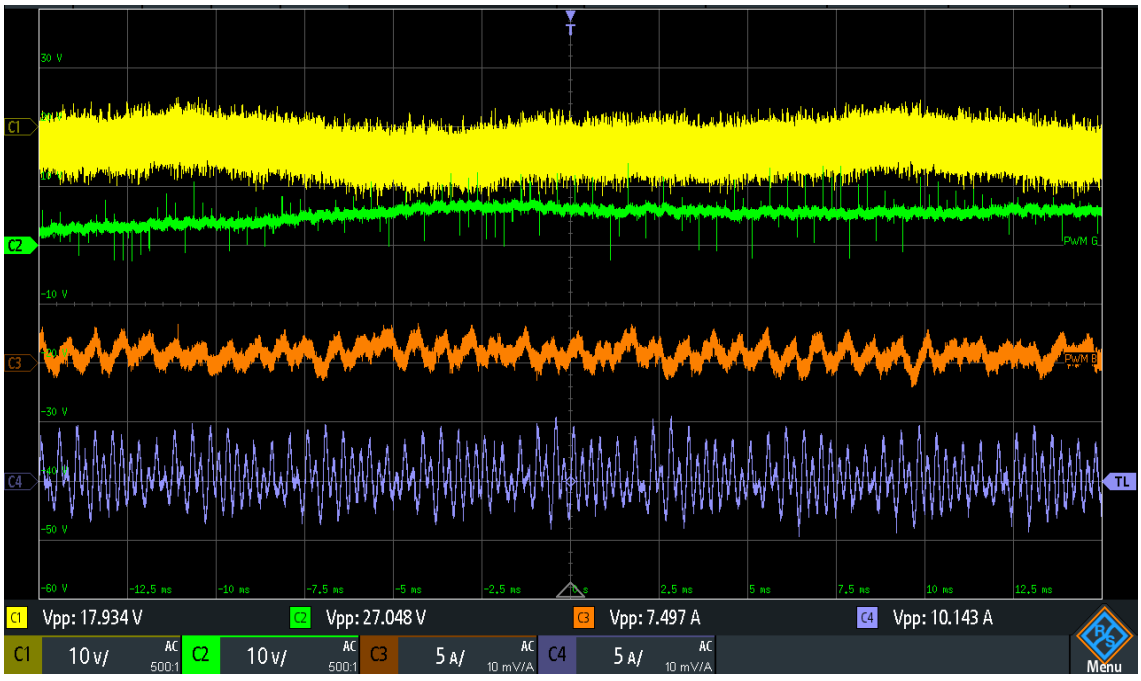

Figure 43 Ripple of the measures in Figure 42.

The digital delay inside the DCDC converter is hard to measure given the internal speed of the processor (which must be above 100 kHz) however, in Figure 45 the delay of the current reference setpoint, which is external has been taken as a measure to evaluate the digital response

of the converter. From 0 A average to 10% of the final step value the reference delay is in the order of 5 to 10 ms, which is many machine cycles and so cannot impact internal operations.

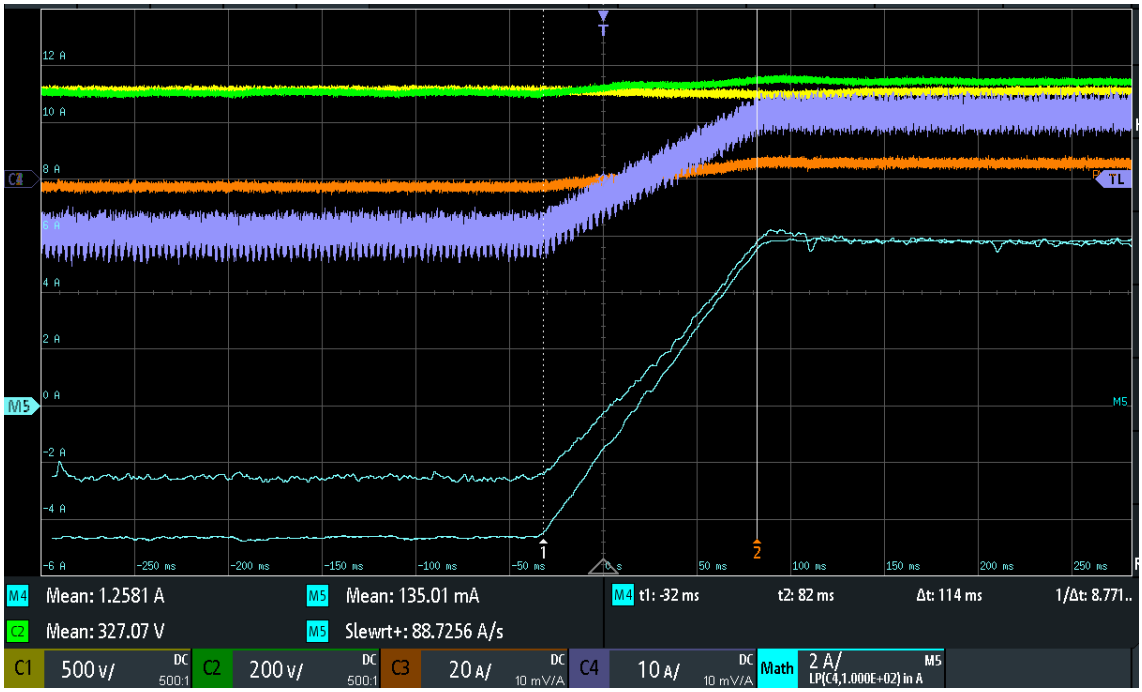

Figure 44 Current step performances on the DCDC under limiting current slew rate, where the light blue lines represent the averages of the input and output currents.

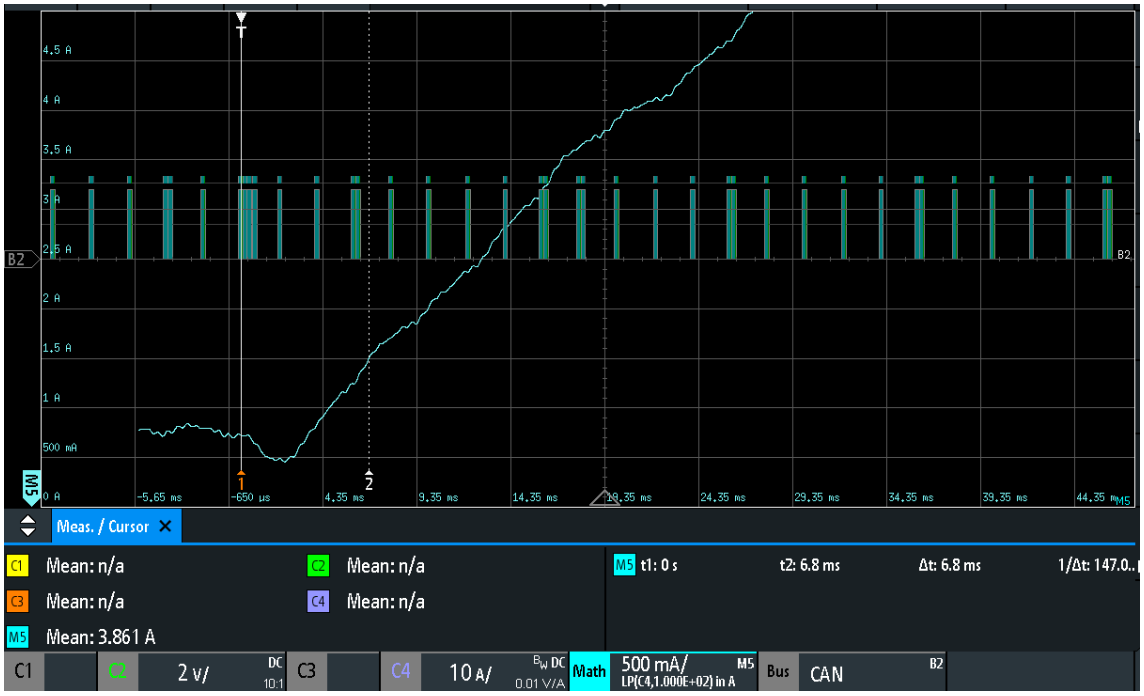

Figure 45 Digital delay on current reference of the DCDC converter

The AC grid currents are reported Figure 46 at the operating power of 10kW, the measure is affected from low sampling time which partially explains the high THD, however the second reason is the AC EMI ground filters (C_y) had to be removed in order to add DC ground filters to contain common mode voltages that might go outside the operating range of the DCDC converter.

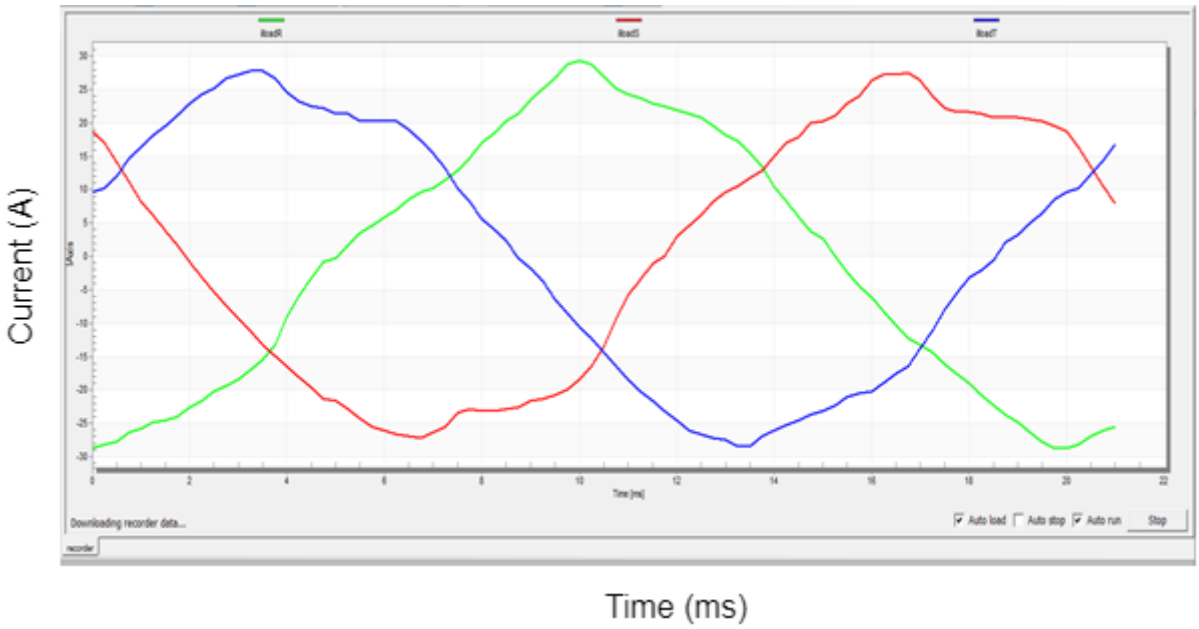

Figure 46 AC grid currents on the AFE ACDC converter

3 AC/DC CONVERSION

The initial stage of the fast charger is the conversion from the 50 Hz 400 V mains to the DC voltage of the off-board battery. As already mentioned, the voltage of the DC-link needs to be elevated with respect to the EV battery to allow for easier control schemes. This poses a problem with respect to the maximum output withstand able voltage of the rectifier which also needs to be high. The main solution to this problem in the past has been the use of clamped multilevel converters, which have the advantage of reducing the stress per switch, but on the horizon of AC/DC conversion technology an alternative method of resolving the problem is gaining foot: the widegap Silicon-Carbide (SiC) switch. The usage and integration of these two technologies will be analyzed next, and a quick survey will reveal the most common adopted solutions. After the converter topology has been established the focus will change to the control method for this specific application, which will require the derivation of a mathematical model to analyze low frequency behavior. Finally, the discrete active damping application will be introduced, with a focus on the role of sampling time and delay in calculation. An algorithm will be proposed in order to ensure stable performance even with different connections to the grid, basically proving the impact of the MV/LV transformer on the discrete control.

3.1 CONVERTER TOPOLOGIES

3.1.1 2-Level Converters

At its most basic, a three-phase AC/DC converter is composed of a an half bridge configuration mounted on each one of the AC-phase like shown in Figure 47, this is commonly denominated "2-Level": the switching table in Table 7 represents the voltage seen from the AC-network nodes $j = A, B, C$ with respect to a common point N, depending on the position of the switches. Switches on the same leg are driven from logically negated signal so that short circuits are avoided. Via a simple KVL, the voltage stress that needs to be endured by each switch, when $V_{jn} = \pm V_{dc}$ is $-V_{jn}$ which is the entire voltage of the DC-side. The use of a 2-Level converter in this application might be challenging due to the BES voltage specifications (Table 5) of more than 800 V; moreover since the rated power of the converter is 11 kW also the current rating of Eq.3.1 must be met:

$$I_n = \frac{P_n}{V_{min,battery}} = 20\ A \tag{3.1}$$

The choice of adding many switches in parallel, to increase the current rating is possible but, staying on the low side of switches per leg benefits both reliability and control effort, since the gate signals will be traveling at switching frequency and will be subject to radiated emissions problems, and will have production processes unbalances. For an 800 V converter of this power, the use of a 2-Level configuration is possible, but to scale the design other solutions will be considered next.

Table 7 Switching table for 2-Level Inverter

Voltage Level (Vjn)	M1, M3, M5	M2, M4, M6
Vdc	1	0
0	0	0
-Vdc	0	1

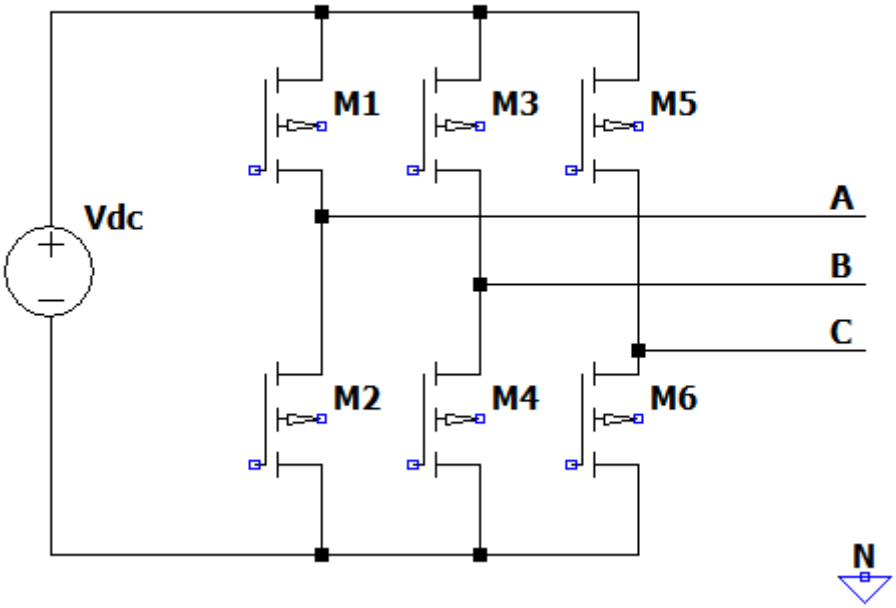

Figure 47 Three Phase 2-Level Inverter

3.1.2 Multilevel Converters

The accepted engineering solution to reduce the problems of a 2-Level converter is to increase the number of DC voltage levels at which the converter can operate, hence the name "Multilevel". The advantages of this kind of configurations are not only restricted to higher nominal values, but extend to better functionalities inside the operating range such as [45]:

- **Staircase waveform quality:** The higher number of DC steps increases the fidelity of the output AC waveform to the mains waveform, when the converter is working as an inverter, however it does not provide extensive advantages when the converter is working as a rectifier.

- **Lower switching losses:** Switching losses are deeply affected by the voltage blocked by each switch, less blocked voltage means either higher switching frequencies or more current, solving partially the power for higher power converters.

- **Better electromagnetic compatibility:** The so called $\frac{dv}{dt}$ is highly reduced by the presence of more levels given the same switching frequency and the same switching time of the transistors, reducing higher frequency wave pollution.

The are several macro-types of multilevel converters, briefly visualized in Figure 48. The Cascaded configuration among Separate DC sources is only used in very high voltage

applications and will not be analyzed in this instance. The Common DC Source configurations are more used for the application considered and each have set of advantages and disadvantages.

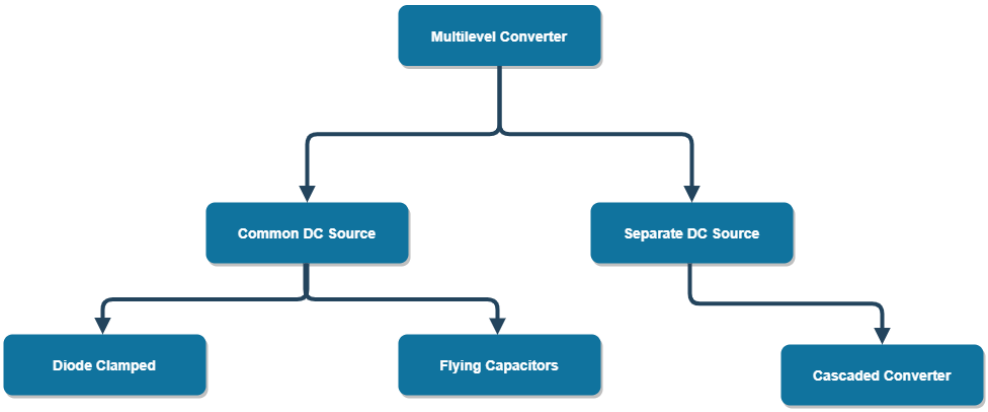

Figure 48 Multilevel Configurations

The Diode Clamped configuration, in its 3-Level variant, is reported in Figure 49 Both the high-side and low-side of each leg require 2 switches which are clamped to the midpoint of the DC voltage via a diode. Said voltage midpoint is created using a capacitor only branch, from + to – of the DC part. Reported configuration, in according with Table 8 and following the same considerations made for the 2-Level configuration, allows each switch to block only half of the DC bus voltage, effectively doubling the rating of the converter in voltage terms.

Table 8 Switching Table for 3-Level Clamped Diode

Voltage Level (Vjn)	**M1, M3, M5**	**M2, M4, M6**	**M7, M9, M11**	**M8, M10, M12**
Vdc/2	1	1	0	0
0	0	1	1	0
-Vdc/2	0	0	1	1

One significant disadvantage of the configuration shown in Figure 49 is the high part count, decreasing both reliability and cost efficiency. The number of components needed by an m-Level diode clamped converter is:

- $2m - 2$ number of switches
- $m - 1$ DC decoupling capacitors
- $(m - 1)(m - 2)$ diodes

The number of diodes evolves quadratically with the number of levels, posing costs and sizing problems. The diodes also need to be high speed and suffer from reverse recovery stress, making heat dissipation troublesome. The flying capacitor configuration partially solves these issues, replacing the clamps with voltage levels provided by capacitors connected between switches, however these capacitors need to be charged in the starting sequence, with carefully designed control to achieve balance between capacitors. These configurations are state of the art where AC forming is needed, but for DC recharging the size and number of components make them undesirable.

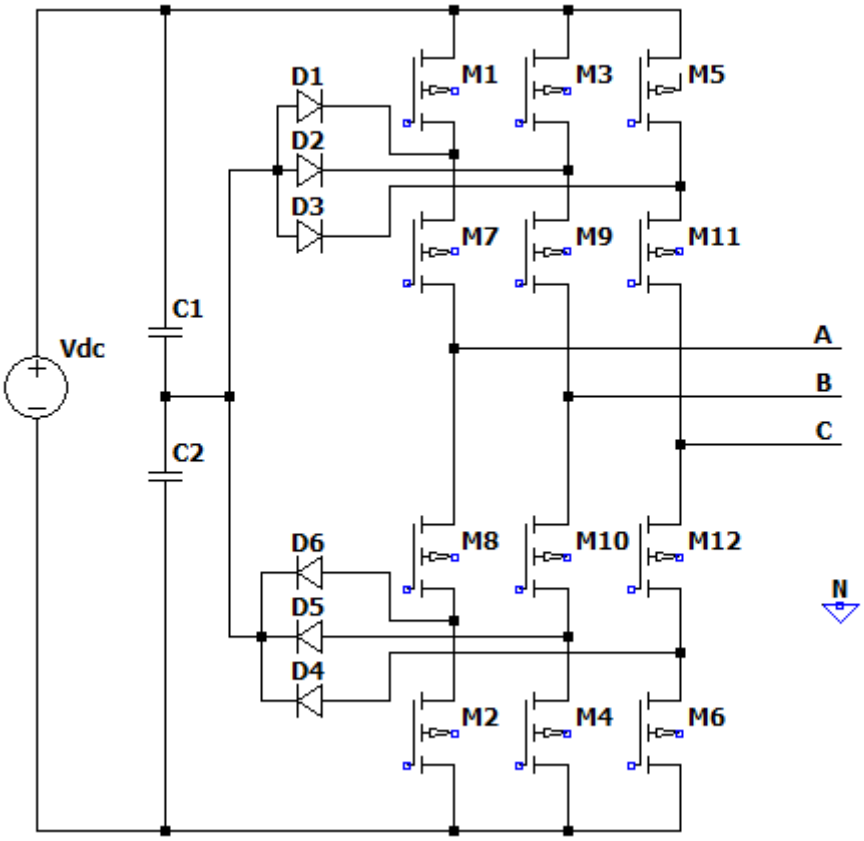

Figure 49 3-Level Clamped Diode configurations

3.1.3 SiC Converters

Silicon Carbide (SiC) switches are the frontier of switching devices. The new chemistry (as opposed to the old Si-based) grants higher blocking voltage per epitaxial layer, greatly diminishing the size of the switch. The reduced size of the switch brings about many improvements, such as the reduction of parasitic capacitance between pins, granting less storage energy and higher achievable switching frequencies. Of course, the thinner epi layer also grants reduced conduction resistance (R_{on}) thanks to the higher concentration of carriers that can be obtained, however more complex driving circuits are needed to provide enough charge to the switching devices in the decreased switching time window.

For example, Sic Mosfets suffer from very low undervoltage lockout (UVLO), so the need to ensure the appropriate voltage is needed, complicating the driving circuit or face the possibility of a thermal runaway due to the increase of R_{on}[4]. Table 9 presents a comparison between two top of the line switches, which compete for the same market, tipping the balance in favor of the new chemistry.

[4] The gate voltage (V_{gs}) is directly responsible for the distribution of active carriers in the epi layer, lower density of carriers results in a decreased E-field propagation which cause higher conduction resistance.

Table 9 Comparison between a SiC Mosfet and a Si Power Mosfet

Parameter	SiC Mosfet	Si Power Mosfet
Vds [V]	1200	1050
Id [A]	50	46
Tj-max [°C]	175	175 degraded 150
Rds [mΩ]	45	120
Ton or Toff [ns]	20	100
Cgs [pF]	65	50
Cdg [pF]	16	158
Switching losses [mJ]	0.350	1.6

To summarize the advantages of the SiC are:

1. Lower conduction losses
2. Higher Voltage Rating
3. Better switching properties

While the disadvantages are:

1. More complex driver circuit
2. More expensive

The higher voltage rating seems to solve the 2-Level configuration drawback, and the increased complexity of a m-Level converter is not justified, even if would provide better THD on-line voltages, so a 2-Level configuration with SiC devices is chosen for this application.

3.2 LCL FILTER DESIGN

As mentioned, the total current distortion (THD) of line current must be kept under a certain value, the EU accepted standard is <5%. The ACDC converter is a known source of distortion due to the switching dynamics of the components and due to the PWM modulation of the gate signals. Classic PWM strategy is represented in Figure 50 for a 2-Level three phase converter: Figure 50.a shows the three phase sinusoidal signals $v_{c_{A,B,C}}(t)$, of amplitude v_c and frequency f_1, compared with the carrier triangular signal $v_t(t)$, of amplitude v_t and frequency f_s. The switching scheme is described in Eq3.2:

$$high\ side\ switch\ status\ of\ phase\ j\ = \begin{cases} 1; v_{c_j}(t) \geq v_t(t) \\ -1;\ v_{c_j}(t) < v_t(t) \end{cases} for\ j = A, B, C \qquad (3.2)$$

Combining Figure 50.a with Eq.3.2 for phase A yields Figure 50.b which provides the on-time and gate signal for M1 with reference to Figure 47.

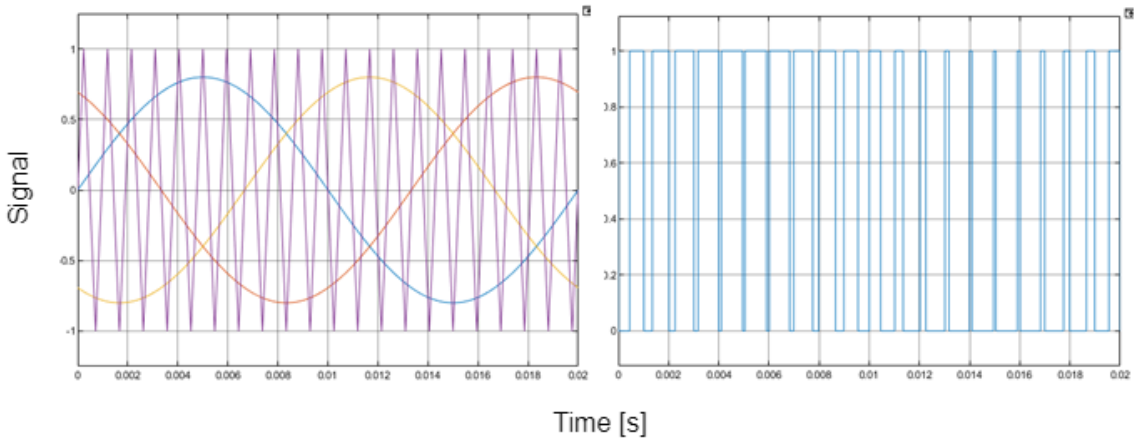

Figure 50
a) PWM control waveform with ma=0.8 and mf=21 b) Gate signal for high side phase A switch

For a three-phase active rectifier; the amplitude modulation index m_a and the frequency modulation index m_f can be defined as in Eq.3.3-4. Using the well know PWM relationship for a bridge converter in Eq.3.5, the value of the DC bus can be set; where V_{jn1} is the value of the first harmonic of phase j (220 V) applied to the converter and V_{dc} is the rectified voltage. Notice the condition $m_a < 1$ is often satisfied as the lower possible battery voltage value is usually greater than two times the peak value of V_{jn1}.

$$m_a = \frac{v_c}{v_t} \tag{3.3}$$

$$m_f = \frac{f_s}{f_1} \tag{3.4}$$

$$2\sqrt{2}V_{jn1} = m_a V_{dc} \rightarrow V_{dc} = \frac{2\sqrt{2}V_{jn1}}{m_a} \text{ when } \mathrm{m_a} < 1 \tag{3.5}$$

However, the rectified equivalent AC voltage $u_c(t)$ contains other harmonics due to the PWM switching pattern. The harmonics are centered around multiples of the triangular carrier frequency, which is now bound to the mains $f_s = m_f f_1$ and can be expressed via a Fourier series expansion, for the k −th harmonic order, as [46]:

$$u_c(t) = u_{c(1)} + \sum_{-\infty\ \mathrm{k}}^{+\infty} u_{c(k)} = \frac{m_a V_{dc}}{2}\sin(2\pi \mathrm{f}_1 t) + \frac{4}{\pi}\frac{V_{dc}}{2}\sum_{j=1}^{\infty}\frac{1}{j}\sum_{-\infty\ \mathrm{k}}^{+\infty} J_k(\pi m_a)\sin\left[(j+k)\frac{\pi}{2}\right]\sin\left[\left(jm_f + k\right)2\pi f_1 t\right] \tag{3.6}$$

Where J_k is the Bessel function of the first type of order k. The actual harmonic order is $h = jm_f + k$, as can be noticed by the last term of Eq.3.6. It can also be noticed that the existence of the harmonic is dependent on $\sin\left[(j+k)\frac{\pi}{2}\right]$, which means that the quantity $j + k$ must be odd for harmonic h to exist. By selecting m_f odd the existence of only odd harmonics can be ensured since, when j is even, k is odd and $jm_f + k$ is odd, when j is odd, k is even and $jm_f + k$ is odd. This grants more regularity to the wave. The harmonics are centered around $jm_f 2\pi f_1$ which means that higher frequency modulation index results in higher order harmonics. Higher

switching frequencies are preferred since they can be attenuated with filters that do not interact with the low frequency behavior of the converter, thus higher m_f is preferred, if the switching losses allow it.

The above-mentioned harmonic component of the converter AC voltage $u_c(t)$ injects current harmonics into the network as represented by Figure 51, which takes into consideration the single-phase equivalent of the circuit, recognizing the symmetry in Figure 50. The amplitude of h-th current harmonic is calculated in Eq.3.7, where V_h is the corresponding voltage harmonic.

$$I_h = \frac{V_h}{\sqrt{R_t^2 + [2\pi h f_1 L_t]^2}} \tag{3.7}$$

The transformer inductance naturally decreases the amplitude of higher order current harmonics, however additional filtering is usually required, especially when low power converters are considered, since the maximum ripple allowable depends on the minimum operating current. The simplest form of filtering requires the addition of and inductor, which works in the same fashion as the transformer leakage inductance.

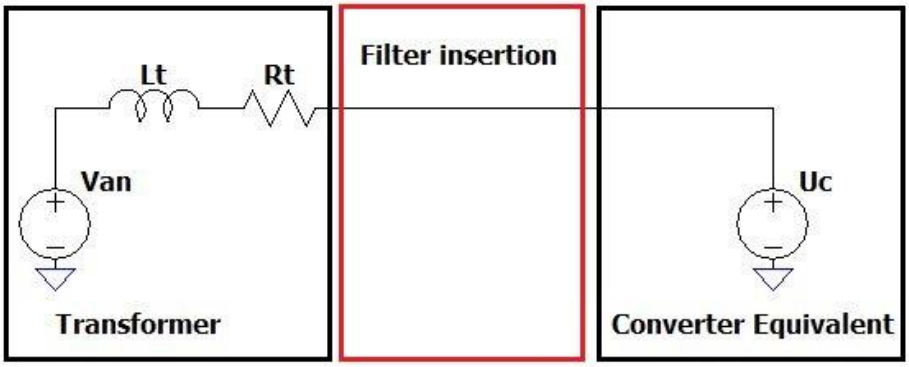

Figure 51 Equivalent AC circuit

The design is centered on two focal points: the reduction of the switching ripple as seen by the network and dynamic behavior of the filter. The first issue can be considered by setting both the maximum current ripple allowable ($\frac{\Delta I_L}{I_{min}}$), where I_{min} is the minimum drawn current on the first harmonic, and maximum duty cycle of the transistors δ, which is usually 0.75-0.9 [47]. Then the inner filter inductance L_i can be sized with reference to Figure 51 where an inductor in the red section has been added:

$$L_i = \frac{\delta U_{c\_max}}{\left(\frac{\Delta I_L}{I_{min}}\right) I_{min} m_f f_1} = \frac{\frac{\delta V_{dc\_max}}{2}}{\left(\frac{\Delta I_L}{I_{min}}\right) I_{min} m_f f_1} \tag{3.8}$$

This condition is usually hard to satisfy in terms of inductance: any sensible value of current ripple requires either very high switching frequency or very high inductance. For example considering the values of Table 3 and Table 5, setting $\left(\frac{\Delta I_L}{I_{min}}\right) = 0.20$, $I_{min} = 3\ A \rightarrow P_m = 2kW$,

$m_f = 201$ and $\delta = 0.9$, Eq2.8 yields $L_i = 6\,mH$ which must be rated for maximum power output ($I_n = 22\,A$) which sizing into a compact solution for low power might pose challenges.

The other design issue can be considered by specifying the frequency at which the pole of the $\frac{I_h}{V_h}$ transfer function should occur: for control reasons that will become clear later, the current dynamics should be faster than the voltage output dynamics, but losses in the inductor also need to be minimized. In general, the quality factor of the inductor Q_L should be in the range of 5 to 10.

To solve the issue of low attenuation, an additional capacitor grid-side can be added (Figure 52.a), however the resonant frequency of this solution needs to be decisively below switching frequency, which makes for high value of inductance and capacitance, moreover it is also a function of grid inductance, and so it may be unpredictable and degrade upon installation[5].

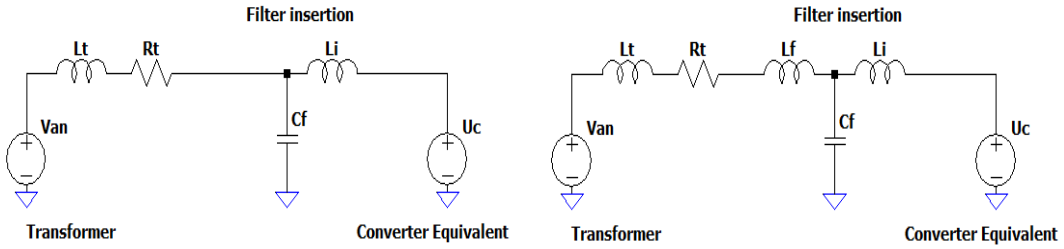

Figure 52

a) 2nd order filter *b) 3rd order filter*

The final iteration of the input filter is shown in Figure 52.b and is usually called LCL filter. Various design methods present in literature [48] [49] [50] use, as design parameters, base units of the selected system:

$$Z_b = \frac{E_n^2}{P_n}$$
$$C_b = \frac{1}{2\pi f_1 Z_b} \tag{3.9}$$

Where Z_b is the base impedance and C_b is the base capacitance of the system. The resonant frequency of the filter f_{res} should be in the range of $10f_1 < f_{res} < 0.5f_{sw}$ to prevent filter interaction with important dynamics in the system. Considering that the mains can be considered a short-circuit for all matter harmonics, the circuit in Figure 52.b becomes easy to analyze at switching frequency. The transfer functions of the system, neglecting the mains become:

$$\frac{i_c(s)}{u_c(s)} = \frac{s^2 L_g C_f + 1}{\left(\frac{s^2 L_g L_i C_f}{L_i + L_c} + 1\right)} \frac{1}{s(L_i + L_g)} \tag{3.10}$$

[5] This consideration is explained in the LCL filters calculation, in which grid inductance is considered.

$$\frac{i_g(s)}{i_c(s)} = \frac{1}{s^2 L_g C_f + 1} \tag{3.11}$$

Where $i_c(s)$ is the harmonic component of the converter's current, L_g is the grid inductance $L_t + L_f$ and $i_g(s)$ is the harmonic current flowing through the grid, the direction depends of the function of the converter (i.e. absorbing as a rectifier). Defining the characteristic quantities of the filter as:

$$\begin{aligned} \omega_{res}^2 &= \frac{L_i + L_g}{L_g L_i C_f} \\ \omega_{LC}^2 &= \frac{1}{L_g C_f} \end{aligned} \tag{3.12}$$

At switching frequency ($s = j2\pi f_{sw} = j\omega_{sw}$) Eq.3.10 and Eq2.11 can be re-written as:

$$\left|\frac{i_c(\omega_{sw})}{u_c(\omega_{sw})}\right| \cong \underbrace{\frac{\omega_{res}^2}{\omega_{LC}^2}}_{1st\ factor} \quad \underbrace{\frac{1}{\omega_{sw}(L_i + L_g)}}_{\substack{standard\ inductor \\ attenuation}} \tag{3.13}$$

$$\left|\frac{i_g(\omega_{sw})}{i_c(\omega_{sw})}\right| \cong \frac{\omega_{LC}^2}{\omega_{sw}^2} \tag{3.14}$$

In Eq.3.13 two factors can be recognized: the second one is the composite inductor behavior of high order harmonics reduction, while the first one is strictly degrading the performance since $\omega_{res}^2 \gg \omega_{LC}^2$ (i.e. causing more current harmonics). Analyzing said factor yields:

$$\frac{\omega_{res}^2}{\omega_{LC}^2} = \frac{\frac{L_i + L_g}{L_g L_i C_f}}{\frac{1}{L_g C_f}} = 1 + \frac{L_g}{L_i} \tag{3.15}$$

Eq.3.15 demonstrates explicitly the degrading effects of grid inductance and justifies the choice $L_g \ll L_i$ so that the factor $\frac{\omega_{res}^2}{\omega_{LC}^2}$ is near 1, remembering that $\min(L_g) = L_t$. So far, the effects of the LCL filter seem negative, however even if the system is generating more harmonics, they are not entering the public grid due to the presence of the shunting capacitor. The amount of grid injected harmonics is governed by the ratio $\frac{\omega_{LC}^2}{\omega_{sw}^2}$ in Eq.3.14, so there is a need to minimize ω_{LC}^2, which means that both L_g and C_f need to be of significant value. As mentioned L_g needs to be restricted, usually around 0.1 L_i, and C_b also needs to be restricted because of reactive power absorption from the grid, which is quantified as:

$$C_f = xC_b \tag{3.16}$$

Where x is the accepted power factor reduction, usually around 5 percent. Inductor L_i is still bounded by previous consideration and Eq.3.8.

The proposed design procedure is the following:

1. Design L_i from Eq.3.8 considering the maximum ripple allowable.
2. Decide the size of capacitor C_b by setting x.
3. Design L_g such that Eq.3.14 yields the desired reduction in grid injection. The additional generated harmonics are contained in r such that $L_g = rL_i$.
4. Check that $f_{res} = \frac{1}{2\pi}\sqrt{\frac{L_i+L_g}{L_g L_i C_f}}$ is in the range $10f_1 < f_{res} < 0.5f_{sw}$.

After following the design procedure, the effects of L_g and C_f can be ignored, as long as: r is chosen little and the peak of the resonance present in Eq.3.10 is well damped, either by a resistive component R_D in series with the capacitor, or other means of active control. The amount of damping depends on the type of control employed; a good rule of thumb is to keep the damping factor of the filter around 20% when using passive components to avoid heat dissipation. The values usually suggested in literature is $R_D = \frac{1}{3*C_b*\omega_{res}}$ which yields a damping factor ξ_{pf} of:

$$\xi_{pf} = \frac{1}{2}\left[\frac{\frac{L_i + L_g}{L_g L_i}\omega_{res}}{R_D}\right] = |_{R_D=\frac{1}{3*C_b*\omega_{res}}} \frac{1}{6} = 0.16 \tag{3.17}$$

The losses in the damping resistor can be calculated as the joule losses of the currents shunted by the capacitor branch shown in Eq.3.18, which decrease the efficiency of the system.

$$P_D = 3R_D \sum_h i_c(h) - i_g(h)^2 \tag{3.18}$$

In the next subchapter a mathematical model of the AC/DC converter will be derived, strong of the assumptions made in this chapter that allow for the neglection of the additional $L_g C_f$ filter, which greatly simplifies the operations, making the inductor of inductance $L_i = L$ the only AC component employed in mathematical artifices.

3.3 MATHEMATICAL MODEL

The scope in this chapter is to identify a sound mathematical model for the circuit in Figure 53, where the voltage-current convention is that of the generators for the three phase side and that of the users for the battery, represented by the DC voltage generator, this means that positive power $P_{3ph} \approx P_{dc}$ is positive when the converter is working as a rectifier and negative when the converter is working as an inverter.

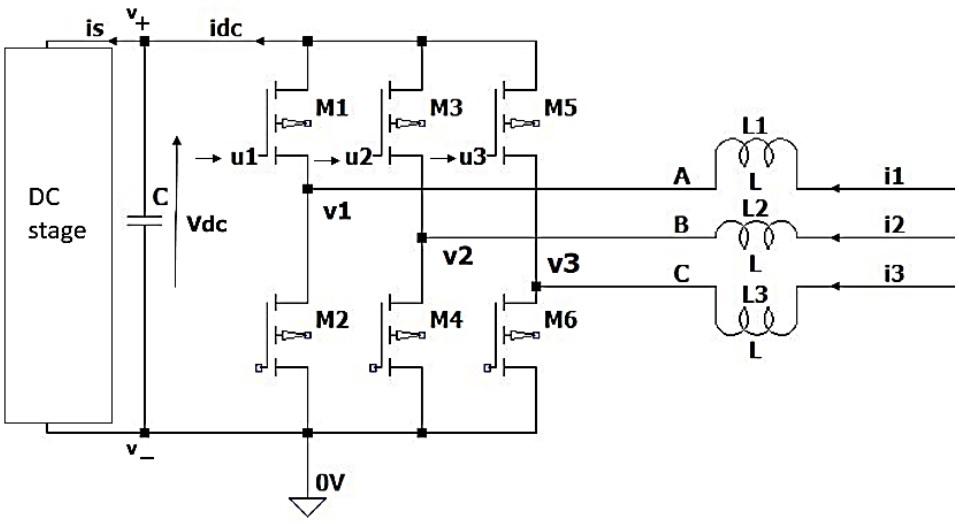

Figure 53 ACDC converter circuit

3.3.1 Mathematical Definitions

Before starting the analysis, some conventions will be laid out, so that there will be no misunderstanding in between mathematical operations.

For any signal $x(t)$ defined for $t \in (-T, +inf]$ where T is the period of the signal, and of C^1 regularity, the following Fourier expansions is valid:

$$x(t) = \sum_{k=-\infty}^{\infty} x_k(t) e^{jk\omega t} \tag{3.19}$$

Where $T = \frac{2\pi}{\omega}$, ω is the fundamental pulsation and $x_k(t)$ is the time-varying, k th order harmonic of the signal $x(t)$, which is defined in Eq2.19 and is a complex quantity.

$$x_k(t) = \frac{1}{T} \int_{t-T}^{t} x(\tau) e^{-jk\omega\tau} d\tau \tag{3.20}$$

The first order harmonic model presented in this thesis is based on the analysis of first order harmonics of the signals present in the circuit. Using Eq.3.19 it is possible to recover a truncation of the initial signal $x(t)$ by expanding the series and discarding higher order harmonics:

$$x(t) = x_o(t) + x_{-1}(t)e^{-j\omega t} + x_1(t)e^{j\omega t} + \overbrace{\sum_{k=-\infty}^{-2} x_k(t)e^{jk\omega t} + \sum_{k=2}^{\infty} x_k(t)e^{jk\omega t}}^{higher\ order\ discarded\ terms} \cong$$
$$x_o(t) + x_{-1}(t)e^{-j\omega t} + x_1(t)e^{j\omega t} = x_o(t) + 2\left[Re\left(x_1(t)\right)\cos(\omega t) + Im\left(x_1(t)\right)\sin(\omega t)\right] \tag{3.21}$$

In Eq.3.20 the property that $x_{-1}(t)$ is the complex conjugate of $x_1(t)$ has been used.

Time varying harmonics $x_k(t)$ have beneficial properties that allow for the uncoupling of nonlinear systems, as provided in [51] with sound proofs. The first property in Eq.3.22 defines how the derivative acts on the time varying spectral components of the signal, allowing for the manipulation of state variables in a physical system. The second property in Eq.3.22 defines

how the harmonics of two different signals $x(t)$ and $y(t)$ interact with each other, allowing for the simplifications of non-linearities, which are still present since both signals spectral harmonics $x_k(t)$ and $y_k(t)$ are time-varying, but can be accounted for in a small signal reference model.

$$\frac{d}{dt}x_k(t) = \left[\frac{d}{dt}x(t)\right]_k - jk\omega x_k(t) \rightarrow \left[\frac{d}{dt}x(t)\right]_k = \frac{d}{dt}x_k(t) + jk\omega x_k(t)$$
$$[x(t) * y(t)]_k = \sum_{i=-\infty}^{\infty} x_{k-i}(t) * y_i(t) \tag{3.22}$$

In Eq.3.22 the term $\left[\frac{d}{dt}x(t)\right]_k$ indicates the kth harmonic of the derivative of $x(t)$. Notice that if the signal reaches a stationary condition $\frac{d}{dt}x_k(t) = 0$ Eq.3.22 fully describes the classical phasor representation $\left[\frac{d}{dt}x(t)\right]_k = jk\omega x_k(t)$.

For all further analysis, the dependence on time of the sliding harmonic $x_k(t)$ will be dropped for brevity, and it will be indicated by $\langle x\rangle_k$, where the brackets denote the sliding harmonic operation of Eq.3.20. The sliding harmonics of order $k \geq |2|$ will be considered zero valued (e.g. $\langle x\rangle_2 = \langle x\rangle_{-2} = 0$). This last choice introduces approximation errors in the model, and can be amended by expanding the order of harmonics considered, since neither equations in Eq.3.22 impose restrictions, however the models might then become of difficult to manage for straight-forward considerations. Some operations appear often when considering the first sliding harmonic and should be kept in mind:

$$\langle x * y\rangle_1 = \sum_{i=-\infty}^{\infty} x_{1-i}(t) * y_i(t) = \langle y\rangle_0\langle x\rangle_1 + \langle y\rangle_1\langle x\rangle_0 \tag{3.23}$$

$$\langle x * y\rangle_0 = \sum_{i=-\infty}^{\infty} x_{0-i}(t) * y_i(t) = \langle y\rangle_0\langle x\rangle_0 + \langle y\rangle_1\langle x\rangle_{-1} + \langle y\rangle_{-1}\langle x\rangle_1 =$$
$$= \langle y\rangle_0\langle x\rangle_0 + 2Re(\langle x\rangle_1\langle y\rangle_{-1})) = \langle y\rangle_0\langle x\rangle_0 + 2(Re\big(\langle x\rangle_1\big)Re(\langle y\rangle_1) + Im(\langle x\rangle_1)Im(\langle y\rangle_1)\big) \tag{3.24}$$

3.3.2 Mathematical State Variables Equations

The three-phase configuration of Figure 53 possesses 4 state variables, 3 for the AC currents and one for the DC voltage. The switches connected to the + (plus) of the DC bus are controlled by $u_1(t), u_2(t), u_3(t)$, whereas the one connected to the – (minus) are controlled by the $-u_1(t), -u_2(t), -u_3(t)$. Control signals $u_1(t), u_2(t), u_3(t)$ are bipolar, which means that $u_k \in [-1,1]\ for\ k = 1,2,3$, as shown in Figure 50.

Writing the three KVLs for the inductor's current, and one KCL for the capacitor's voltage with reference to the circuit in Figure 53 yields:

$$\begin{cases} Li_k = e_k - v_k \\ Cv_{dc} = i_{dc} - i_s \end{cases} for\ k = 1,2,3 \tag{3.25}$$

Where e_k is the phase voltage supplied by the AC grid of phase k. Voltages v_k (converter side AC voltages) need to be defined in terms of state variables and switching functions to obtain a state model. By supposing that the main is a symmetrical set of voltages ($\sum e_k = 0$), the AC and DC side are perfectly isolated ($\sum i_k = 0$) and that the switches follow the following scheme:

$$v_k = \begin{cases} v_+ \,;\, u_k = 1 \\ v_- \,;\, u_k = -1 \end{cases} \; for\; k = 1,2,3 \tag{3.26}$$

By summing up the three current equations it can be concluded that also $\sum v_k = 0$ and finally:

$$\begin{cases} v_k = v_+ * \dfrac{1+u_k}{2} + v_- * \dfrac{1-u_k}{2} = \dfrac{v_{dc}}{2}u_k + \dfrac{v_+ - v_-}{2} \overset{\sum v_k = 0}{\widehat{=}} \dfrac{v_{dc}}{2}u_k - \dfrac{v_{dc}}{6}\sum u_k \\ i_{dc} = \sum (i_k * \dfrac{1+u_k}{2}) \overset{\sum i_k = 0}{\widehat{=}} \dfrac{1}{2}\sum (i_k * u_k) \end{cases} \tag{3.27}$$

Substituting Eq.3.27 results into Eq.3.25 yields the complete non-linear model of Eq.3.28.

$$\begin{cases} L\dot{i_k} = e_k - \dfrac{v_{dc}}{2}u_k + \dfrac{v_{dc}}{6}\sum u_k \\ C\dot{v_{dc}} = \sum (i_k * \dfrac{1+u_k}{2}) - i_s \end{cases} \; for\; k = 1,2,3 \tag{3.28}$$

Under the previously mentioned assumptions exacted in Eq.3.23 and Eq.3.24 the first sliding harmonic order model of Eq.3.28 becomes:

$$\begin{cases} L\dfrac{d}{dt}\langle i_k\rangle_1 \overset{PWM\ sym.}{\widehat{=}} -j\omega L\langle i_k\rangle_1 + \langle e_k\rangle_1 - \dfrac{\langle v_{dc}\rangle_0}{2}\langle u_k\rangle_1 \\ C\dfrac{d}{dt}\langle v_{dc}\rangle_0 = \sum \left(Re\big(\langle i_k\rangle_1\big)Re(\langle u_k\rangle_1) + Im(\langle i_k\rangle_1)Im(\langle u_k\rangle_1)\right) - \langle i_s\rangle_0 \end{cases} \; for\; k = 1,2,3 \tag{3.29}$$

Since the PWM modulation that gives rise to $u_1(t), u_2(t), u_3(t)$ is bipolar and symmetrical, two important simplification have been made in Eq.3.29: $\langle u_k\rangle_0 = 0$ and $\sum\langle u_k\rangle_1$.[6]

There are still three complex AC equations, meaning six equations, which are hard to manage. To reduce the number of equations the *dq* transform can be introduced. For the generic AC variable $f \in \{i, u, e\}$:

$$\begin{cases} f_1 = f_q \cos(\omega t) + f_d \sin(\omega t) \\ f_2 = \left(-\dfrac{1}{2}f_q - \dfrac{\sqrt{3}}{2}f_d\right)\cos(\omega t) + \left(\dfrac{\sqrt{3}}{2}f_q - \dfrac{1}{2}f_d\right)\sin(\omega t) \\ f_3 = \left(-\dfrac{1}{2}f_q + \dfrac{\sqrt{3}}{2}f_d\right)\cos(\omega t) + \left(-\dfrac{\sqrt{3}}{2}f_q - \dfrac{1}{2}f_d\right)\sin(\omega t) \end{cases} \tag{3.30}$$

[6] Simplification as follow:

First equation: $L\frac{d}{dt}\langle i_k\rangle_1 = -j\omega L\langle i_k\rangle_1 + \langle e_k\rangle_1 - \frac{\langle v_{dc}\rangle_0}{2}\langle u_k\rangle_1 - \underbrace{\frac{\langle v_{dc}\rangle_1}{2}\langle u_k\rangle_0}_{0} + \frac{\langle v_{dc}\rangle_0}{6}\underbrace{\sum\langle u_k\rangle_1}_{0}$

Second equation: $\frac{1}{2}\langle\sum(i_k * u_k)\rangle_0 = \underbrace{\frac{1}{2}\sum\langle i_k\rangle_0\langle u_k\rangle_0}_{0} + \sum\left(Re\big(\langle i_k\rangle_1\big)Re(\langle u_k\rangle_1) + Im(\langle i_k\rangle_1)Im(\langle u_k\rangle_1)\right)$

By comparing Eq.3.30 with the respective equations of the three-phase variable in time domain as for Eq.3.21[7], the equivalence can be obtained between *dq* components and sliding harmonics. Eq.3.31, Eq.3.32 and Eq.3.33 describe the relationships for currents, PWM signals and voltages, respectively.

$$\begin{cases} Re(\langle i_1\rangle_1) = \frac{1}{2} i_q & Im(\langle i_1\rangle_1) = -\frac{1}{2} i_d \\ Re(\langle i_2\rangle_1) = \left(-\frac{1}{4} i_q - \frac{\sqrt{3}}{4} i_d\right) & Im(\langle i_2\rangle_1) = \left(-\frac{\sqrt{3}}{4} f_q + \frac{1}{4} f_d\right) \\ Re(\langle i_3\rangle_1) = \left(-\frac{1}{4} i_q + \frac{\sqrt{3}}{4} i_d\right) & Im(\langle i_3\rangle_1) = \left(\frac{\sqrt{3}}{4} f_q + \frac{1}{4} f_d\right) \end{cases} \tag{3.31}$$

$$\begin{cases} Re(\langle u_1\rangle_1) = \frac{1}{2} u_q & Im(\langle u_1\rangle_1) = -\frac{1}{2} u_d \\ Re(\langle u_2\rangle_1) = \left(-\frac{1}{4} u_q - \frac{\sqrt{3}}{4} u_d\right) & Im(\langle u_2\rangle_1) = \left(-\frac{\sqrt{3}}{4} u_q + \frac{1}{4} u_d\right) \\ Re(\langle u_3\rangle_1) = \left(-\frac{1}{4} u_q + \frac{\sqrt{3}}{4} u_d\right) & Im(\langle u_3\rangle_1) = \left(\frac{\sqrt{3}}{4} u_q + \frac{1}{4} u_d\right) \end{cases} \tag{3.32}$$

$$\begin{cases} Re(\langle e_1\rangle_1) = 0 = \frac{1}{2} e_q & Im(\langle i_1\rangle_1) = -\frac{E}{2} = -\frac{1}{2} V_d \\ Re(\langle i_2\rangle_1) = -\frac{\sqrt{3}}{4} E = \left(-\frac{1}{4} i_q - \frac{\sqrt{3}}{4} i_d\right) & Im(\langle i_2\rangle_1) = \frac{E}{4} = \left(-\frac{\sqrt{3}}{4} f_q + \frac{1}{4} f_d\right) \\ Re(\langle i_3\rangle_1) = \frac{\sqrt{3}}{4} E = \left(-\frac{1}{4} i_q + \frac{\sqrt{3}}{4} i_d\right) & Im(\langle i_3\rangle_1) = \frac{E}{4} = \left(\frac{\sqrt{3}}{4} f_q + \frac{1}{4} f_d\right) \end{cases} \tag{3.33}$$

Where E is the peak value of the grid side phase to neutral voltage. Substituting the sliding harmonics - *dq* components relationships (Eq.3.31-33) in one current equation and voltage equation of Eq.3.29 yields the final model of Eq.3.34. The choice of the current equation is of no consequence since it is easy to verify the same results for each one.

$$\begin{cases} \dot{i_d} = \omega i_q - \frac{\langle v_{dc}\rangle_0}{2L} u_d + \frac{E}{L} - r_L i_d \\ \dot{i_q} = -\omega i_d - \frac{\langle v_{dc}\rangle_0}{2L} u_q - r_L i_q \\ \langle \dot{v_{dc}}\rangle_0 = \frac{3}{4C}\left(i_d u_d + i_q u_q\right) - \langle i_s\rangle_0 \end{cases} \tag{3.34}$$

Where small inductor resistances r_L have been considered. Further simplifications are needed to achieve simpler control laws, but these simplifications are dependent on the objective of the control and the presence of additional components on the DC side.

[7] Considering that the AC variables have $\langle f_k\rangle_0 = 0$

Consider now the presence of a strong DC source connected on the DC-Link as in Figure 3 and in accordance with Table 2 this source will never be disconnected. The capacitor-battery KVL can be written:

$$v_{dc} = r * i_{batt} + v_{batt} \rightarrow \dot{v_{dc}} = r_{esr} * \dot{\imath_{batt}} + \dot{v_{batt}} \tag{3.35}$$

Eq.3.35 states that for slow variations of the DC current, the voltage on the DC-Link equals the voltage on the capacitor, which variation can be considered zero in terms of dynamics, especially when battery capacity is large. This also justifies the assumptions that the voltage $\langle v_{dc} \rangle_0$ is constant with respect to the current variations.

Consider small variations of the variables in Eq.3.34 and large capacity battery connected to the DC-Link, so that:

$$\begin{cases} i_d = I_d + \widetilde{\imath_d} \\ i_q = I_q + \widetilde{\imath_q} \\ u_d = U_d + \widetilde{u_d} \\ u_q = U_q + \widetilde{u_q} \\ \dot{v_{dc}} = \dot{v_{batt}} \\ \langle v_{dc} \rangle_0 = V_{dc} \end{cases} \tag{3.36}$$

Where the capital letters are the operating point values around which the model is linearized. Notice this introduces ulterior approximation on the spectral component of the physical variables of the system, which have already been considered restricted in terms of frequency, and now have a finite small amplitude variation. The first order model[8] can be written as:

$$\begin{cases} \dfrac{d}{dt}\widetilde{\imath_d} = \omega(I_q + \widetilde{\imath_q}) - \dfrac{V_{dc}}{2L}(U_d + \widetilde{u_d}) + \dfrac{E}{L} - r_L(I_d + \widetilde{\imath_d}) \\ \dfrac{d}{dt}\widetilde{\imath_q} = -\omega(I_d + \widetilde{\imath_d}) - \dfrac{\langle v_{dc} \rangle_0}{2L}\left(U_q + \widetilde{u_q}\right) - r_L\left(I_q + \widetilde{\imath_q}\right) \\ \dfrac{d}{dt}\langle v_{dc} \rangle_0 = \dot{v_{batt}} \end{cases} \tag{3.37}$$

Finally, the small signal model can be written for the currents:

$$\begin{cases} \dfrac{d}{dt}\widetilde{\imath_d} = \omega\widetilde{\imath_q} - \dfrac{V_{dc}}{2L}\widetilde{u_d} - \dfrac{r_L}{L}\widetilde{\imath_d} \\ \dfrac{d}{dt}\widetilde{\imath_q} = -\omega\widetilde{\imath_d} - \dfrac{V_{dc}}{2L}\widetilde{u_q} - \dfrac{r_L}{L}\widetilde{\imath_q} \end{cases} \tag{3.38}$$

The operating range is restricted to the by specifications of Table 3 for the DC operating points: the reactive part of the current I_q needs to be around zero to achieve high power factor, the direct current I_d is then limited by rated power and the voltage needs to be in battery range, as shown in Eq.3.39:

[8] All higher order approximation terms of the form $\widetilde{xy}$ are considered null.

$$\begin{cases} I_q = \dfrac{V_{dc}}{2\omega L} U_d - \dfrac{E}{\omega L} \cong 0 \\ I_d = \dfrac{V_{dc}}{2\omega L} U_q < \dfrac{2}{3\sqrt{2}} \left| \dfrac{P_n}{E} \right| \\ Vmin < V_{dc} < Vmax \end{cases} \tag{3.39}$$

4 INVERTER CONTROL

4.1 CONTROL IN DQ FRAME

The model in Eq.3.38 can be used to control the currents in the dq frame. In this application the voltage mode will not be needed due to the strong DC source in the battery. The voltage at the output of the AC/DC converter, will only be decided by the needed power transfer between stages, which for balanced operation satisfies the following:

$$P = \sqrt{3} V_{ll} I_{ac} = \frac{3}{2}\left(V_d I_d + V_q I_q\right) \tag{4.1}$$

As already mentioned, $I_q \approx 0$ the relation can be rewritten as:

$$P = \frac{3}{2} V_d I_d = \frac{3}{2} E I_d \rightarrow I_{d_{ref}} = \frac{2}{3\sqrt{2}} \frac{P_{ref}}{E_{rms}} \tag{4.2}$$

So, the current reference is a direct function of how much power is drawn from the mains, which ensures that the converter works in operating range of power. The feedback controller should then ensure that $I_{q_{ref}} = 0$ & $I_{d_{ref}} = \frac{2}{3\sqrt{2}} \frac{P_{ref}}{E_{rms}}$, where the rms value of line voltage is considered constant.

The control to current transfer function $H_C(s)$ of Eq.4.3 for both channels is identical, considering the other current as a disturbance, so only one controller needs to be designed.

$$H_C(s) = \frac{i_d}{u_d}(s)|_{i_q=0} = \frac{i_q}{u_q}(s)|_{i_d=0} = -\frac{V_{dc}}{2r} \frac{1}{s\frac{L}{r_L} + 1} = -K_c \frac{1}{sT_c + 1} \tag{4.3}$$

The current process can be controlled by employing a PI controller with transfer function $H_{PIC}(s) = K_p(1 + \frac{1}{T_i s})$, which allows to rewrite the closed loop current transfer function as:

$$H_{C_{cl}}(s) = \frac{H_{PIC}(s) H_C(s)}{1 + H_{PIC}(s) H_C(s)} = -\frac{sT_i + 1}{\frac{T_c T_i}{K c K_p} s^2 + T_i\left(\frac{1}{K_c K_p} + 1\right) s + 1} = -\frac{sT_i + 1}{T_{C_{cl}}^2 s^2 + 2\xi_C T_{C_{cl}} s + 1} \tag{4.4}$$

Now by imposing stable dynamics to the closed loop time constant $T_{C_{cl}}$ and current damping factor ξ_C, desired performance can be ensured by matching the two sides of Eq.4.4:

$$\begin{aligned} T_i &= 2\xi_C T_{C_{cl}} - \frac{T_{C_{cl}}^2}{T_C} \\ K_p &= \frac{T_C T_i}{K_C T_{C_{cl}}^2} \end{aligned} \tag{4.5}$$

On the choice of closed loop dynamics some considerations are always valid: current damping factor ξ_C needs to be high in order to correctly prevent current overshot that could cause heating in the device when a change in reference is applied. The optimum value in engineering practice is usually considered 0.7. The time constant $T_{C_{cl}}$ represents a tradeoff between performance and

stability of the process: it needs to be low enough that voltage variations in the battery can be neglected (the higher the battery capacity the less stringent this issue) and high enough that it does not interfere with switching harmonics, where the model loses all validity. A good rule of thumb is to keep the $T_{C_{cl}}$ over five times the period of the PWM generator. The average regulating scheme is synthesized in Figure 54 where $id^* = i_{d_{ref}}$.

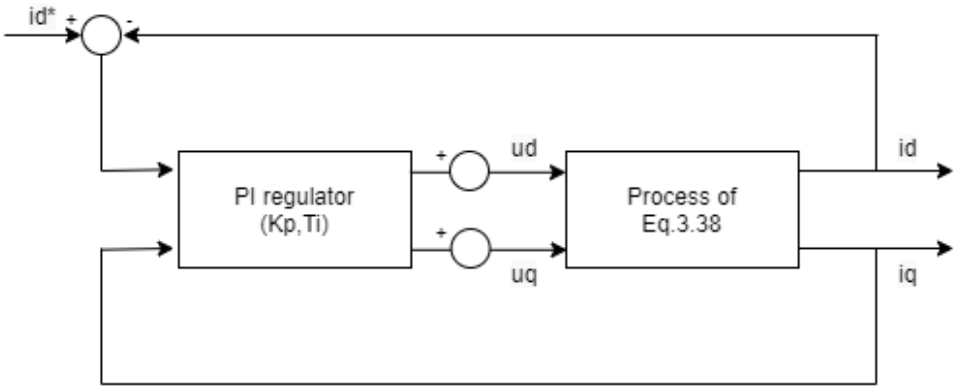

Figure 54 Average current controlled model of a PWM ACDC converter

4.1.1 Design Example

From the open loop current transfer function in Eq.4.3 it can be noticed that the plant only changes its behavior when the DC-side voltage V_{dc} changes, when the passive components on the grid-side remain the same. Consider now a battery that does not have a wide range of operating points, which is common for EV batteries and Li-ion batteries in general. The specifics of Table 5 sets the range from 590 V to 810 V, which for all purposes in this case just means a 3 dB difference in the DC gain of Eq.4.3; so it can be assumed that the designed control loop would work throughout the operating range, however the filter design in 3.2 still needs to be satisfied in order for model in Eq.3.38 to be valid.

Consider the values in Table 3 for AC-side filter sizing as per procedure in 3.2. Base quantities become $Z_b = \frac{E_n^2}{P_n} = \frac{400^2}{11^5} \cong 16\Omega$ and $C_b = \frac{1}{2\pi f_1 Z_b} \cong 0.2\ mF$, and consider an inner inductance $L_i = 6\ mH$. The maximum reduction in power factor x can then be set to 2.5%, the r factor is chosen little as to reduce harmonic production ($r = 0.05$). The calculated parameters are $L_i = 6\ mH$, $L_g = 0.3\ mH$, $C_f = 50\ uF$ provide a reduction in injected harmonics of $1 - \frac{\omega_{LC}^2}{\omega_{sw}^2} = 0.99$ considering a switching frequency of 10 kHz.

Now considering $r_L = 0.1\ \Omega$ and only $L_i = L$ for the purposes of control loop design, and imposing closed loop performance as $\xi_C = 0.7,\ T_{C_{cl}} = 1\ ms$ the PI control parameters can be calculated with Eq.4.5 and yield: $T_i = 2\xi_C T_{C_{cl}} - \frac{T_{C_{cl}}^2}{T_C} = 0.0014\ s$ and $K_p = \frac{T_C T_i}{K_C T_{C_{cl}}^2} = 0.0237$.

Simulation test is carried out in MATLAB Simulink on an average model. Results of a step in drawn power, and by consequence in current (of around 10 A), can be observed in Figure 54. The blue current represents i_d and follows closely the reference change, even if the

performance results degraded, as it shows an uncharacteristic spike for a system with 0.7 of damping factor, however the speed of the loop is satisfactory and the amplitude of the spike is only of 2 dB. The current i_q (in orange) does not receive any difference in reference, as the reactive power absorbed is kept to 0, but ripples occur due to system coupling as per Eq.3.38. where both currents act as disturbances with respect to the other.

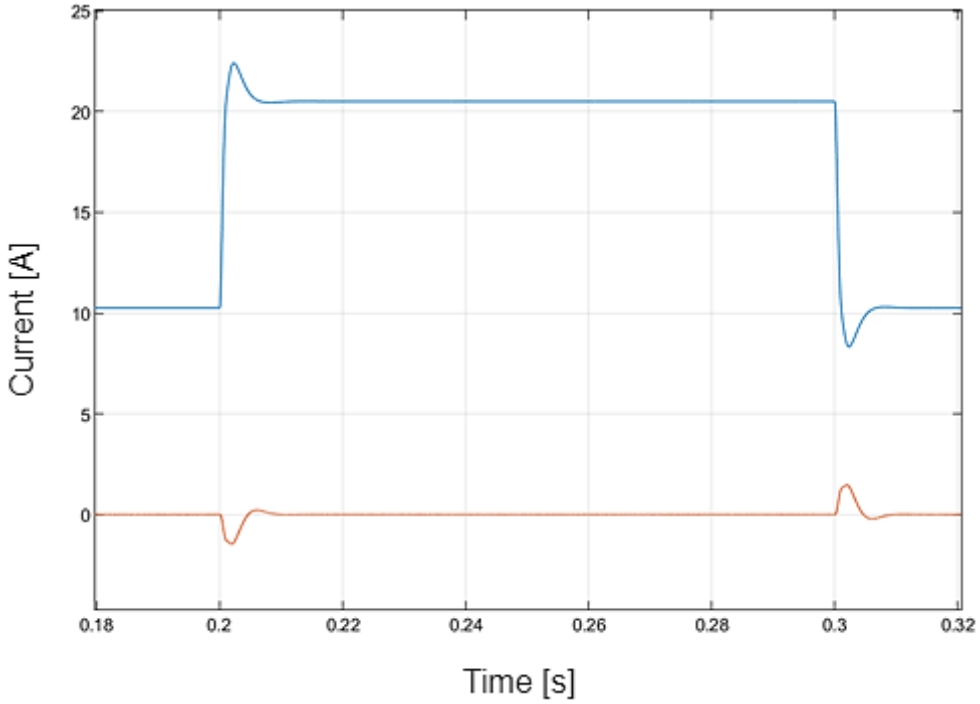

Figure 55 Performance of current regulator under a step variation in reference

The effects of current coupling can be reduced via a feedforward compensation. Consider the first equation of Eq.3.38 and consider now the effects of a variation of i_q while i_d remains constant.

$$\frac{d}{dt}\tilde{i_d} = \omega\tilde{i_q} - \frac{V_{dc}}{2L}\widetilde{u_d} - \frac{r_L}{L}\tilde{i_d} \overset{i_d=0}{\Rightarrow} \widetilde{u_d}^* = \frac{2\omega L}{V_{dc}}\tilde{i_q}^* \tag{4.6}$$

The result of Eq.4.6. is the provoked disturbance on the control $\widetilde{u_d}^*$ which can be compensated by employing a static gain and correcting the duty cycle. If the static gain is equal to $\frac{2\omega L}{V_{dc}}$ the feedforward perfectly compensates the effects of coupling, however delays in the control might reduce the effectiveness of the compensation, effectively resulting in a ripple of reduced order. Figure 56 represents the new control diagram, while Figure 57 clearly shows the effect of the uncoupling structure: current i_q shows little transients when reference change of i_d occurs.

4.1.2 Voltage Control

Since the converter connects two active components (the AC grid and the Battery) there is no need to control voltage for either side however, in startup phase it is necessary to enforce the voltage at one side of the converter. The process is commonly known as pre-charge, the voltage

at the DC side is brought to the level of battery voltage to prevent substantial inrush of current in or out the capacitor.

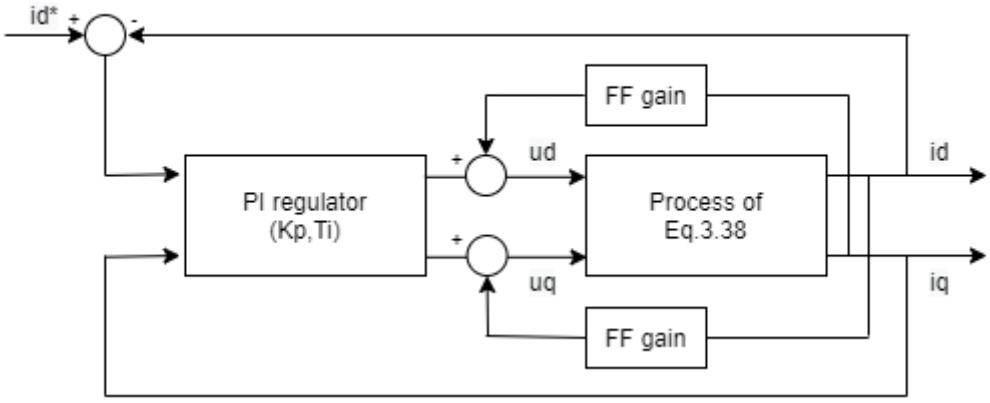

Figure 56 Control loop with feedforward control of gain FF Gain

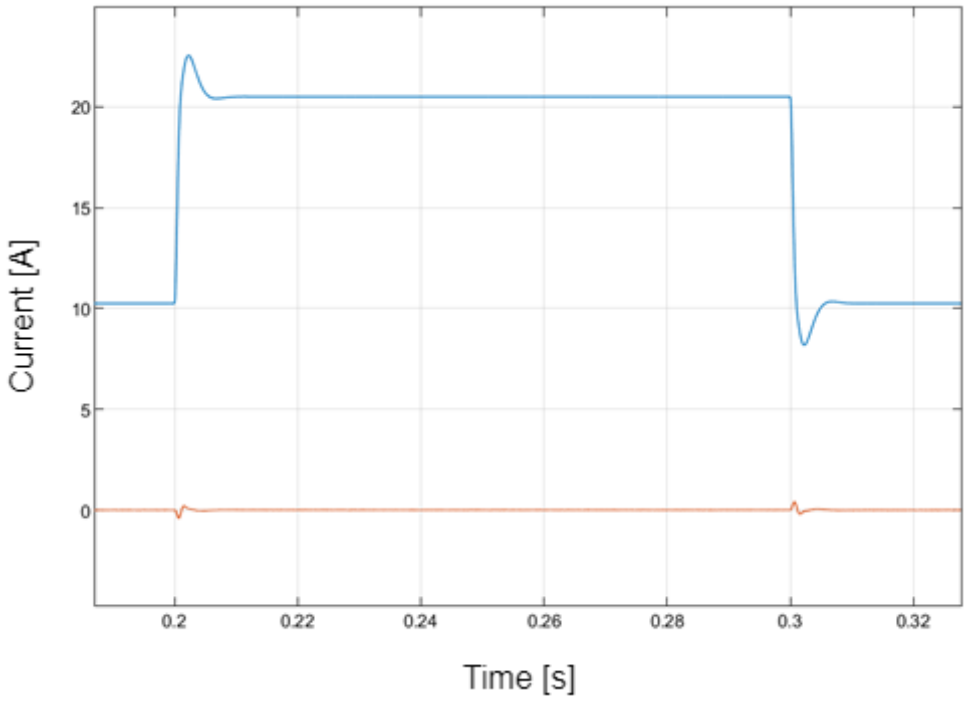

Figure 57 Performance of current regulator under a step variation in reference with FF gain $\frac{2\omega L}{V_{dc}}$

The charging circuit is completed with a damping resistor, which is excluded when the voltage level at DC side reaches rectified grid voltage. Then a control loop is employed to regulate the voltage at the condition $v_{dc} = v_{batt}$, so that, when the connection between the converter and battery is made, no current flows. The transfer function that represents the charging process can be calculated by Eq.3.34, considering null drawn reactive power ($I_q = 0$), a fixed DC voltage level ($V_{dc} = V_{batt}$) and no transferred power ($I_s = 0$). Neglecting losses and considering regime upon said restrictions yields:

$$I_d = -\frac{4}{3}\frac{I_s}{U_d} = 0;\ U_q = -\frac{2\omega L I_d}{V_{dc}} = 0;\ U_d = \frac{2E}{V_{dc}} \tag{4.7}$$

Considering the current control loop described in 4.1 to enforce the current values, the voltage differential equation of Eq.3.35 is rewritten in Eq.4.8 as an integrator gain. The control strategy is therefore easily implemented with a proportional controller of the form $H_{PV}(s) = K_{pV}$. The gain K_{pV} needs to be low enough so that the speed of the voltage controller does not overtake the current regulation loop which is used to enforce the condition upon which Eq.4.8 is based.

$$\langle \dot{v_{dc}} \rangle_0 = \frac{3}{4C}\left(\overbrace{\widetilde{I_d}\widetilde{u_d}}^{=0} + \widetilde{\imath_d} U_d \right) = \frac{3}{2C}\frac{E}{V_{dc}}\widetilde{\imath_d} \tag{4.8}$$

The choice of K_{pV} is tailor fit to the capacitance of the output capacitor of the DC side. Considering the example in 4.1.1 and a capacitance of 10 uF, the current control loop has a closed loop time constant $T_{C_{cl}} = 1\ ms$, meaning that the bandwidth of the voltage control needs to be such that $T_{V_{cl}} > 10\ T_{C_{cl}}$ which implies, from open loop considerations, that $K_{pV} < \frac{2\pi}{10T_{C_{cl}}}\frac{2C}{3}\frac{V_{dc}}{E} \cong 0.01$. From a physical standpoint, it means that the difference in voltage is translated in a current setpoint of a hundredth in magnitude, which is a logical choice considering that the voltage range is that of hundreds and the current range that of tens: in current control $max(I_{d_{ref}}) = \frac{2}{3\sqrt{2}}\frac{P_{ref}}{E_{rms}}$ which is limited to around 20 A. The final control scheme is shown in Figure 58.

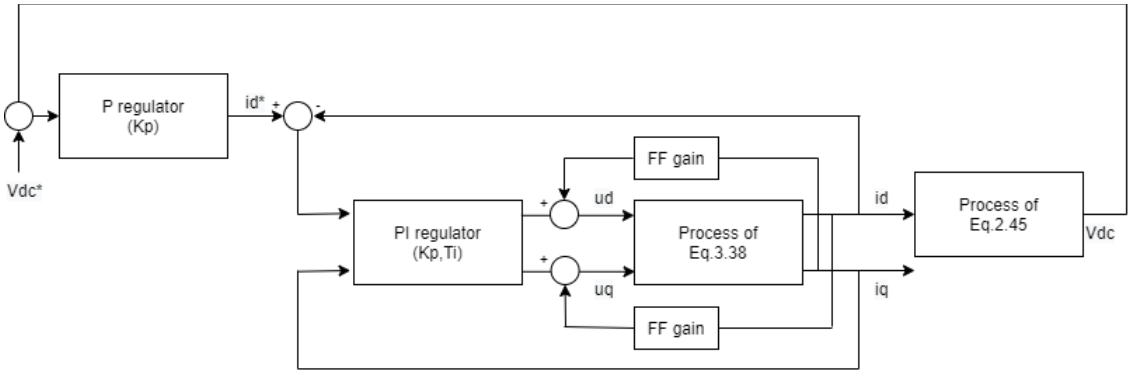

Figure 58 Voltage control mode for start-up

4.2 GRID INTERACTION

Until now the interaction between grid impedance and input impedance of the device has been ignored attributing a value to the grid inductance decisively less that of the grid-side impedance of the LCL filter. However, the installation near low power transformer might change the ratio of inductances which then would need to be considered in the control scheme for two reasons:

1. The resonance of the LCL filter gets modified, and degrades the performance, which can be read by the control loop if not artificially filter out.

2. The value of the equivalent inductance grid-side could be comparable with the inverter-side inductance modifying its dynamic behavior.

Practically when the MV/LV transformer associated with the supply point has secondary inductance L_t (which dominates the grid inductance) of value near the value of L_g it cannot be ignored without modifying the device's performances (choosing $L_f = 0$ is unsuitable for large transformers). Considering 4.1.1 the chosen grid-side inductance L_g is 0,3 mH and considering some common MV/LV sizes for transformer in Table 10, the range of interaction can be estimated. For low power transformers (*Sn<160 kVA*) the two values are comparable, a MATLAB Simulink simulation of the inverter shows the effects of adding the transformer inductance for different sizes in Figure 59, where the depicted varaible is still direct current i_d.

Table 10 MV/LV transformers size comparison with grid-side filter inductance

Sn (kVA)	**Vcc (p.u.)**	**Z_t (Ω)**	**L_t (mH)**	**$\frac{L_t}{L_g}$**
5000	0,1	0,003	0,010	0,034
2500	0,1	0,006	0,020	0,068
1000	0,1	0,016	0,051	0,170
750	0,08	0,017	0,054	0,181
400	0,08	0,032	0,102	0,340
250	0,06	0,038	0,122	0,408
160	0,06	0,060	0,191	0,637
100	0,06	0,096	0,306	1,019
50	0,06	0,192	0,611	2,038
25	0,06	0,384	1,223	4,076

The magnitude of the effects on the filter of the transformer impedance can be estimated by comparing the input impedance of the converter considering the near side inductance , with the LC portion of the filter, via Middlebrook's theorem in the form reported in Eq.4.9 to evaluate the low frequency effects on the lower frequency range.

$$H(s) = H^0(s)\frac{1 + \frac{Z(s)}{Z_n(s)}}{1 + \frac{Z(s)}{Z_d(s)}} \tag{4.9}$$

Where $H(s)$ is the new transfer function with the LC filter inserted, $H^0(s)$ is the transfer function with the LC filter short circuited (present analysis), $Z(s)$ is the impedance of the LC filter, $Z_d(s)$ is the driving point impedance of the converter as seen by the extra elements and $Z_n(s)$ is the double-null-injection driving point impedance[9] as seen by the extra element. The function $H(s)$ to evaluate anew is $H_{C_{cl}}(s) = \frac{\widetilde{i_d}(s)}{i_d^*(s)}$ of Eq2.41 which is affected by low frequency

[9] $Z_n(s)$ is found by replacing the extra element with a second test signal source (either current source or voltage source as appropriate). Then, $Z_n(s)$ is defined as the ratio of voltage across the terminals of this second test source to the current leaving its positive terminal when the output of the system's transfer function is nulled for any value of the primary input to the system's transfer function.

behavior of the filter, and governs the dynamics of Figure 59. The control loop affects the driving point impedance $Z_d(s)$ because the d-current feedback modifies said current by changing the equivalent voltage source of the converter ($\langle v_{dc} \rangle_0 u_d$) thus modifying the current drawn. The equivalent circuit and process can be visualized in

Figure 60 where the LCL filter has been reported in *dq-frame*, but cross terms have been ignored. The analysis revolves around the concept that if $\big(Z(s) \ll Z_d(s)\big)$ and $\big(Z(s) \ll Z_n(s)\big)$ function $H_{C_{cl}}(s)$ remains unchanged.

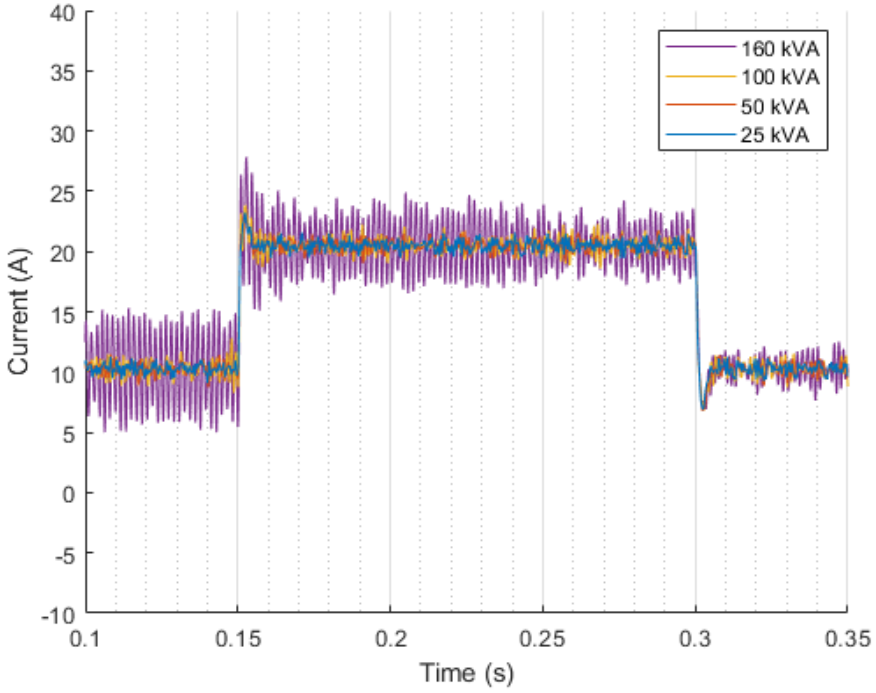

Figure 59 Dynamic performances under different transformer size

The value of the LC filter impedance is easily calculated as:

$$Z(s) = sL_t \,//\, \left(\frac{1}{sC_f} + R_d\right) \tag{4.10}$$

The driving point impedance $Z_d(s)$ can be calculated accounting for the feedback control by analyzing the relationship between the small signal relationship ($\frac{\widetilde{\imath_d}}{\tilde{e}}$) which can be written via Mason's formula for single feedback loop:

$$Z_d(s) = \frac{H_{PIC}(s)H_C(s)}{1 + H_E(s)} \tag{4.11}$$

Where $H_{PIC}(s)H_C(s)$ is the loop gain of the feedback previously defined in Eq.4.4 and $H_E(s)$ is the $\frac{\widetilde{\imath_d}}{\tilde{e}}$ derived from model in Eq.3.34 when a small variation in grid voltage is considered. In

order to null the output of $H_{C_{cl}}(s)$ the variation in current $\widetilde{\imath_d}$ must be zero, so that $\frac{\widetilde{\imath_d}}{\tilde{e}}$ is definitely zero, which means that $Z(s) \ll Z_d(s)$ is always true. Plotting $Z(s)$ for different transformer sizes in Figure 61 shows that for smaller transformer the module of $Z(s)$ and $Z_n(s)$ are similar around the crossover frequency of the current control ($T_{C_{cl}} = 1\,ms$) therefore modifying the phase margin and causing oscillations.

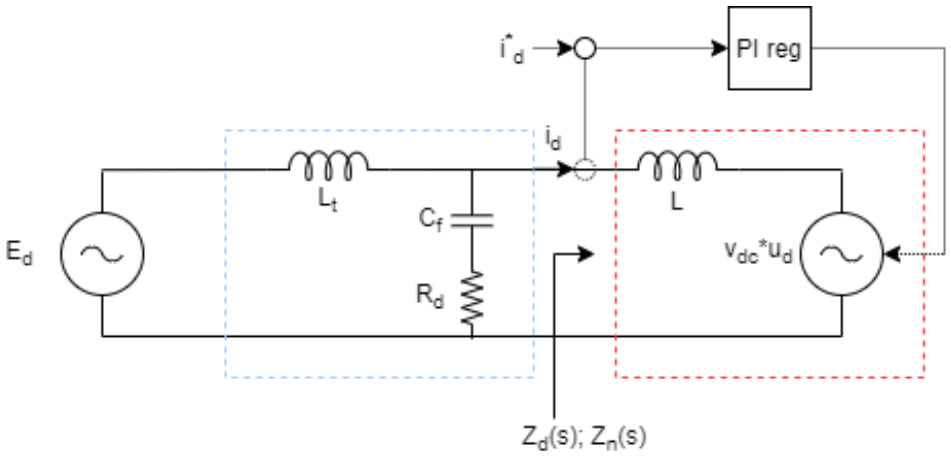

Figure 60 LC interaction circuit with current feedback

In order to reduce the effect in low power transformer setting it is possible to overdamp the system, therefore reducing the peak in the LC filter impedance however doing so with resistor is expensive and inefficient, so next active damping is introduced.

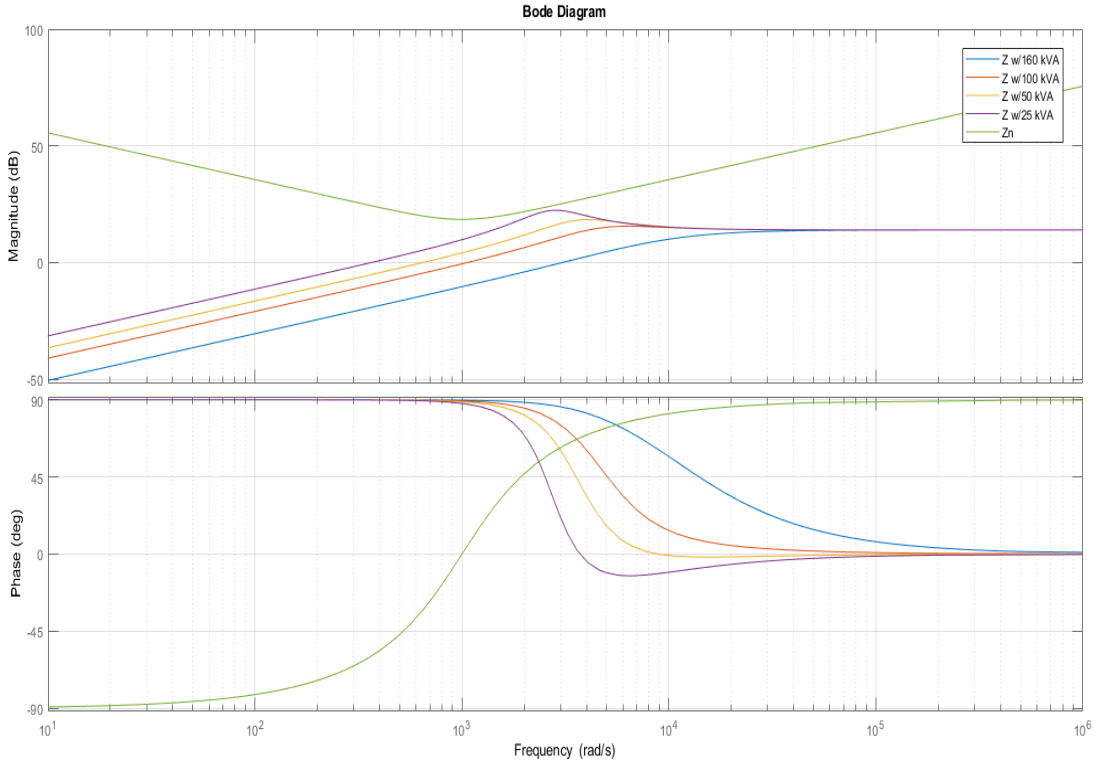

Figure 61 Bode plot of Eq.4.9 for different transformer sizes

4.3 ACTIVE CAPACITOR CURRENT (ACC) DAMPING

Consider now the time domain state equations for an ideal undamped LCL filter for one phase of the three-phase system in Figure 62 described in Eq2.48.

$$\begin{cases} v_i - v_{ci} = L\dfrac{di_{ci}}{dt} \\ i_{ci} - i_{gi} = C_f\dfrac{dv_{ci}}{dt} \\ v_{ci} - e_i = L_g\dfrac{di_{gi}}{dt} \end{cases} \tag{4.12}$$

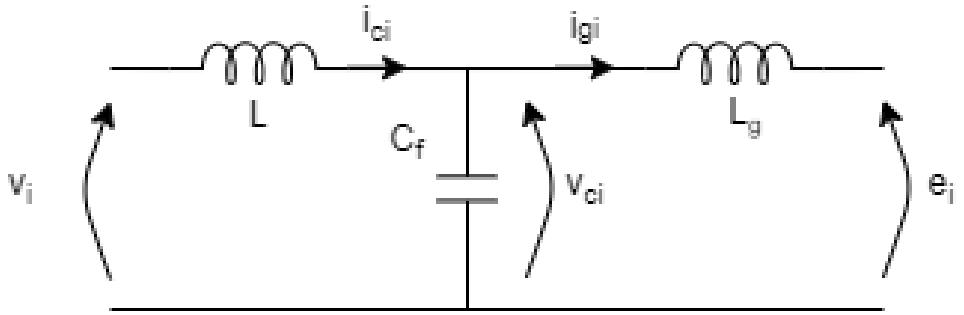

Figure 62 LCL undamped one phase equivalent

Equivalently the systems of equations can be represented, with the control loop, in diagram blocks as in Figure 63. Adding a capacitor current feedback to the effort modifies the behaviour of the filter, and after accounting for the converter gain on phase voltage the behaviour of the LCL filter can be obtained. The controller is translated in the three phase reference to $H_{PIC}(s)^*$ from the native dq $H_{PIC}(s)$ reference, since a stable operation point can be reached by the configuration it is implied that there exists a shift in reference that does not modify performances [52]. The output control signal u_k for phase $k = 1,2,3$ can therefore just be multiplied by half the DC voltage according to Eq.3.29.

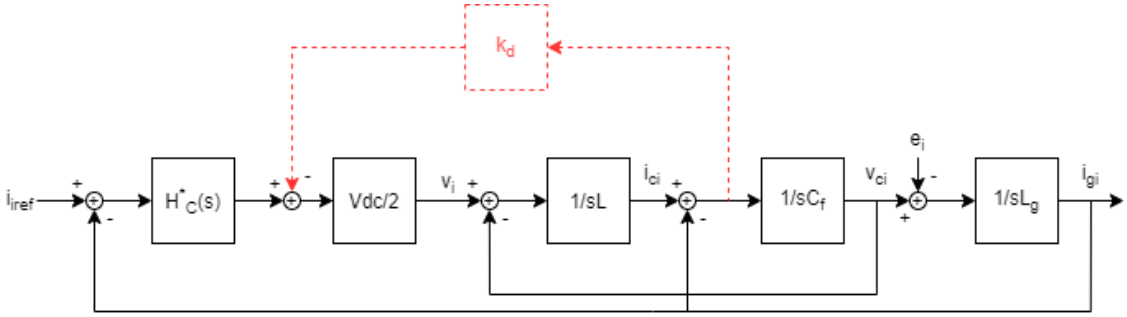

Figure 63 Block Diagram of Control and LCL Filter

The closed loop performance of the block diagram can be evaluated again using Mason's formula for adjacent[10] loops to calculate the closed loop behaviour of the filter, the open loop performance of the converter can be calculated in Eq.4.13 since the feedback is now drawn

[10] Closed loop transfer function is $\frac{i_{iref}}{i_{gi}} = \frac{G(s)}{1+T_n(s)}$. Loop gain is calculated via $T_n(s) = \sum_{i=1}^{n} T_i$ where n is the number of loops inside $i_{iref} \rightarrow i_{gi}$ and T_i is the i-th loop gain, $G(s)$ is the forward path gain.

from the grid current i_{gi} (before considering the effects of the full filter this choice is not observable in an analytic setting):

$$T(s) = \frac{\frac{V_{dc}}{2} H^*_{PIC}(s)}{s^3 L_g L C_f + s^2 \frac{L_g C_f k_d V_{dc}}{2} + s(L_g + L)} \tag{4.13}$$

By making an appropriate choice of k_d the system can properly be damped. The damping factor in the denominator can be recognized in Eq2.50. The performance variation with grid impedance can analysed by making L_g vary in the range of Table 10, doing so allows to determine the beneficial effect of grid impedance on damping when active filtering is present. Figure 64 presents the variation of the active filter damping and a traditional passive damping[11] with grid impedance. Usually the system presents a minimum damping that needs to be granted, which is ultimately also affected by connections conditions. This final damping value can be achieved by overdamping the system with a passive resistor over the solutions usually is inefficient or too greatly diminishes switching harmonics filtering.

$$\xi_d = \frac{\frac{L_g C_f k_d V_{dc}}{2}}{2 L L_g C_f} * \sqrt{\frac{L L_g C_f}{L + L_g}} = \frac{k_d V_{dc}}{4L} \sqrt{\frac{L L_g C_f}{L + L_g}} \tag{4.14}$$

The control loop, along with active damping, is now suited to be discretized, to be implemented with a digital controller, however this poses further questions which will be analysed next.

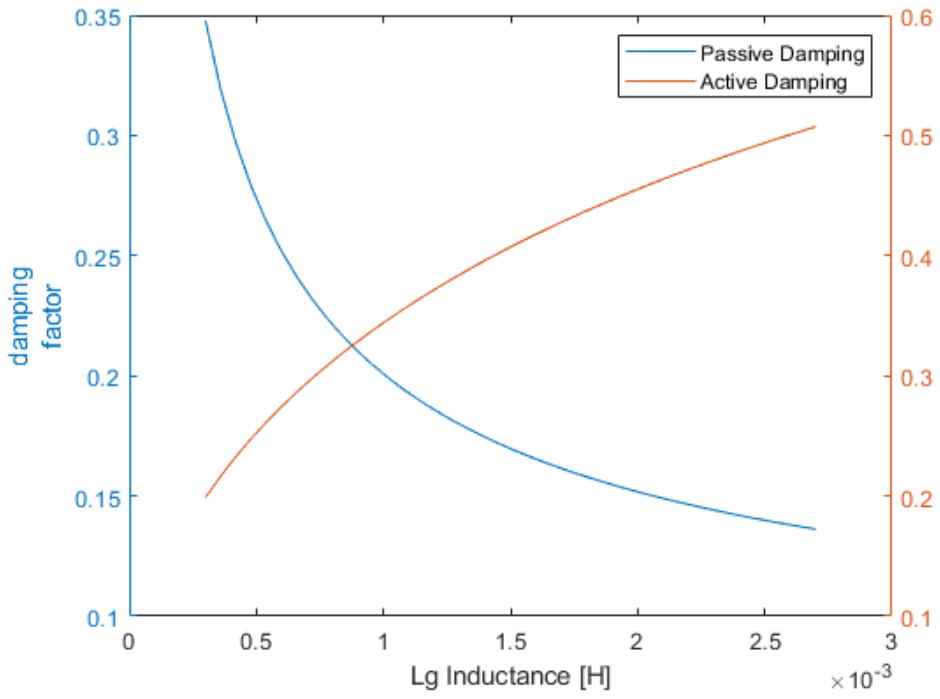

Figure 64 Variation of damping factor with grid impedance

[11] The traditional damping factor refers to series resistor: $\xi_c = C_f R_d \sqrt{\frac{L+L_g}{L L_g C_f}}$, as in circuit in Figure 60.

4.3.1 Digital Control

A continuous PI control in the dq frame and an active capacitor current feedback have been presented until now, however, in modern control system the control is implemented in discrete form. Discrete controls can be modified more easily and allow for the accounting on intrinsic delays in the control loop, for example sampling of the feedback. Since the signal must be acquired and processed by a computer, other delays are added in the control scheme: most notably the computational delay introduced by calculations on the feedbacks T_D and sampling related delays due to the Boolean decision on gate signals made in the PWM modulator T_S. The calculations need necessarily to be completed before the next PWM choice, which will update the control effort one period after so that $0 < T_D < T_S$, when $T_D = T_S$ the system is synchronous. The PWM delay can be estimated via the ZOH transfer function in Eq.4.15, where the control effort u_i is held on for T_S, before getting compared with the carrier.

$$G_h(s) = \frac{1 - e^{sT_s}}{s}\Big|_{s=j\omega} = \frac{\sin(0.5\omega T_s)}{0.5\omega} e^{-j0.5\omega T_s} \approx T_s e^{-j0.5\omega T_s} \rightarrow T_s e^{-0.5sT_s} \tag{4.15}$$

The synchronous computation delay can then be calculated as $G_d(s) = e^{-sT_s}$. An updated control diagram is shown in Figure 65.

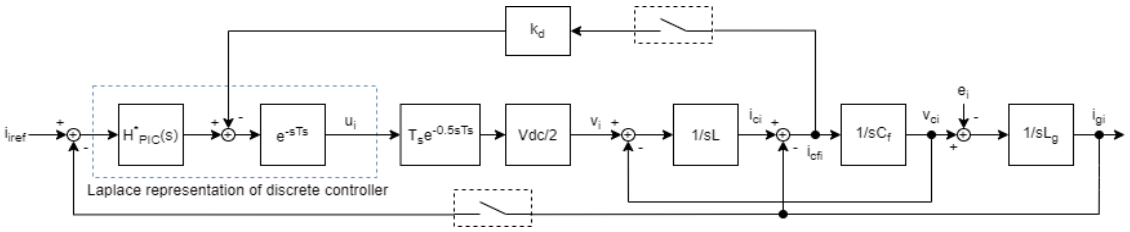

Figure 65 Block Diagram of Control and LCL Filter with equivalent delays

Note that the current compensator $H^*_{PIC}(s)$ has undergone two transformations: one passing from the digital domain ($z \rightarrow s$) and one passing from dq to abc reference ($dq \rightarrow abc$). The former can be seen as the reverse of a ($s \rightarrow z$) transform so that characteristics are maintained, and it can be achieved with a Tustin Transform of $H_{PIC}(s)$ as in Eq.4.16:

$$H_{PIC}(z) = H_{PIC}(s)\Big|_{s=\frac{2}{T_s}\frac{z-1}{z+1}} = K_p\left(1 + \frac{1}{T_i s}\right)\Big|_{s=\frac{2}{T_s}\frac{z-1}{z+1}} = \frac{T_i}{T_s}\frac{\left(K_p + \frac{T_s K_p}{2T_i}\right)z + \left(-K_p + \frac{T_s K_p}{2T_i}\right)}{z - 1} \tag{4.16}$$

To ease an analysis analogue to the one presented in Figure 61, capacitor current feedback can be manipulated into a parallel impedance representation [53], of impedance Z_{eq}, by changing the injection points of the feedback so that it fits the equivalent circuit represented in Figure 66. The feedback needs to be represented as drawn from voltage v_{ci} and injected into the capacitor

current i_{cfi}, meaning $Z_{eq}(\omega)$ needs to be as per Eq.4.17 to fit the representation[12]. The reference block diagram is given Figure 67.

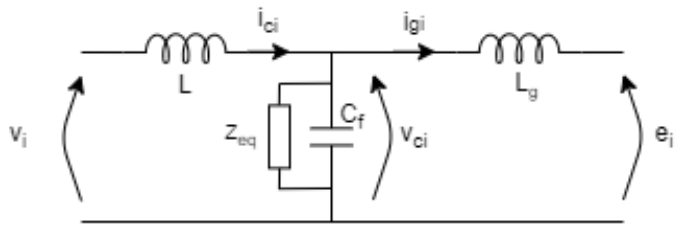

Figure 66 Parallel representation of active damping

$$Z_{eq}(s) = \frac{G_{delay}(s)}{sC_f} = \frac{2LT_s e^{1.5sT_s}}{V_{dc}k_d C_f} = R'_d e^{1.5sT_s} \tag{4.17}$$

Where $G_{delay}(s)$ is the loop gain of current feedback i_{cfi} and R'_d is the equivalent damping resistance introduced by the feedback.

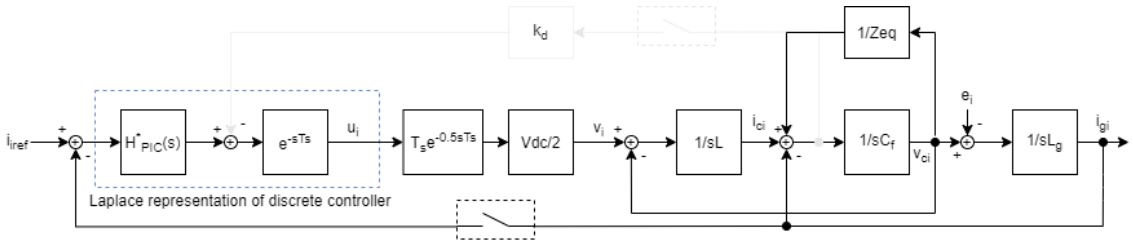

Figure 67 Control block diagram with equivalent impedance representation

Evaluating $Z_{eq}(s)$ in the ω domain allows for important considerations on the filter.

$$Z_{eq}(j\omega) = Z_{eq}(s)|_{s=j\omega} = R'_d \cos(1.5\omega T_s) + jR'_d \sin(1.5\omega T_s) \triangleq R_{eq}(\omega)||jX_{eq}(\omega) \tag{4.18}$$

Where:

$$R_{eq}(\omega) = \frac{R'_d}{\cos(1.5\omega T_s)};\ X_{eq}(\omega) = \frac{R'_d}{\sin(1.5\omega T_s)} \tag{4.19}$$

From Eq.4.19 it can be evinced that the damping effect is different based on the frequency at which the impedance is evaluated, also reactance $X_{eq}(\omega)$ modifies the reactance of the branch, effectively modifying the resonance frequency. Reactance $X_{eq}(\omega)$ can be attributed to a virtual capacitor of capacitance:

$$jX_{eq}(\omega) = \frac{1}{j\omega C_{eq}} \rightarrow\ C_{eq} = -\frac{1}{\omega X_{eq}(\omega)} \tag{4.20}$$

[12] Via basic control theory it is possible to prove that the loop gains of the loops which interest k_d and Z_{eq} must be equal (i.e. $\frac{1}{Z_{eq}(s)}\frac{1}{sC_f} = \frac{1}{sL}\frac{k_d V_{dc}}{2}e^{1.5sT_s}$)

So that when $\sin(1.5\omega T_s)$ is positive there is a negative equivalent capacitance and vice versa when $\sin(1.5\omega T_s)$ is negative.

Parameters in Eq.4.19 are plotted against frequency in Figure 68 to evaluate their effects, three zones can be identified: $f < \frac{f_s}{6}; \frac{f_s}{6} < f < \frac{f_s}{3}; \frac{f_s}{3} < f < \frac{f_s}{2}$.

Considering $k_d > 0$, when $f < \frac{f_s}{6}$ both $R_{eq}(\omega) > 0$ and $X_{eq}(\omega) > 0$, meaning that the effective value of the capacitance is reduced by $\frac{1}{\omega X_{eq}(\omega)}$, increasing the filter resonating frequency, and the damping works the same a passive resistor since $R_{eq}(\omega) > 0$, however when $f = \frac{f_s}{6}$, $R_{eq}(\omega)$ approaches infinity and the system becomes totally undamped.

When $\frac{f_s}{6} < f < \frac{f_s}{3}$, $R_{eq}(\omega) < 0$ and $X_{eq}(\omega) > 0$ which means that the equivalent resistance becomes negative and the equivalent reactance still lowers the capacitance value by $\frac{1}{\omega X_{eq}(\omega)}$, however near $f = \frac{f_s}{3}$ the reactance is so high in value that the capacitance is completely compensated and the resonating frequency is pushed far into the frequency domain, basically nulling the filter effect. This condition critical for the correct functioning of the filter.

When $\frac{f_s}{3} < f < \frac{f_s}{2}$, both $R_{eq}(\omega) < 0$ and $X_{eq}(\omega) < 0$ meaning that the equivalent reactance is now capacitive in nature, and as such lowers the resonating frequency of the filter, effectively increasing the capacitance, which might lead to opting for smaller capacitances in the design of the filter. The latter idea has been proposed recently, however the design procedure is difficult, given the strict range in which the parameters must be determined in order to stay within specified frequency range [54].

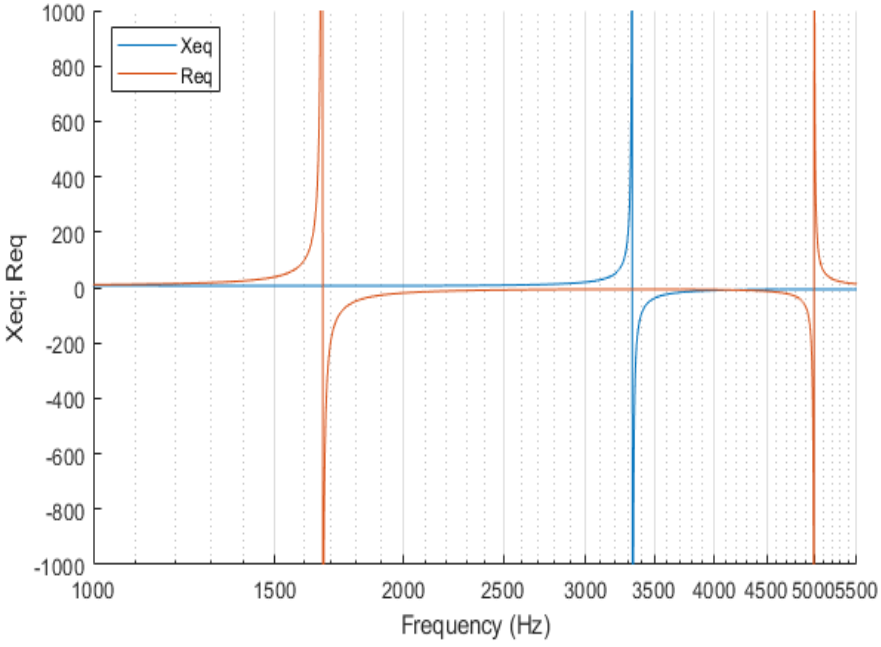

Figure 68 Equivalent parameters with $V_{dc} = 800\,V$, $k_d = 0.03$, $L = 6\,mH$, $C_f = 50\,\mu F$, $T_s = 10^{-4}s$

Closed loop performance can be again evaluated for the diagram in Figure 67, in similar fashion to Eq.4.13, the loop gain can be written as:

$$T_{delay}(s) = \frac{\frac{V_{dc}}{2} H^*_{PIC}(s) e^{-1.5sT_s}}{s^3 L_g L C_f + s^2 \frac{L_g C_f k_d V_{dc}}{2} e^{-1.5sT_s} + s(L_g + L)} \tag{4.21}$$

However, in the Laplace domain transfer function with delays are harder to manage, and determining stability looking for roots with positive real part of denominator containing e^{-sT_s} cannot easily be done in closed form. To evaluate stability, the bode diagram can be useful because it restricts the analysis to $s = j\omega$, allowing the use of Eq.4.19-20 and the physical representation of complex valued impedances in circuit form. Particularly the impedance branch impedance can be substituted by the equivalent circuit in Figure 69. A transfer function that is only valid when $s = j\omega$ can then be written, which employs the new circuit:

$$T_{eq}(s) = \frac{\frac{V_{dc}}{2} H^*_{PIC}(s) e^{-1.5sT_s}}{s^3 L_g L C'_f + s^2 \frac{L_g L}{R_{eq}} + s(L_g + L)} \tag{4.22}$$

Where $C'_f = C_f - \frac{1}{\omega X_{eq}(\omega)}$, the new resonance frequency ω'_{res} can be defined as:

$$\omega'_{res} \approx \sqrt{\frac{L_g + L}{L_g L C'_f(\omega'_{res})}} \tag{4.23}$$

Clearly ω'_{res} cannot rigorously be calculated since the capacitance value C'_f depends on frequency, however a good approximation of the new resonance frequency of the system will be derived in the following considerations.

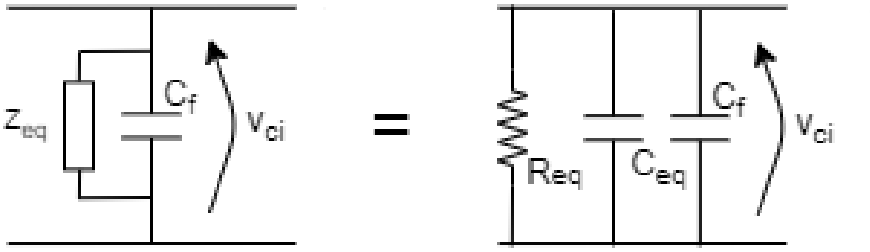

Figure 69 Equivalent parallel capacitor and resistance representation for $Zeq(s)$

Consider $\omega_{res} < \frac{2\pi f_s}{6}$, from Eq2.55 and Figure 68 it can be noticed that for any $\omega'_{res} \neq \frac{2\pi f_s}{6}$ there exist k_d such that the system is sufficiently damped and stable. However, in practice $|k_d| < k_{dmax}$ where k_{dmax} is the maximum backwords gain that does not saturate the controller, so there is a frequency value around $\frac{f_s}{6}$ called f_m such that there exists a k_d that does not saturate the controller that can effectively damp the system. This consideration establishes a necessity for and algorithm to chose k_d such that the system is well damped and stable, conditions can be drawn from the standard Bode theorem:

- The phase margin PM must be positive.
- The gain margin GM_1 at $s = j\omega_{res}$ must be less than zero.
- The gain margin GM_2 at $s = j\omega'_{res}$ must be less than zero.

In other words, once $T_{eq}(s)$ crosses the 0 dB axes in the ω domain with positive PM, it must stay under 0 dB, which is critical for at $s = j\omega_{res}$ and $s = j\omega'_{res}$.

In order to evaluate k_{dmax} one can refer to standard operating condition at nominal frequency, calculate nominal capacitor current and knowing the amplitude of the carrier in the PWM V_m, calculate the maximum nominal feedback that would always saturate the control scheme. To prevent accidental saturation in non-nominal condition a factor of 2 is proposed to be divided on the maximum nominal feedback, so that:

$$k_{dmax} = \frac{\omega_n C_f E}{V_{dc}} V_m \tag{4.24}$$

Given a fixed ω_{res}, the condition $\omega'_{res} \neq \frac{2\pi f_s}{6}$ can be written as:

$$\sqrt{\frac{1}{L_{eq} C'_f(f_s)}} \neq \frac{2\pi f_s}{6} \rightarrow \sqrt{C'_f(f_s)} \neq \frac{\pi f_s \sqrt{L_{eq}}}{3} \rightarrow f_s^2 C'_f \neq \frac{9}{\pi^2 L_{eq}} \tag{4.25}$$

Where $L_{eq} = \frac{LL_g}{L+L_g}$ and in this first step the approximation $f_{res} \approx f'_{res}$ has been used. Eq.4.25 can be further refined by expanding $C'_f(f_s)$, and directly showing the relationship with f_s:

$$f_s^2 \left(C_f - \frac{\sin\left(\frac{3\pi f_{res}}{f_s}\right)}{2\pi f_{res} R'_d} \right) \neq \frac{9}{\pi^2 L_{eq}} \tag{4.26}$$

Eq.4.26 shows again that if $f_s \gg f_{res}$ the capacitor is not affected by the delay, however when $f_s \approx 6 f_{res}$ the capacitor is affected the most since $\frac{3\pi f_{res}}{f_s} \approx \frac{\pi}{2}$, and that coincides with the event $R_{eq} \rightarrow \infty$ which cannot damp the filter. By this logic, in order to avoid choosing a critical sampling frequency for a given filter configuration, the sine can be expanded via Taylor's series[13] when $f_s \rightarrow 6 f_{res}$:

$$f_s^2 \left(C_f - \frac{1 - \frac{\pi^2}{8} \frac{(f_s - 6f_{res})^2}{36 f_{res}^2}}{2\pi f_{res} R'_d} \right) - \frac{9}{\pi^2 L_{eq}} \neq 0 \rightarrow$$

[13] $f(x) = \sin\left(\frac{A}{x}\right) \underbrace{\rightarrow}_{x_0 \rightarrow x} \sin\left(\frac{A}{x_0}\right) - \frac{A}{x_0^2}\cos\left(\frac{A}{x_0}\right)(x - x_0) - \frac{A^2}{x_0^4}\sin\left(\frac{A}{x_0}\right)\frac{(x-x_0)^2}{2} \underbrace{=}_{\frac{A}{x_0} = \frac{\pi}{2}} 1 - \frac{\pi^2}{4}\frac{(x-x_0)^2}{2x_0^2}$

$$\rightarrow \frac{\pi}{576 f_{res}^3 R_d'} f_s^4 - \frac{\pi}{48 f_{res}^2 R_d'} f_s^3 + \left(C_f - \frac{1}{2\pi f_{res} R_d'} + \frac{\pi}{16 f_{res} R_d'} \right) f_s^2 - \frac{9}{\pi^2 L_{eq}} \neq 0 \qquad (4.27)$$

There are 4 closed form solution for Eq.4.27 however only the positive one needs to be considered. The actual solution is too extended to be of any use, a computational engine can likely be used to solve Eq.4.27. The phase margin PM can be written by evaluating Eq.4.21 at the crossover frequency ω_c:

$$PM = \pi + \phi\left(T_{delay}(s)\right)|_{s=j\omega_c} =$$

$$= \left(\pi + \phi(H_{PIC}^*) - j1.5\omega_c T_s - \phi\left(s^3 L_g L C_f + s^2 \frac{L_g C_f k_d V_{dc}}{2} e^{-1.5sT_s} + s\left(L_g + L\right) \right) \right)|_{s=j\omega_c} \rightarrow$$

$$\rightarrow PM = \arctan(2\pi T_i) - 1.5\omega_c T_s - \arctan\left(\frac{\frac{\omega_c k_d V_{dc}}{2} \cos(1.5\omega_c T_s)}{L(\omega_{res}^2 - \omega_c^2) - \frac{\omega_c k_d V_{dc}}{2} \sin(1.5\omega_c T_s)} \right) \qquad (4.28)$$

The gain margin GM_1 can be written as:

$$GM_1 = 20\log\left(T_{delay}(s)\right)|_{s=j\omega_{res}} = 20\log\left(\frac{LK_p}{(L+L_g)k_d}\right) \qquad (4.29)$$

Notice that $H_{PIC}(s) \approx H_{PIC}^*(s)$ has been used in the calculation of PM which is justified in high frequency ranges [52].

Based on Eq.4.29 and given a certain filter with resonance frequency ω_{res}, a general procedure may be written to effectively damp the system: chose ξ_d such that $GM_1 < -6\ dB$, calculate k_d based on Eq.4.14, check that $k_d < k_{dmax}$. Adjust the sampling frequency in the PWM firmware such that Eq2.63 is satisfied. The analysis done is only valid for $f_s > 6f_{res}$, which is common in SiC based filter and medium power application where high switching frequencies can be achieved.

Consider now the frequency f_{crit} that satisfies the equality that corresponds to Eq.4.27 as:

$$\frac{\pi}{576 f_{res}^3 R_d'} f_{crit}^4 - \frac{\pi}{48 f_{res}^2 R_d'} f_{crit}^3 + \left(C_f - \frac{1}{2\pi f_{res} R_d'} + \frac{\pi}{16 f_{res} R_d'} \right) f_{crit}^2 - \frac{9}{\pi^2 L_{eq}} \neq 0 \qquad (4.30)$$

f_{crit} is the switching frequency for which $f_{res}' = \frac{fs}{6}$, however f_{res}' is not very variable when $10f_{res} < f_s < f_{crit}$, since $0.8 < \sin\left(\frac{3\pi f_{res}}{f_s}\right) < 1$ in that range, meaning that f_{crit} can be used to estimate f_{res} without resorting to more analytic formulas as per Eq.4.31.

$$f_{res}' \approx \frac{f_{crit}}{6} \qquad (4.31)$$

Based on Eq.4.31, PM_2 is calculated on the new estimated resonance frequency and becomes:

$$GM_2 = 20\log\left(T_{delay}(s)\right)|_{s=j3\pi f_{crit}} \qquad (4.32)$$

Which can be kept $GM_2 < -3dB$ to ensure no negative crossover. Finally check that $PM > 45°$.

4.3.1.1 Active Damping Design Example

Consider the filter and control proposed in 4.1.1 with parameters: $L = 6\,mH$, $L_g = 0.3\,mH$, $C_f = 50\,uF$, $T_i = 0.0014\,s$ and $K_p = 0.0237$. The resonance frequency is $\omega_{res} = 8333\frac{rad}{s}$ or $f_{res} = 1335\,Hz$. Consider $k_{dmax} = 0.1$, k_d can be chosen such that:

$$GM_1 = 20\log\left(\frac{LK_p}{(L+L_g)k_d}\right) = -10\,dB < 6\,dB \rightarrow \frac{LK_p}{(L+L_g)k_d} = \sqrt{10} \rightarrow k_d = 0.071 \qquad (4.33)$$

Now the sampling frequency must be chosen, considering a typical operating point of $V_{dc} = 700\,V$. According to Eq.4.27 and Eq.4.31 $f_{crit} = 10.680\,kHz$, so that $f'_{res} \approx \frac{f_{crit}}{6}$. The sampling frequency can be chosen $f_s = 15\,kHz > f_{crit}$. The phase margin is calculated as $PM = 58.4°$ and the gain margin $GM_2 = -8.89\,dB$ which ensure excellent stability. In Figure 70 and Figure 71 magnitude and phase of $T_{delay}(s)$, with different parameters, are shown respectively. The calculated stability parameters $PM. GM_1, GM_2$ have been correctly assessed for the stable curve where $f_s = 15kHz$ and $k_d = 0.071$. In Figure 70 the yellow curve represents the ideal transfer function $T(s)$ of Eq.4.13 and shows the noticeable shift in resonance frequency when delays are accounted. As proof of the inherent instability some choices of sampling frequency the blue curve shows $T_{delay}(s)$ when $f_s = f_{crit}$, which presents a negative 0 dB crossing. Figure 71 shows that if the filter is designed in an appropriate way (i.e. as in 3.2) the high frequency components and active damping do not impact phase margin PM.

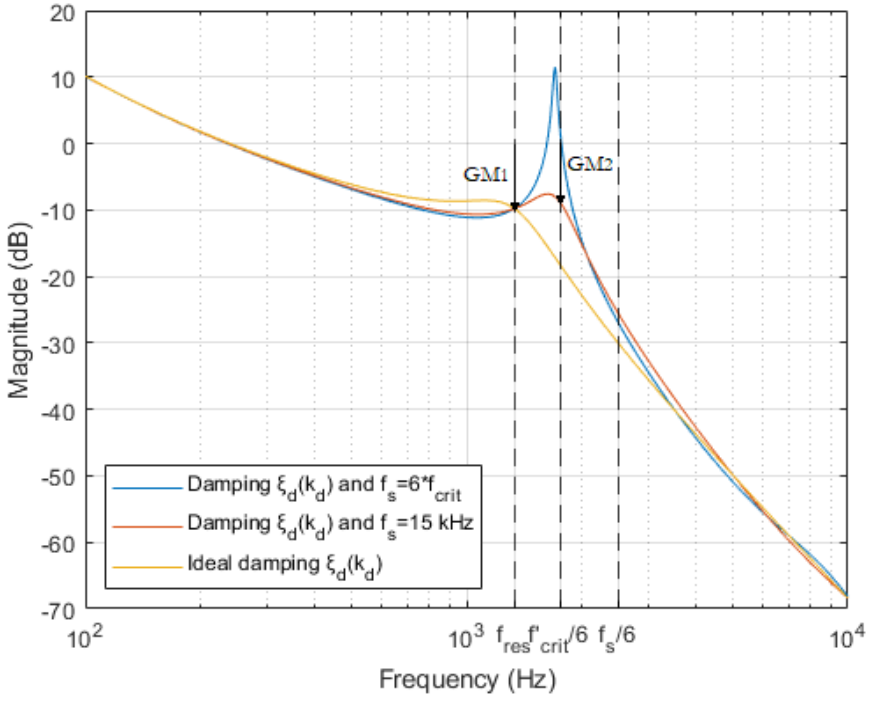

Figure 70 Magnitude bode plot of Eq.4.21 with kd = 0.071 and different sampling frequencies f_s

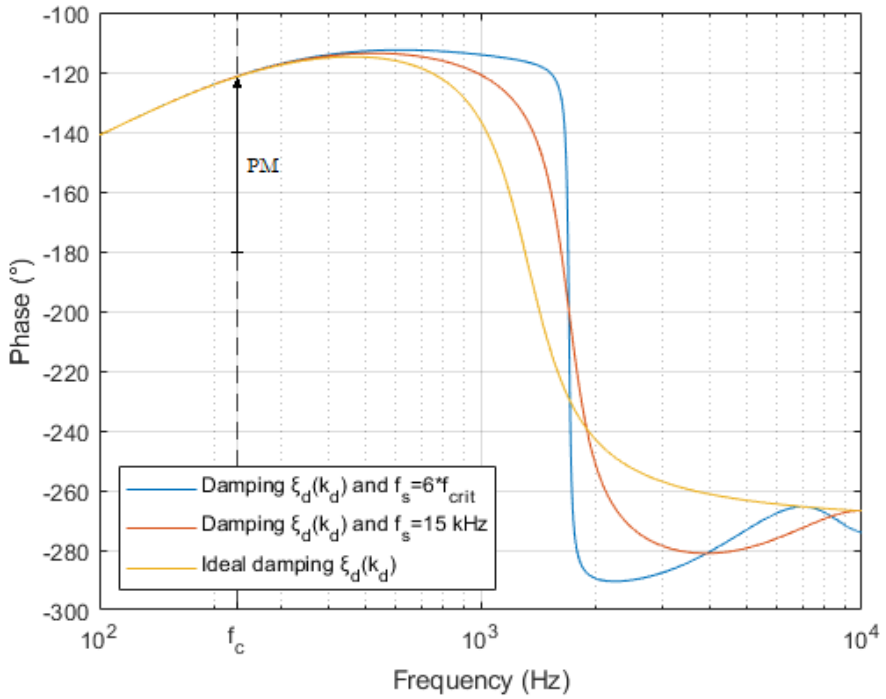

Figure 71 Phase bode plot of Eq.4.21 with kd = 0.071 and different sampling frequencies f_s

The system complete with delays has been simulated in MATLAB Simulink, at a discrete time of 100 kHz to grant the bandwidth for the observed effects. A fully electrical PMW model has been used to grant high fidelity shown in Figure 72.

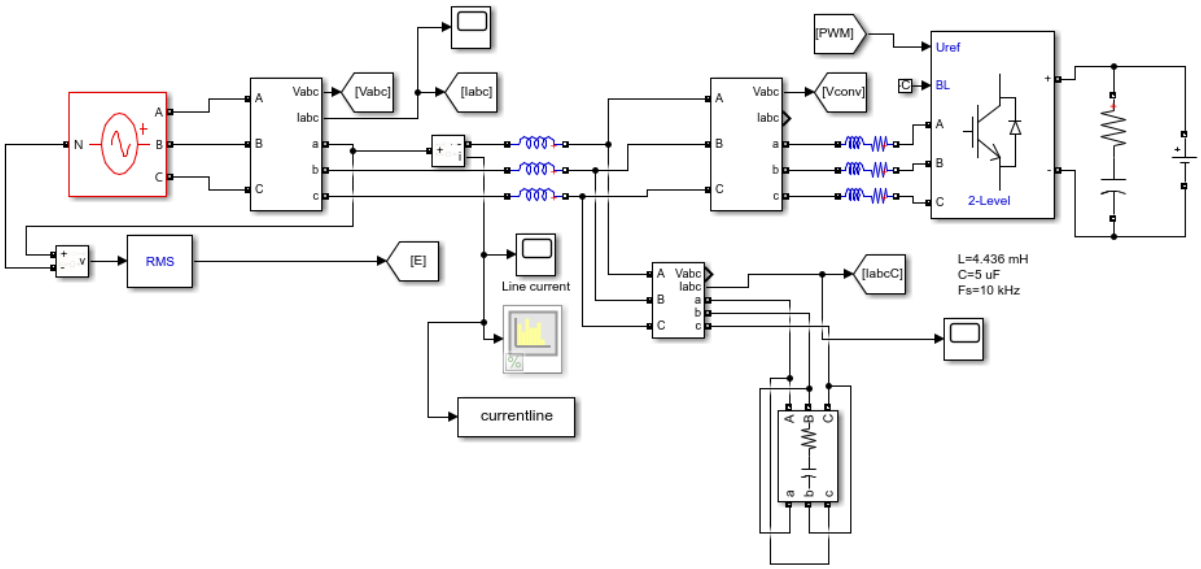

Figure 72 Electrical model of the ACDC converter

The direct current (I_d) regulation dynamic is observed in Figure 73 under a step-like change in reference from 5 kW to 10 kW. The controller exhibits good performances, however a ripple at 200 Hz of the 6^{th} harmonic is present, however grid current (phase 1) in Figure 74 is regular and shows low THD as per Figure 75. Notice the frequency associated with f_{res} of the filter is as low as 0.02%.

Another configuration with $f_s = 10\ kHz$ has been simulated, so that comparisons can be drawn. The choice $f_s = 10\ kHz$ is somewhat arbitrary in nature, however any lower frequencies (e.g. 9 kHz) made the system unstable in the simulation environment. The direct current (I_d) regulation dynamic is again shown Figure 76 where notable high frequency components are present. The line current in Figure 77 shows high THD as per Figure 78, where the harmonic associated with f_s' is over 6% that of the fundamental.

The simulations give active proof to the theory proposed above and set a definite criterion for the choosing of a system switching frequency and capacitor current feedback implantation strategy.

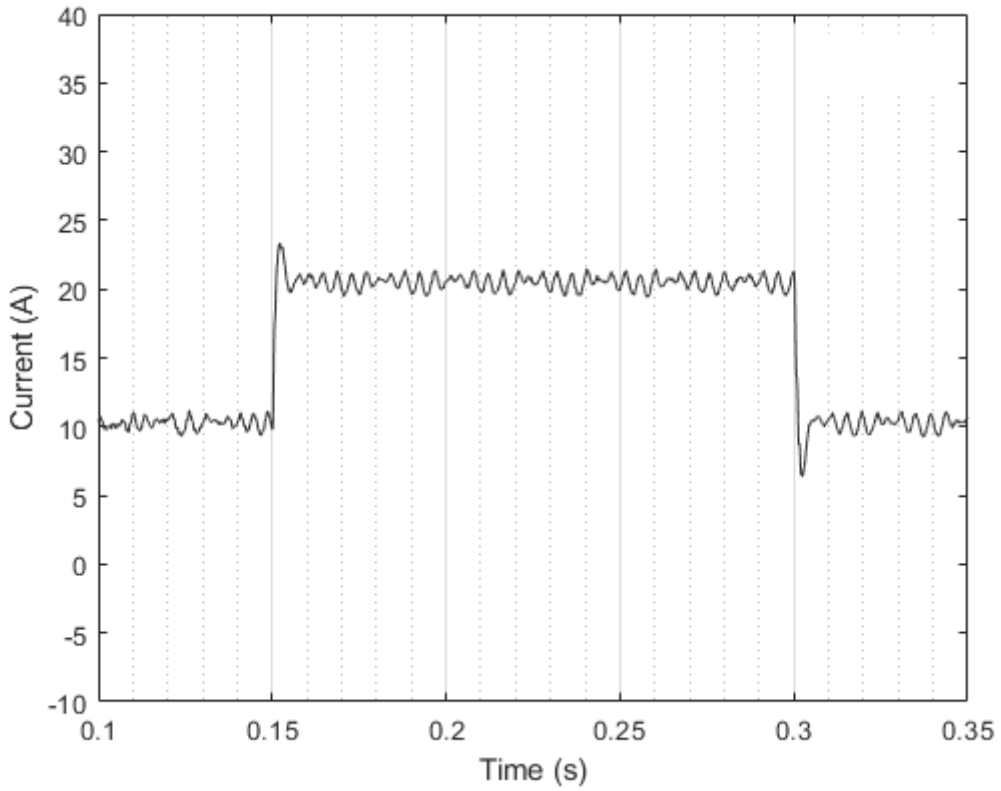

Figure 73 I_d current regulation when a 5kW step in reference is applied with $f_s = 15\ kHz$ and $kd = 0.071$

4.4 GRID SENSITIVITY

Finally, the performance of a digital active damping control can be shown against different transformer sizes. The current regulation in the direct axis is shown in Figure 79, where it can be noticed that the curves completely overlap, showing complete insensitivity to grid inductance. This behavior is well explained in Figure 80 and Figure 81, respectively the magnitude and phase plot of $T_{delay}(s)$ when different L_g (respectively of different sized transformers) are considered. The crossover frequency is unchanged, because the high frequency behavior of the LCL filter is always uncoupled with respect to the PI current control, however the phase margin degrades of around 15° when worst case scenario is considered. This, however, does not have tangible effects on the performances. The behavior at high and low

frequencies remains substantially unchanged, granting the classical low steady state errors of a PI controller.

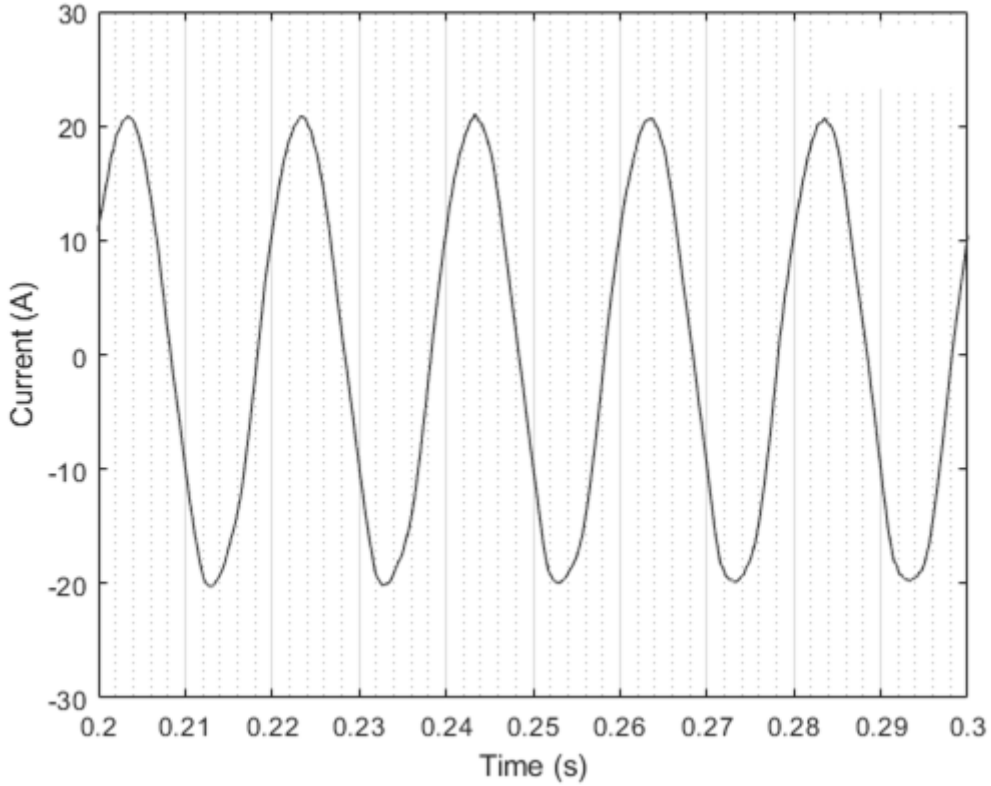

Figure 74 Line 1 grid current with $f_s = 15\ kHz$ and $kd = 0.071$

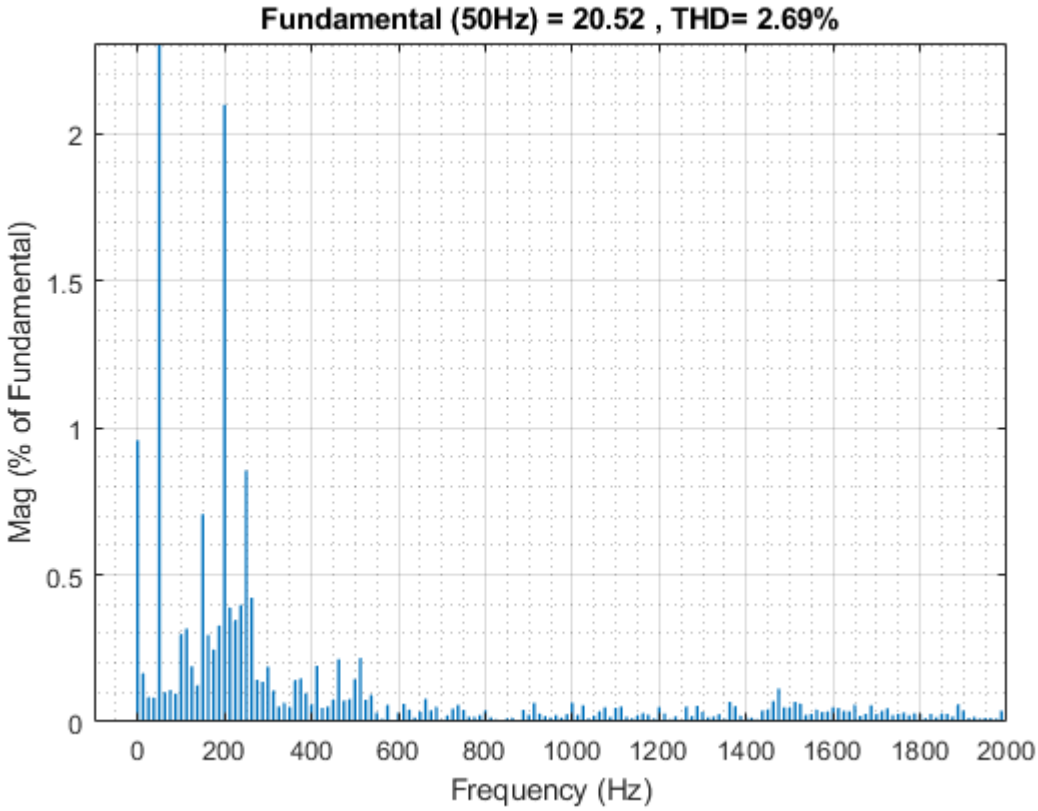

Figure 75 Line 1 grid current harmonic content with $f_s = 15\ kHz$ and $kd = 0.071$

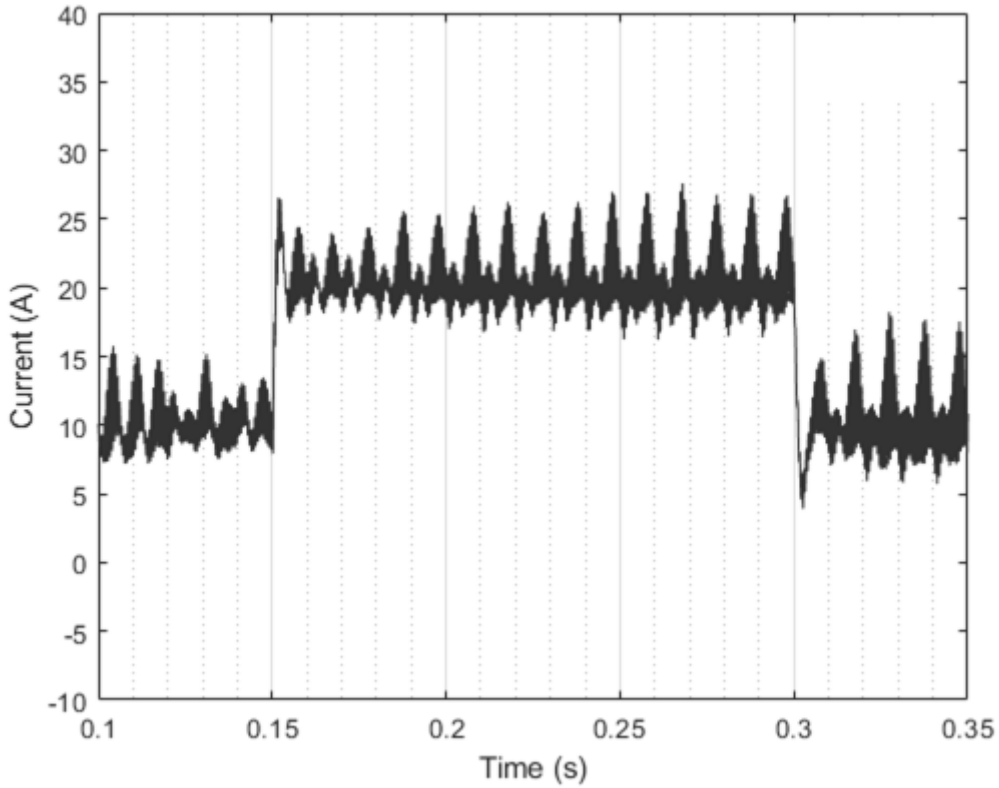

Figure 76 I_d current regulation when a 5kW step in reference is applied with $f_s = 10\ kHz$ and $kd = 0.071$

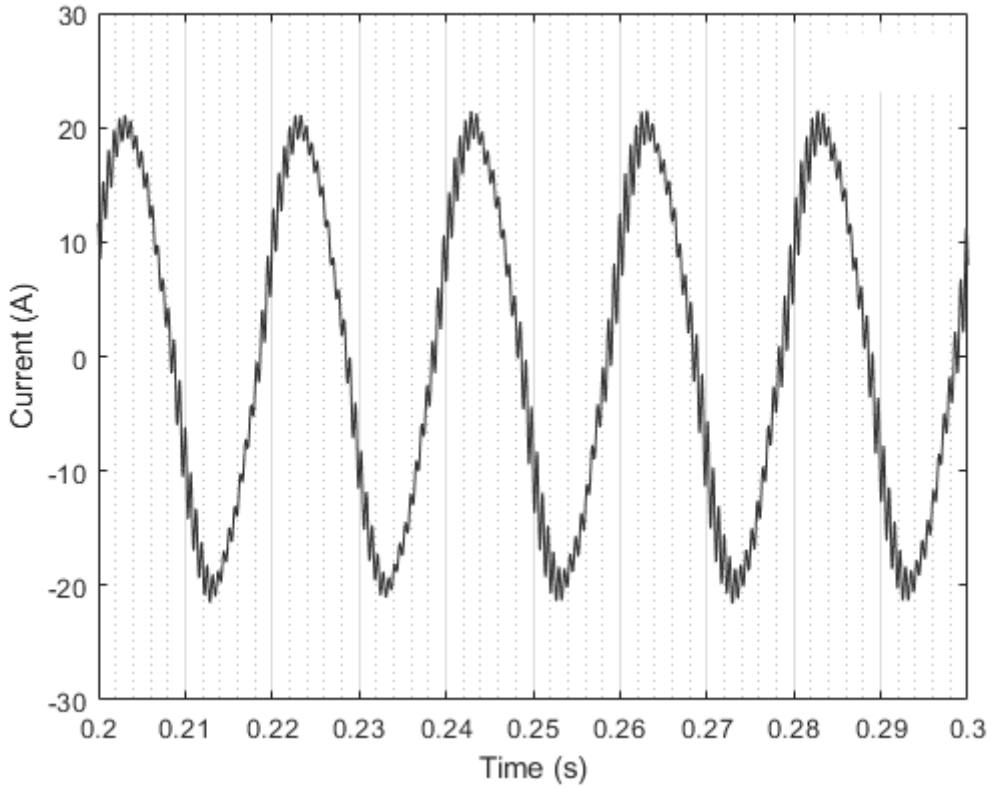

Figure 77 Line 1 grid current with $f_s = 10\ kHz$ and $kd = 0.071$

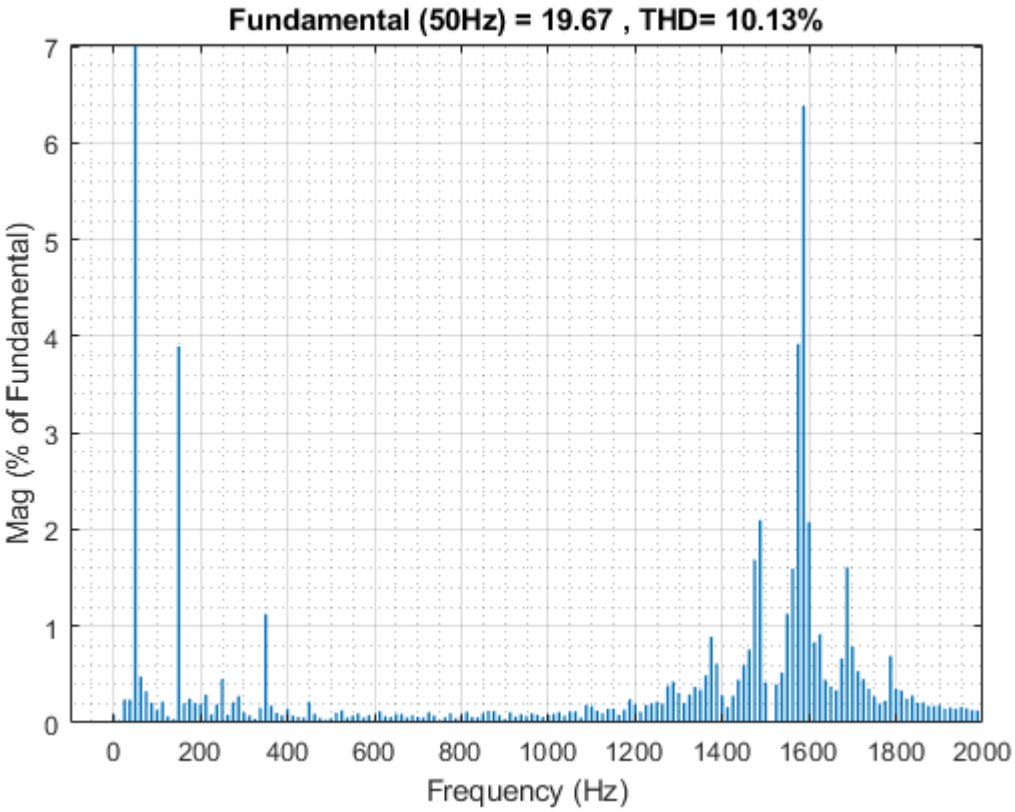

Figure 78 Line 1 grid current harmonic content with $f_s = 10\ kHz$ and $kd = 0.071$

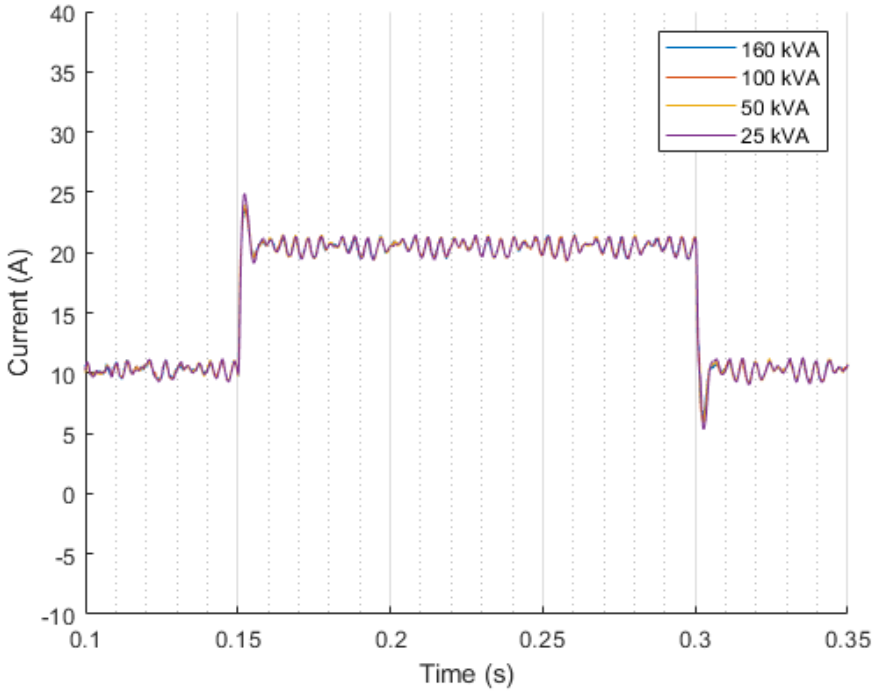

Figure 79 Active Damping Dynamic performances under different transformer size

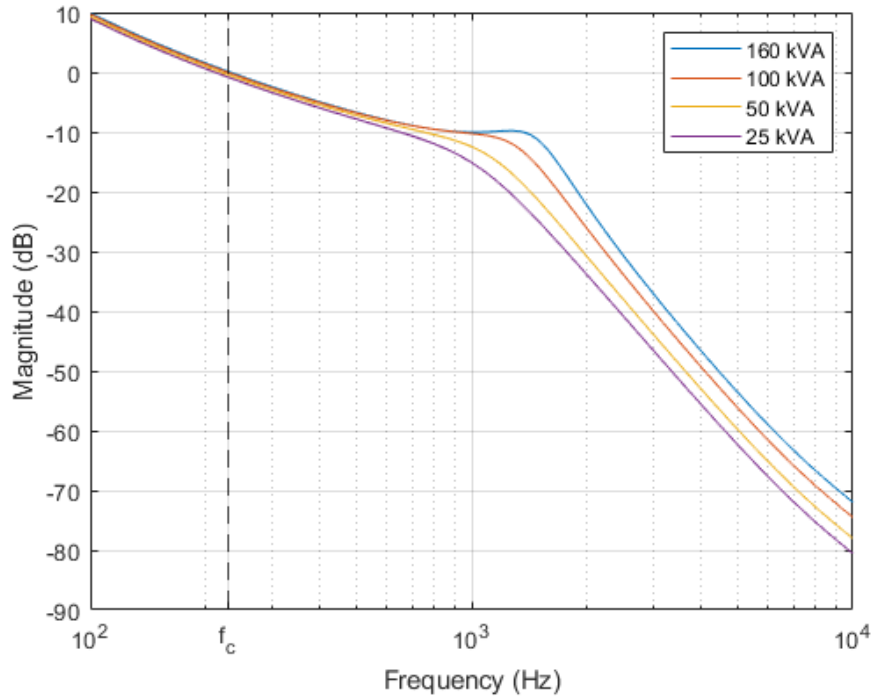

Figure 80 Magnitude bode plot Eq.4.21 with $f_s = 15\ kHz$ and $kd = 0.071$

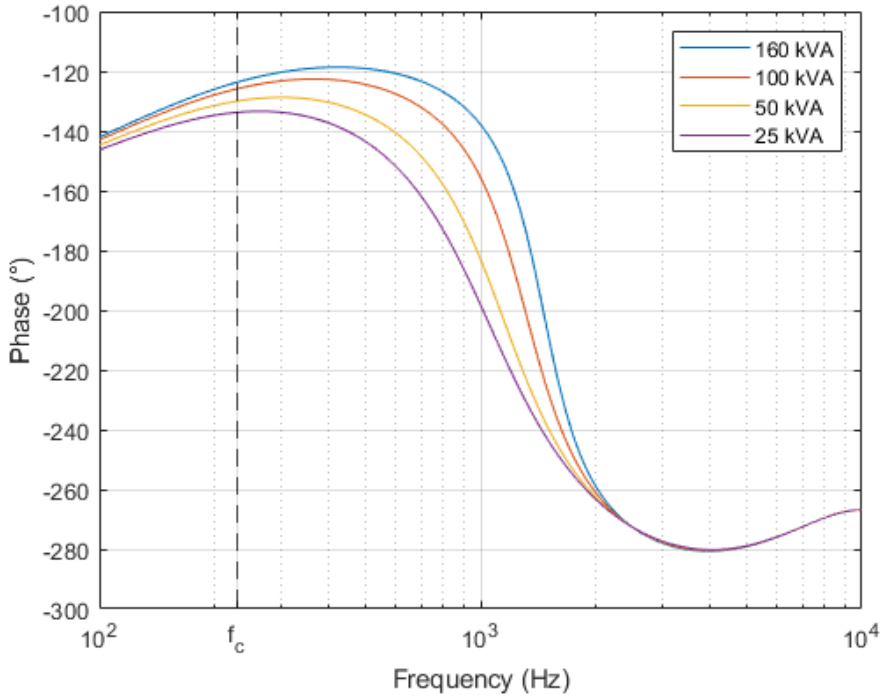

Figure 81 Phase bode plot of Eq.4.21 with $f_s = 15\ kHz$ and $kd = 0.07$

5 STR NON-LINEAR CONTROL

A possible approach to control the system dynamics without resorting to extra feedback loops is to artificially move the poles and zeros of the system under control to replicate well known and stable controlled system. The mechanism of the adaptation relies on precise parametric knowledge since, unlike classical control, the error $e(t)$ is not minimized directly via the control strategy. In general and adaptive control system can be defined as a system that changes its control parameters based on a feedback loop based on a precise performance index of the to-be-controlled process. In general the performance index is one which minimized grants stable operation; however its minimization can grant additional benefits: in the case of electric system accurate parametrization is often a byproduct of this control scheme.

In this context STR regulators employ a fixed structure which is easy to manipulate via an estimation algorithm and yield a consistent regulating effort on which they are based. The problem can then be split in two one of *underlying design* and one of *update process*. The main architecture of an STR regulator is depicted in Figure 82, the *underlying design* consists in the manner in which parameters modify the gains of the controller and the *update process* is the manner in which these parameters are obtained. Initially they can be considered independent, so that each step of the process can be analyzed without cross behavior.

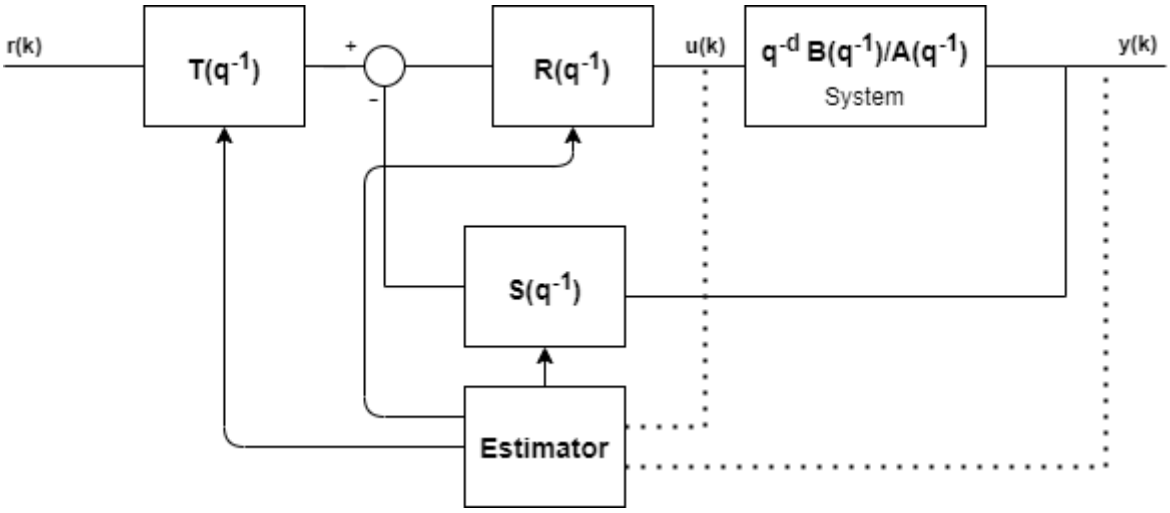

Figure 82 STR regulation scheme with adaptive estimator mechanism

Before delving into mathematical considerations a point must be made over which process *("System")* is the target of the control. In order to contain oscillations of the AC capacitor current in an ACDC converter the dynamics of the LCL filter must be considered, so it is natural to want to consider Eq.4.13 where the damping coefficient k_d is set to 0 and the controller is not yet implemented as per Eq.5.1, however as an initial step the simpler first order current model of Eq.4.3 can be considered as per Eq.5.2 where the minus sign has been omitted.

$$G_2(s) = \frac{\frac{V_{dc}}{2}}{s^3 L_g L C_f + s\left(L_g + L\right)} e_s^{-sT_s} \tag{5.1}$$

$$G_1(s) = K_c \frac{1}{sT_c + 1} e_S^{-sT_s} \tag{5.2}$$

Both processes are affected by the digital delay given by discrete implantation, which in this instance is considered synchronous and equal to T_s meaning both processes can be discretized in the form of Eq.5.3 taking T_s as timestep.

$$\boldsymbol{A}(q^{-1})y(k) = q^{-1}\boldsymbol{B}(q^{-1})u(k) \tag{5.3}$$

Where q^{-1} is the backshift operator, $A(q^{-1})$ is a monic polynomial and $A(q^{-1})$ is relatively prime with $B(q^{-1})$. The *underlying design* is solved by defining a target behavior to be mimicked and then translating it into a discrete process of similar form:

$$\boldsymbol{A_m}(q^{-1})y(k) = q^{-1}\boldsymbol{B_m}(q^{-1})r(k) \tag{5.4}$$

Where $A_m(q^{-1})$ is a stabler monic polynomial and $A_m(q^{-1})$ is relatively prime with $B_m(q^{-1})$. The STR controller equations can be written as:

$$\boldsymbol{R}(q^{-1})u(k) = \boldsymbol{T}(q^{-1})r(k) - \boldsymbol{S}(q^{-1})y(k) \tag{5.5}$$

Multiplying Eq.5.5 times $q^{-1}B(q^{-1})$ and restricting the analysis to SISO system yields:

$$[A(q^{-1})R(q^{-1}) + q^{-1}S(q^{-1})B(q^{-1})]y(k) = q^{-1}B(q^{-1})T(q^{-1})r(k) \tag{5.6}$$

Hence the connection between Eq.5.3 and Eq.5.4 can be made:

$$\frac{y(k)}{r(k)} = \frac{q^{-1}\boldsymbol{B_m}(q^{-1})}{\boldsymbol{A_m}(q^{-1})} = \frac{q^{-1}\boldsymbol{B}(q^{-1})T(q^{-1})}{[\boldsymbol{A}(q^{-1})\boldsymbol{R}(q^{-1}) + q^{-1}\boldsymbol{S}(q^{-1})\boldsymbol{B}(q^{-1})]} \tag{5.7}$$

From Eq.5.7 it can be noticed that the closed and open loop systems will share the same zeros due to the multiplication $B(q^{-1})T(q^{-1})$ however poorly damped zeros must not be simplified. in the present case $B(q^{-1})$ is considered stable so that not unstable zeros are present in both systems. The characteristic polynomial of the closed loop system can be recognized as $[A(q^{-1})R(q^{-1}) + q^{-1}S(q^{-1})B(q^{-1})]$ should contain the roots of $A_m(q^{-1})$ and the zeros which can be canceled of $B(q^{-1})$ which are none in the present case. $T(q^{-1})$ can already be obtained:

$$T(q^{-1}) = \frac{\boldsymbol{B}(q^{-1})}{\boldsymbol{B_m}(q^{-1})} \tag{5.8}$$

In order to get the other controller parameters it must be ensured that the denominators in Eq.5.7 can be matched as per Eq.5.9.

$$\boldsymbol{A_m}(q^{-1}) = \boldsymbol{A}(q^{-1})\boldsymbol{R}(q^{-1}) + q^{-1}\boldsymbol{S}(q^{-1})\boldsymbol{B}(q^{-1}) \tag{5.9}$$

it can be proved that there exist infinitely many solutions for $R(q^{-1})$ and $S(q^{-1})$ if the greatest common factor of $A(q^{-1})$ and $B(q^{-1})$ is a dividend of $A_m(q^{-1})$ which since $A(q^{-1})$ and $B(q^{-1})$ is guaranteed [55]. For a causal minimal solution more restrictions must be made:

$$\begin{cases} \deg \boldsymbol{S}(q^{-1}) < \deg \boldsymbol{A}(q^{-1}) \\ \deg \boldsymbol{S}(q^{-1}) = \deg \boldsymbol{A_m}(q^{-1}) - 1 \end{cases} \tag{5.10}$$

Constraints in Eq.5.10 define the order of closed loop behavior achievable with this strategy, for example taking $\deg A(q^{-1}) = \deg A_m(q^{-1})$ satisfies it, which enforces the same number of

non-cancelling poles for the open and closed loop system. Finally solving Eq.5.9 yields the final controller parameters.

5.1 DESIGN EXAMPLE

Consider the system described in 4.1.1 and Eq.5.2, the latter can be re-written as Eq.5.11 discretizing with sample time T_s via Euler's Transform:

$$F_1(z) = \frac{z^{-1}b_0}{z - a_1} \rightarrow y(k) = \frac{q^{-1}b_0}{1 + a_1 q^{-1}}u(k) \tag{5.11}$$

F_1 describes the open loop behavior which needs to be controlled, so the following target performance can be imagined:

$$G_{1_m}(s) = \frac{K_m}{s + K_m}e^{-sT_s} \tag{5.12}$$

Choosing K_m allows for the definition of the closed loop performance, for example choosing $G_{1_m}(j\omega_c) < 1$ at $\omega_c = 2000\,\frac{rad}{s}$ yields a settling time of around $0.5\ ms$, as shown in Figure 83. Discretizing in a similar manner Eq.5.12 to the form of Eq.5.11 the target system can be synthesized:

$$F_{1_m}(z) = \frac{z^{-1}b_{0_m}}{z - a_{1_m}} \rightarrow y(k) = \frac{q^{-1}b_{0_m}}{1 + a_{1_m}q^{-1}}r(k) \tag{5.13}$$

Solving for $S(q^{-1}), T(q^{-1}), R(q^{-1})$ assuming known parameters specified in the mentioned design example 3.2 yields:

$$\begin{gathered} S(q^{-1}) = [0.0314] \\ T(q^{-1}) = [0 + 0.0317q^{-1}] \\ R(q^{-1}) = [1] \end{gathered} \tag{5.14}$$

Figure 84 shows the implementation of this controller on the discretized small signal model of Eq.5.13 and compares the performance against the PI controller in the case of an average switch model and the more similar continuous small signal model. The results can be observed in Figure 85 where the STR outperforms the PI both in response time and in overshoot.

The STR controller with parameters in Eq.5.14 is the inserted in the average simulation circuital model of Figure 72. Notice this iteration if the STR controller cannot yet damp capacitor current since it is based on a first order model, so a damping resistance of $R_d = 1.5\ \Omega$ is used and as per usual consider the filter proposed in 4.1.1 with parameters: $L = 6\ mH$, $L_g = 0.3\ mH$, $C_f = 50\ uF$, switching period associated to $f_s = 15\ kHz$ and simulation step time of $1\ us$ (had to be decreased to ensure stability so THD evaluations will have a baseline advantage).

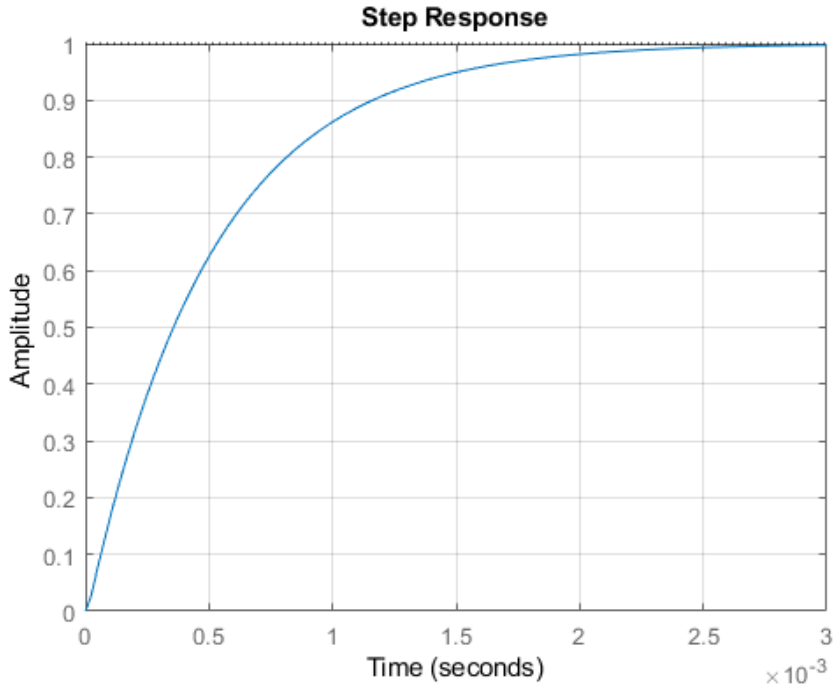

Figure 83 Step Response of target closed loop performance of Eq.5.12.

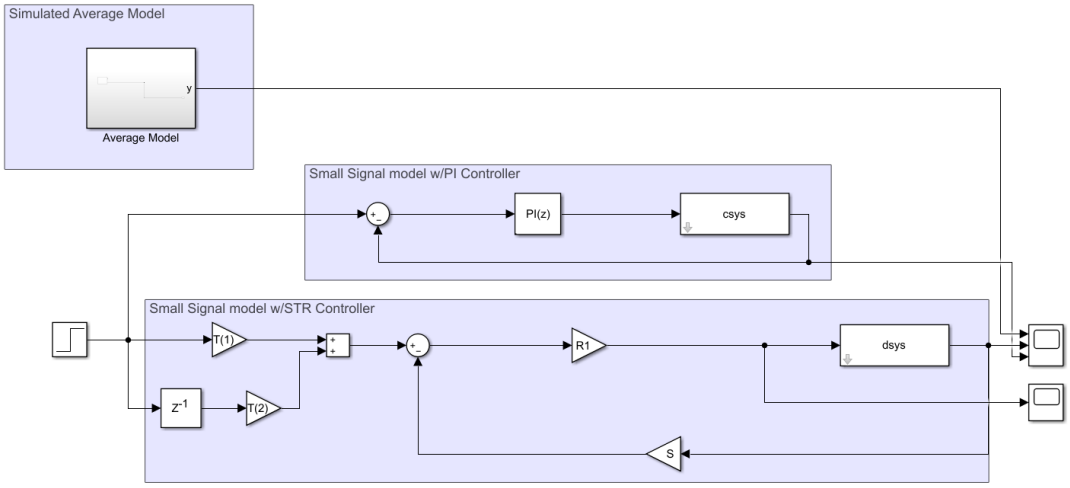

Figure 84 STR to PI Controller comparison scheme

The plant parameters are not yet continuously estimated to adapt to different transformer sizes and are considered known. The direct current (I_d) regulation dynamic is again observed in Figure 86 under a step-like change in reference from 5 kW to 10 kW. Comparing Figure 73 to Figure 86 the much better dynamic performances of the regulator can be assessed: there are not steady state ripples and the response to the step is within 2 ms. Figure 87 shows the line current using the newly found STR controller, the associated FFT is in Figure 88 where, as previously mentioned, the THD is very low due to the combination of the better controller and reduced simulation step size. However it is very likely that the performance of the SRT is an improvement over that of a PI even when accounting for the aforementioned factors.

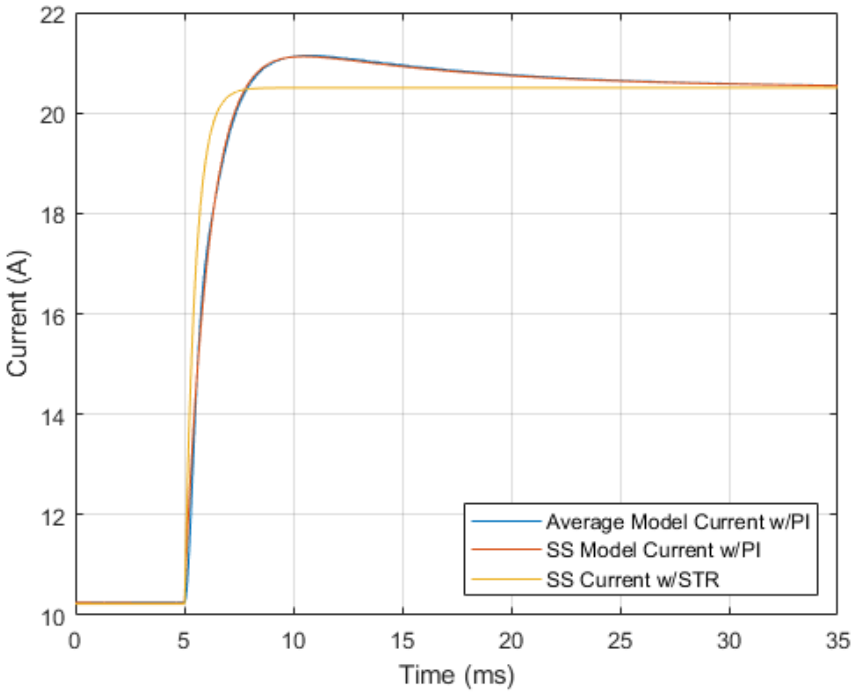

Figure 85 Current step response comparison STR to PI

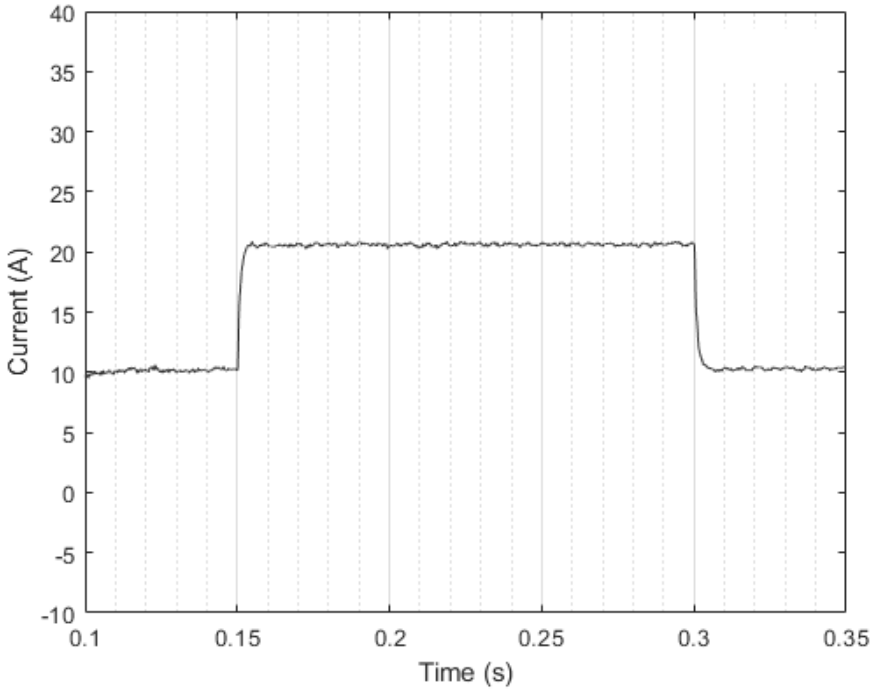

Figure 86 I_d current regulation to a 5kW step in reference with STR controller

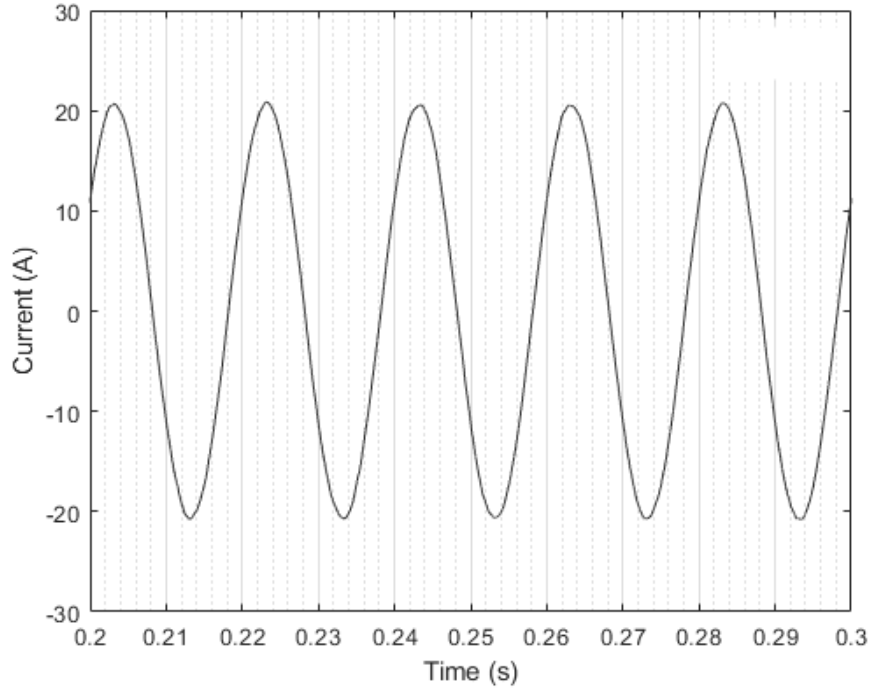

Figure 87 Line 1 gird current with STR controller

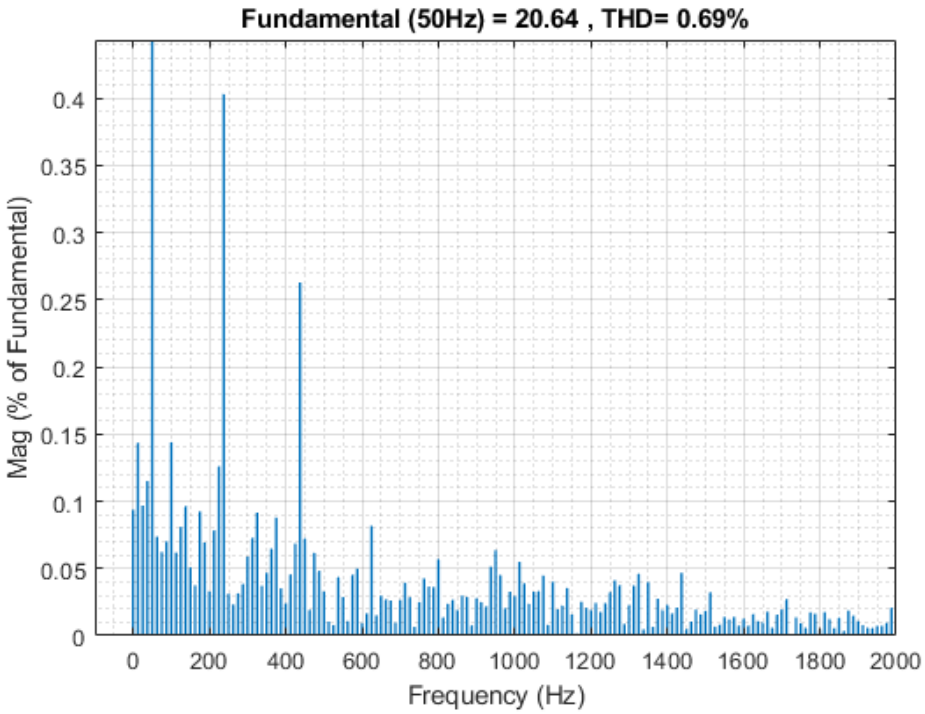

Figure 88 Line 1 grid current harmonic content with STR regulator

The used configuration still uses passive resistors to damp the LCL filter; consider now instead a discretization of Eq.5.1 as previously did with Eq.5.2 in Eq.5.11 then Eq.5.15 can be written (for general a and b coefficients):

$$F_2(z) = z^{-1}\frac{z^2b_0 + zb_1 + b_2}{z^3 + z^2a_1 + za_2 + a_3} \rightarrow y(k) = q^{-1}\frac{b_0 + b_1q^{-1} + b_2q^{-2}}{1 + q^{-1}a_1 + q^{-2}a_2 + q^{-3}a_3}u(k) \qquad (5.15)$$

The target control functions can be decided of the form in Eq.5.16 following constraints of Eq.5.10:

$$G_{2_m}(s) = \frac{\prod K_{im}}{(s+K_{1m})(s+K_{2m})(s+K_{3m})} e^{-sT_s} \tag{5.16}$$

The coefficient K_m can be chosen such that $K_{1m} \ll K_{2m} \ll K_{3m}$ where K_{1m} is the near crossover frequency pole or dominant pole at $2000\frac{rad}{s}$, the others can be chosen sufficiently large; in this case $K_{1m} = 200\ \frac{rad}{s}; K_{2m} = 10000\frac{rad}{s}; K_{3m} = 20000\frac{rad}{s}$. Eq.5.16 can be discretized:

$$F_{2_m}(z) = z^{-1}\frac{z^2 b_{m0} + z b_{m1} + b_{m2}}{z^3 + z^2 a_{m1} + z a_{m2} + a_{m3}} \rightarrow y(k) = q^{-1}\frac{b_{m0} + b_{m1}q^{-1} + b_{m2}q^{-2}}{1 + q^{-1}a_{m1} + q^{-2}a_{m2} + q^{-3}a_{m3}} r(k) \tag{5.17}$$

Solving for $S(q^{-1}), T(q^{-1}), R(q^{-1})$ yields:

$$\begin{aligned} S(q^{-1}) &= 10^4 * [2.7156 - 5.3056q^{-1} + 2.5931q^{-2}] \\ T(q^{-1}) &= [0 + 11.0215q^{-1} + 10.1841q^{-2} + 9.3920q^{-3}] \\ R(q^{-1}) &= [1 + 0.2387q^{-1} + 0.0483q^{-2}] \end{aligned} \tag{5.18}$$

Notice in this case the considered small signal system is not inherently stable, since no damping resistance is present in Eq.5.1, the STR control shifts the poorly damped poles as shown in Figure 89

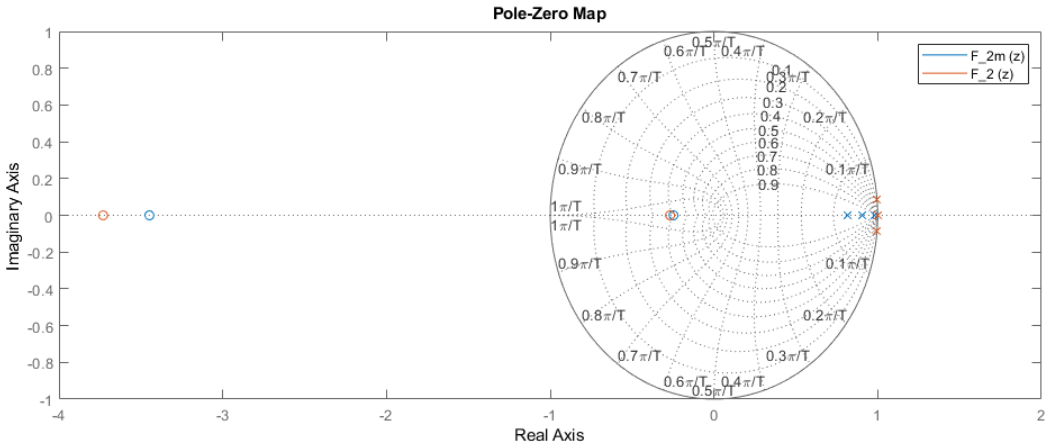

Figure 89 Zero Pole map of Eq.5.15 and Eq.5.16

Again the performances are compared like before into the average and small signal systems in Figure 90 and Figure 91.

Unfortunately, as shown in Figure 92, the control signal well exceeds the limits accepted by a PWM converter, considering in normal circumstances $\tilde{u}(t)$ should be well below 0.5, so it cannot be implemented into any real simulation or practical model.

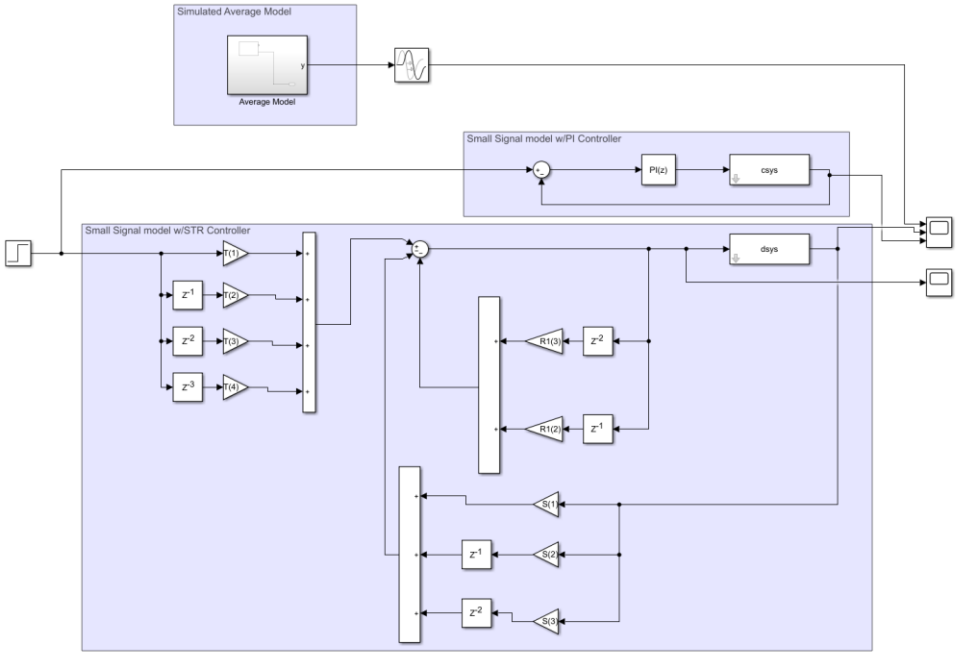

Figure 90 Active damping STR to PI Controller comparison scheme

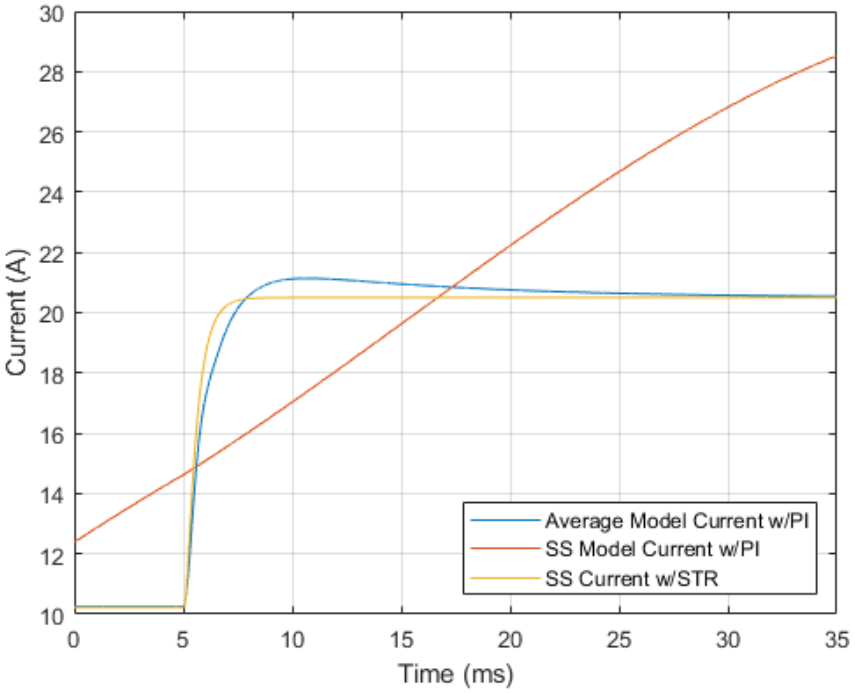

Figure 91 Current step response comparison active damp STR to PI

In Figure 91 it can be noticed that the PI controller is unable to meet performances since it cannot damp poorly damped poles, while the STR maintains performances from the previous comparison as predicted.

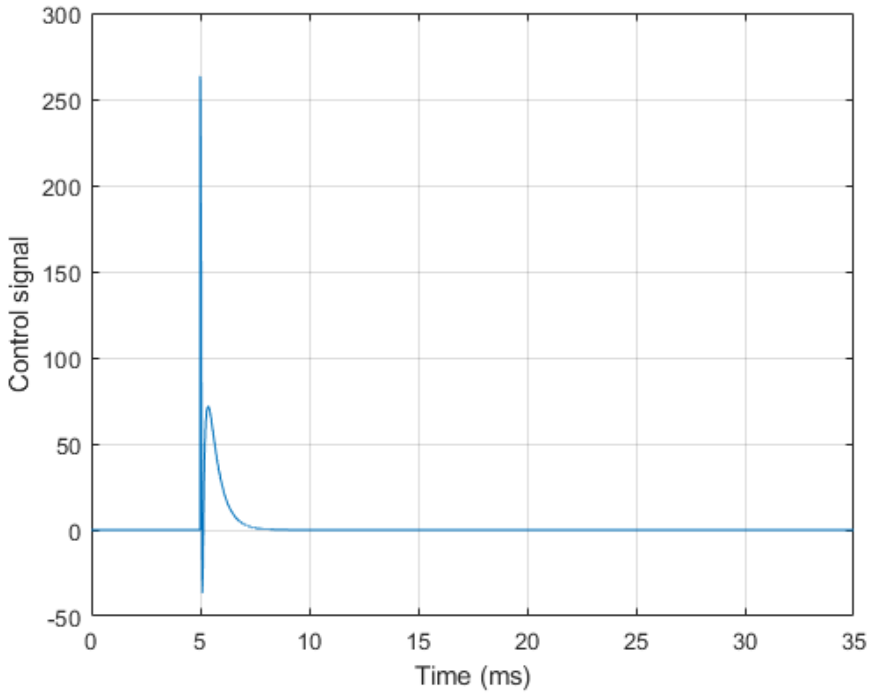

Figure 92 Small signal control when using active damp STR controller

5.2 PARAMETER ESTIMATION

In order to ensure the convergence of the control error to 0 an online estimation algorithm must be used. In this case the Forgetting Factor Mean Least Squares algorithm (FFMLS) has been used. The general algorithm is as follows:

$$\boldsymbol{\theta}(k+1) = \boldsymbol{\theta}(k) - \frac{\boldsymbol{P}(k-1)\boldsymbol{\zeta}(k)\boldsymbol{\varepsilon}(k)}{m^2(k)} \tag{5.18}$$

$$\boldsymbol{P}(k) = \frac{1}{\lambda}\boldsymbol{P}(k-1) - \frac{\boldsymbol{P}(k-1)\boldsymbol{\zeta}(k)\boldsymbol{\zeta}^{\boldsymbol{T}}(k)\boldsymbol{P}(k-1)}{m^2(k)} \tag{5.19}$$

$$m(k) = \sqrt{1 + \boldsymbol{\zeta}^{\boldsymbol{T}}(k)\boldsymbol{P}(k-1)\boldsymbol{\zeta}(k)} \tag{5.20}$$

$$\varepsilon(k) = y(k) - \boldsymbol{\theta}(k)\,\boldsymbol{\zeta}^{T}(k) \tag{5.21}$$

Where $\boldsymbol{\theta}$ are the system parameters, $\boldsymbol{\zeta}$ are the system regressor and λ is the forgetting factor. In this case, $\boldsymbol{\theta} = [b_0\ a_1]$, $\boldsymbol{\zeta} = [u(k)\ y(k)]$ and λ as been chosen to be 0.99 to aid convergence. The filter is initialized with known supposed values and launched when a step reference is applied so that only the small signal variations are detected. Figure 93 shows the convergence of the guessed parameters to a known case.

5.3 GRID SENSITIVITY

In this last chapter the performance of the STR controller can finally be waged against transformer sizes. This control structure possesses a definite advantage over the PI classical one because it defines a fixed closed loop structure with high phase margin even near the resonant frequency. The controller structure and gains are defined in Figure 84 and Eq.5.14. The change in reference current is shown in Figure 94 for 4 different transformers at different rated powers.

The step in reference is the usual 5 to 10 kW which means around 10 A in the direct current reference, it can be seen that there is only slight loss of phase margin, causing oscillations for the 25 kVA simulation.

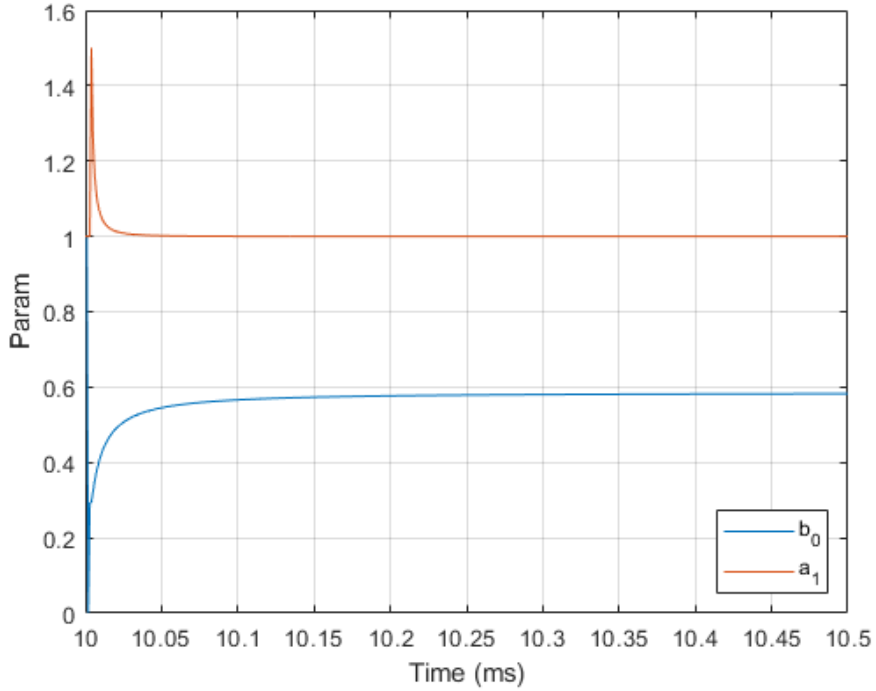

Figure 93 Real time parameter estimation

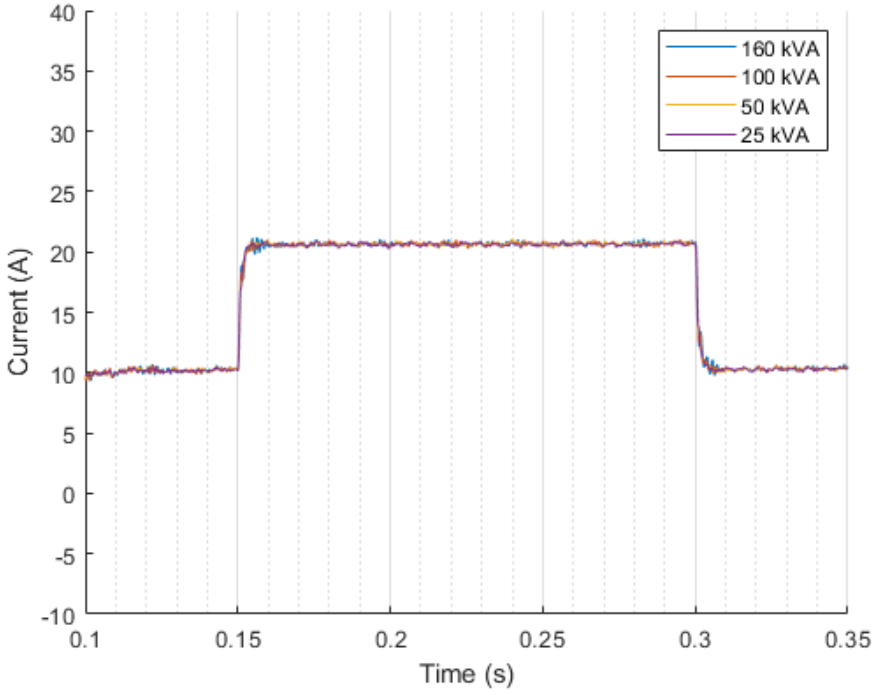

Figure 94 Passive STR controller performances under different transformer sizes

6 CONCLUSIONS AND NEXT STEPS

The current electric distribution grid is not able as of yet to sustain higher penetration of EV, infrastructures will have to be updated if there is any chance to complete the electric transition. In the meanwhile a Fast-Charging alternative is represented by local energy storage such as the fast charger with integrated battery presented. The construction of such a device is complicated and requires understanding of many areas: batteries, power electronics and distribution systems. The main variables and sizing problem have been presented for lithium-ion batteries which constitute the present of electric accumulation systems. The importance of SOC and SOH has been highlighted via simulation models and more importantly SL application, which are essential to diminish the impact of the transition.

A sizing problem has been set up considering statistical models of the battery and a method to maximize the investment in function of the start of SL has been found. The high variability in the model requires more fine tuning based on the specific battery chemistry and product, but the optimal SL start of life was place at around 0.83 which is a value accepted in industry.

Preliminary results from the construction of a prototype have been show along with architecture and simulation structure. In the future the BES will have to be integrated with the tested power electronics, which remains the more difficult task. Batteries will need to become smarter and more deployable if a more profuse usage is to happen in the near future.

Next the control of the ACDC Active Front End has been taken into consideration. For diffused battery storage to be useful V2G functionalities need to be implemented, this requires strict bounds in the performance of the inverter. Low response time is achieved via a classic PI controller, however the low efficiency of passive damping and the high sensitivity to the grid impedance require the employ of other control tactics, such as active capacitor current damping.

The active damping proposed has been analyzed and the digital implementation has been taken into consideration for a fixed sampling time (synchronous). A novel way to determine switching frequency based on the resonant frequency of the filter has been found and tested in simulation software.

Finally and STR controller has been proposed to rival the PI classical controller in the matter of gird sensitivity. After introducing the mathematical determination of such a structure, based on previous examples, the controller has been implemented in simulation. The STR controller achieves low THD and high response time, however it requires complicated calculations, especially in real time.

The two proposed damping strategies were compared, keeping in mind that ACC has no passive damping component it would seem that it is the more efficient of the two, however the performances of an STR controller greatly outclass the PI ones. It is possible to envision a mix of the two, where the plant is modeled after taking into account ACC modifications to the total transfer function.

REFERENCES

[1] U. N., "Paris Agreement," in *United Treaty Collection [OL]*, https://treaties.un.org/pages/ViewDetails.aspx?src=TREATY&mtdsg_no=XXVII-7-d&chapter=27&clang=_en, 2016.

[2] WHO, "World Health Org. Website,". [OL]. Available: https://www.who.int/airpollution/ambient/health-impacts/en/ Accessed: 10 08 2020.

[3] "Hannah Ritchie and Max Roser (2017) - "CO_2 and Greenhouse Gas Emissions" [OL]. Published online at OurWorldInData.org. Retrieved from: 'https://ourworldindata.org/co2-and-other-greenhouse-gas-emissions' [Online Resource," [Online].

[4] E.U., "European Climate Change Commitee," [OL]. Available: https://ec.europa.eu/clima/policies/transport/vehicles_en. [Accessed 10 08 2020].

[5] Zhang, Qian & Ou, X. &. Yan, X. &. Zhang and Xiliang., "Electric Vehicle Market Penetration and Impacts on Energy Consumption and CO2 Emission in the Future: Beijing Case.,"[J] *Energies.*, no. 10. 228. 10.3390/en10020228, 2017.

[6] D. Block, "EVTC," University of Central Florida, Orlando, FL, 30 2018. [OL]. Available: http://evtc.fsec.ucf.edu/research/project5.html. [Accessed 11 08 2020].

[7] A. Tripathi and S. Vaisambhayana, "Study of electric vehicles penetration in Singapore and its potential impact on distribution grid," [C] in *2016 Asian Conference on Energy, Power and Transportation Electrification (ACEPT)*, Singapore doi: 10.1109/ACEPT.2016.7811513., 2016.

[8] L. P. Fernández, T. G. S. Roman, R. Cossent, C. M. Domingo and P. Frías, "Assessment of the Impact of Plug-in Electric Vehicles on Distribution Networks," [J] in *IEEE Transactions on Power Systems*, doi: 10.1109/TPWRS.2010.2049133., 2011.

[9] Z. Jiang, L. Shalalfeh and M. J. Beshir, "Impact of electric vehicle infrastructure on the city of Chatsworth distribution system,"[C] in *2014 IEEE International Electric Vehicle Conference (IEVC)*, Florence doi: 10.1109/IEVC.2014.7056078., 2014.

[10] K. Clement-Nyns, E. Haesen and J. Driesen, "The Impact of Charging Plug-In Hybrid Electric Vehicles on a Residential Distribution Grid," [J] I*EEE Transactions on Power Systems*, vol. 25, no. 1 doi: 10.1109/TPWRS.2009.2036481., pp. 371-380, 2010.

[11] X. Zhu, B. Mather and P. Mishra, "Grid Impact Analysis of Heavy-Duty Electric Vehicle Charging Stations," [J] in *2020 IEEE Power & Energy Society Innovative Smart Grid Technologies Conference (ISGT)*, Washington, DC, USA doi: 10.1109/ISGT45199.2020.9087651., 2020.

[12] Nguyen, Tran-Quoc, Seddik and Bacha, "Harmonic distortion mitigation for electric vehicle fast charging systems," [J] in *PowerTech (POWERTECH)*, 10.1109/PTC.2013.6652435., 2013.

[13] T. P. Joy, K. Thirugnanam and P. Kumar, ""A multi-point Bidirectional Contactless Charging System in a charging station suitable for EVs and PHEVs applications," [C] in *India Conference (INDICON)*, 2013.

[14] B. Sarlioglu, C. T. Morris, D. Han and S. Li, "Driving Toward Accessibility,"[J] *IEEE Industry Applications Magazine*, vol. 23, no. 1 doi: 10.1109/MIAS.2016.2600739, pp. 14-25, January 2017.

[15] J. Kopera, *Inside the Nickel Metal Hydrate battery, [B]* Cobasys, 2004.

[16] Energizer, *Nickel Metal Hydride Handbook, [OL]* Energizer LCC @ https://data.energizer.com/pdfs/nickelmetalhydride_appman.pdf [Accessed 13 01 2021].

[17] M. R. Patel, "Spacecraft Power Systems," [B] CRC Press ISBN 978-0-8493-2786-5, 2005, p. 209.

[18] Plett, Battery Management [B], London: Artech House, 2015.

[19] Y. Maletin, "Ultracapacitor technology: What it can offer to electrified vehicles," [C] in *2014 IEEE International Electric Vehicle Conference (IEVC)*, Florence pp. 1-4 doi: 10.1109/IEVC.2014.7056227, 2014.

[20] S. Amal, V. C. R., M. Sreedevi, G. Mineeshma and V. V., "Modelling of ultracapacitor and Power Management strategy for the parallel operation of Ultracapacitor and Battery in Electric Vehicle Configuration," [C] in *2016 IEEE International Conference on Power Electronics, Drives and Energy Systems (PEDES)*, Trivandrum pp. 1-6 doi: 10.1109/PEDES.2016.7914228, 2016.

[21] A. F. Burke, "Batteries and Ultracapacitors for Electric, Hybrid, and Fuel Cell Vehicles," [C] *Proceedings of the IEEE*, pp. 806-820, April 2007.

[22] A. Fotouhi, D. J. Auger, K. Propp and S. Longo, "Electric vehicle battery parameter identification and SOC observability analysis: NiMH and Li-S case studies," [C] in *8th IET International Conference on Power Electronics, Machines and Drives (PEMD 2016)*, Glasgow pp. 1-6 doi: 10.1049/cp.2016.0142, 2016.

[23] R. C. Nacu and D. Fodorean, "Battery Cells Characterization for Subsequent Operation in Battery Models used in Mobile Charging Station Designing," [C] in *Electric Vehicles International Conference (EV) pp. 1-5, doi: 10.1109/EV.2019.8892858*, Bucharest, Romania, 2019.

[24] G. Pebriyanti, "A lithium-ion battery modeling for a HIL-battery simulator," [C] in *2013 International Conference on Computer, Control, Informatics and Its Applications (IC3INA)*, Jakarta pp. 185-190 doi: 10.1109/IC3INA.2013.6819171, 2013.

[25] D. Cittanti, A. Ferraris, A. Airale, S. Fiorot and S. S. a. M. Carello, "Modeling Li-ion batteries for automotive application: A trade-off between accuracy and complexity," [C] in *2017 International Conference of Electrical and Electronic Technologies for Automotive pp. 1-8, doi: 10.23919/EETA.2017.7993213.*, Torino, 2017.

[26] J.-H. Bae and B. Zhiguo, "The development of technology on reduces the SOC error rate using Hybrid Kalman Filter(HKF) and the demonstration its performance using BMS platform," [C]

in *2016 IEEE Transportation Electrification Conference and Expo, Asia-Pacific (ITEC Asia-Pacific)*, Busan pp. 661-665 doi: 10.1109/ITEC-AP.2016.7513035, 2016.

[27] S. Baba and S. Adachi, "SOC Estimation of HEV/EV Battery Using Series Kalman Filter" [C] in *2012 Proceedings of SICE Annual Conference (SICE)*, Akita pp. 845-850, 2012.

[28] H. Guo, Z. Wang, Y. Li, D. Wang and G. Wang, "State of charge and parameters estimation for Lithium-ion battery using dual adaptive unscented Kalman filter" [C] in *2017 29th Chinese Control And Decision Conference (CCDC)*, Chongqing doi: 10.1109/CCDC.2017.7979374, 2017.

[29] R. Xiong and H. Mu, "Accurate state of charge estimation for lithium-ion battery using dual Uncsented Kalman filters" [C] in *2017 Chinese Automation Congress (CAC)*, Jinan, 2017 doi: 10.1109/CAC.2017.8243757.

[30] F. Herb, "Aging mechanisms in Lithium-Ion-Battery and PEM-Fuel Cell and their influence on Hybrid-Systems," [D], 2010.

[31] C. B. Doménech and M. Heleno, "Estimating the Value of Second Life Batteries for Residential Prosumers," [J] in *2019 IEEE Milan PowerTech, pp. 1-6, doi: 10.1109/PTC.2019.8810647.*, Milan, Italy, 2019.

[32] M. Abdel-Monem, O. Hegazy, N. Omar, K. Trad, P. V. d. Bossche and J. V. Mierlo, "Lithium-ion batteries: Comprehensive technical analysis of second-life batteries for smart grid applications" [C] in *2017 19th European Conference on Power Electronics and Applications (EPE'17 ECCE Europe)*, Warsaw, Poland, 2017, pp. P.1-P.16, doi: 10.23919/EPE17ECCEEurope.2017.8099385..

[33] E. M.-L. e. al., "Evaluation of lithium-ion battery second life performance and degradation," [C] in *016 IEEE Energy Conversion Congress and Exposition (ECCE), Milwaukee*, WI, USA, 2016, pp. 1-7, doi: 10.1109/ECCE.2016.7855090..

[34] A. Barré, B. Deguilhem, S. Grolleau, M. Gérard, F. Suard and D. Riu, "A review on lithium-ion battery ageing mechanisms and estimations for automotive applications," [J] *Journal of Power Sources Volume 241 ISSN 0378-7753,* pp. 680-689 https://doi.org/10.1016/j.jpowsour.2013.05.040., 2013.

[35] P. Ramadass, B. Haran, R. White and B. N. Popov, "Mathematical modeling of the capacity fade of Li-ion cells," [J] *Journal of Power Sources, Volume 123, Issue 2*, pp. 230-240 ISSN 0378-7753 https://doi.org/10.1016/S0378-7753(03)00531-7, 2003.

[36] E. Redondo-Iglesias, P. Venet and S. Pelissier, " Eyring acceleration model for predicting,"[J] *Journal of Energy Storage, Elsevier*, vol. 13, no. ff10.1016/j.est.2017.06.009ff. ffhal-01575005f, pp. 176-183, 2017.

[37] D. M. E. Hossain, J. Mody, H. M. R. Faruque, M. S. H. Sunny and N. Mohammad, "A Comprehensive Review on Second-Life Batteries: Current State, Manufacturing Considerations, Applications, Impacts, Barriers & Potential Solutions, Business Strategies, and Policies," [J] I*EEE Access, vol. 7, pp. 73215-73252, 2019, doi: 10.1109/ACCESS.2019.2917859.*.

[38] S. Saxena, Y. Xing, D. Kwon and M. Pecht, "Accelerated degradation model for C-rate loading of lithium-ion batteries," [J] *International Journal of Electrical Power & Energy Systems,* vol. 107, no. ISSN 0142-0615 https://doi.org/10.1016/j.ijepes.2018.12.016., pp. 438-445, 2019.

[39] D. N. Wong, D. A. Wetz, A. M. Mansour and J. M. Heinzel, "The influence of high C rate pulsed discharge on lithium-ion battery cell degradation," [C] in *2015 IEEE Pulsed Power Conference (PPC),* Austin, TX, USA, 2015, pp. 1-6, doi: 10.1109/PPC.2015.7297030..

[40] L. Buccolini, A. Ricci, C. Scavongelli, G. DeMaso-Gentile, S. Orcioni and M. Conti, "Battery Management System (BMS) Simulation Environment for Electric Vehicles," [C] in *2016 IEEE 16th International Conference on Environment and Electrical Engineering (EEEIC),* Florence doi: 10.1109/EEEIC.2016.7555475, 2016.

[41] M. Luzi, M. Paschero, A. Rossini, A. Rizzi and F. M. F. Mascioli, "Comparison Between Two Nonlinear Kalman Filters for Reliable SoC Estimation on a Prototypal BMS," [C] in *42nd Annual Conference of the IEEE Industrial Electronics Society,* Florence pp. 5501-5506. doi: 10.1109/IECON.2016.7794054, 2016.

[42] D. Andre, C. Appel, T. Soczka-Guth and D. U. Sauer, "Advanced mathematical methods of SOC and SOH estimation for lithium-ion batteries," [J]*Journal of Power Sources,* Vols. Volume 224, https://doi.org/10.1016/j.jpowsour.2012.10.001., no. ISSN 0378-7753 , pp. 20-27 , 2013.

[43] R. Ramachandran and M. Nymand, "Loss Modelling and Experimental Verification of A 98.8% Efficiency Bidirectional Isolated DC-DC Converter," [C] *11th European Space Power Conference,* vol. Volume 16, no. https://doi.org/10.1051/e3sconf/20171618003, p. 6, 2017.

[44] R. Ramachandran, M. Nymand and N. H. Petersen, "Design of a compact, ultra high efficient isolated DC-DC converter utilizing GaN devices," [C] *IECON 2014 - 40th Annual Conference of the IEEE Industrial Electronics Society,* no. doi: 10.1109/IECON.2014.7049142., pp. 4256-4261, Dallas, TX, USA 2014.

[45] A. Aarya and S. Deepa, "Multilevel Inverters-A Comparative Analysis," [J] *IOSR Journal of Electrical and Electronics Engineering,* Vols. e-ISSN: 2278-1676,p-ISSN: 2320-3331,, pp. 43-50.

[46] V. Kus and T. Josefova, "The use of theory of frequency modulation for the calculation of current harmonics of the voltage-source active rectifier," [C] *2013 International Conference on Applied Electronics,* Pilsen, Czech Republic, 2013, pp. 1-4..

[47] K. H. Ahmed, S. J. Finney and B. W. Williams, "Passive Filter Design for Three-Phase Inverter Interfacing in Distributed Generation," [J] *Electrical Power Quality and Utilisation,* vol. XIII, no. 2, pp. 49-58, 2007.

[48] M. Liserre, F. Blaabjerg and S. Hansen, "Design and control of an LCL-filter-based three-phase active rectifier," [J] *IEEE Transactions on Industry Applications,* vol. 41, no. 5 doi: 10.1109/TIA.2005.853373., pp. 1281-1291, 2005.

[49] A. Kahlane, L. Hassaine and M. Kherchi, "LCL filter design for photovoltaic grid connected systems," [J] *Revue des Energies Renouvelables SIENR'14 Ghardaïa,* pp. 227-232, 2014.

[50] M. Dursun and M. K. DÖŞOĞLU, "LCL Filter Design for Grid Connected Three-Phase Inverter," [C] in *2nd International Symposium on Multidisciplinary Studies and Innovative Technologies (ISMSIT)*, Ankara, pp. 1-4, doi: 10.1109/ISMSIT.2018.8567054., 2018.

[51] S. Bacha, I. Munteanu and A. Bractu, Power Electronic Converters Modeling and Control with Case Studie [B], Springer, London, Heidelberg, New York, Dordrecht: DOI 10.1007/978-1-4471-5478-5 ISSN 1439-2232, 2014.

[52] D. Pan, X. Ruan, C. Bao, W. Li and X. Wang, "Capacitor-Current-Feedback Active Damping With Reduced Computation Delay for Improving Robustness of LCL-Type Grid-Connected Inverter," [J] I*EEE Transactions on Power Electronics PP*. *1-1.*, 2014 doi:10.1109/TPEL.2013.2279206. .

[53] W. Xia and J. Kang, ""Stability of LCL-filtered grid-connected inverters with capacitor current feedback active damping considering controller time delays," [J] *Journal of Modern Power Systems and Clean Energy*, vol. 5, no. 4 doi: 10.1007/s40565-017-0309-9, pp. 584-598, July 2017.

[54] Y. Tang, W. Yao, P. C. Loh and B. F., "Design of LCL Filters With LCL Resonance Frequencies Beyond the Nyquist Frequency for Grid-Connected Converters,"[J] *IEEE Journal of Emerging and Selected Topics in Power Electronics*, vol. 4, no. 10.1109/JESTPE.2015.2455042, pp. 1-1, 2015.

[55] P. Paraskevopoulus, Modern Control Engineering [B], Basel, Switzerland: Dekker ISBN: 0-8247-8981-4, 2002.

[56] WHO, "World Health Organization," [Online]. Available: https://www.euro.who.int/en/health-topics/environment-and-health/air-quality/news/news/2018/5/over-half-a-million-premature-deaths-annually-in-the-european-region-attributable-to-household-and-ambient-air-pollution/infographic-air-pollution-the-silent-kil. [Accessed 10 08 2020].